Charles University in Prague

Faculty of Mathematics and Physics

Department of Surface and Plasma Science

Doctoral thesis

# Low Temperature Plasma at Intermediate Pressures and in the Magnetic Field – Experiment and Model

Mgr. Aleš Marek

supervisor: Prof. RNDr. Milan Tichý, DrSc.

branch: F-2 – Physics of Plasma and Ionized Media

Prague, January 2007

# Acknowledgements

I would like to acknowledge my colleagues and coworkers that collaborated with me in experiments and directed my work in useful discussions. In the first – experimental – part of the thesis I would like to acknowledge especially Radu Paul Apetrei from University of Iasi, Rumania, that collaborated with me in major part of emissive probe measurements during his stay in our laboratory, next thanks are devoted to Stefan Bogdan Olenici and Ramona Gstrein for collaboration during their short term stages. I want to thank to Mgr. Pavel Kudrna, Dr. for useful discussion and practical help in solving problems connected with arranging the experiment and in interpretation of results. My thanks are also devoted to Prof. Roman Schrittwieser for useful discussions and also for possibility to perform comparative measurements by emissive probes in his laboratory at University of Innsbruck, Austria.

In the second part of the thesis I would like acknowledge especially Mgr. Pavel Kudrna, Dr., that substantially helped me and lead me in corrections and improvement of OOPIC simulation code and also for useful and thorough discussion with him regarding the simulation and its numerical results.

At last by not at least I would like to thank my supervisor Prof. RNDr. Milan Tichý, DrSc. that led and supported me during the whole work. I'm grateful for his supervising, for inspirative discussions and also for arranging of several stages, that were realized during my postgradual study.

# Abstract

This work focuses on a low temperature plasma at intermediate pressures and in presence of a weak magnetic field. This type of plasma is used in many technological applications and it is therefore the object of our interest.

The first part of the thesis is devoted to emissive probe diagnostic in a low temperature plasma. Particularly on variations of the electron saturation current at varying probe emission. This problem was to our knowledge not systematically studied and explained yet. Overestimation of the plasma potential by strongly emitting probe technique in the low pressure plasma and its applicability in this type of plasma is discussed in this part as well.

The second part of the thesis is concerned on the two dimensional Particle-In-Cell model of the dc discharge in the cylindrical magnetron system. The discharge in this system was systematically experimentally studied and several experiments performed in this device was recently published by our group. Good experimental base is therefore available for comparison of the numerical data with experiment. The results of developed Particle-In-Cell model are presented here, compared with experiment and next advance of the work is suggested.

# Contents

# Nomenclature

## Roman Symbols

| | |
|---|---|
| $A_0$ | Sommerfeld constant |
| $A_p$ | probe area |
| $A_{RD}$ | Richardson constant |
| $B$ | magnetic induction |
| $\vec{c}$ | particle velocity |
| $d$ | diameter, distance between electrodes |
| $E$ | energy |
| $e$ | elementary charge |
| $E_F$ | Fermi energy |
| $f$ | distribution function |
| $\vec{F}$ | force |
| $g_i$ | degeneracy of state $i$ |
| $h$ | Planck constant |
| $I$ | current, discharge current |
| $I_{em}$ | emission current |

| | |
|---|---|
| $I_{es}$ | electron saturation current |
| $i_{es}$ | normalized electron saturation current |
| $I_{HEAT}$ | probe heating current |
| $I_{is}$ | ion saturation current |
| $I_p$ | probe current |
| $j_{em}$ | emission current density |
| $j_e^p$ | plasma electron current density |
| $j_e^s$ | emitted electron current density |
| $j_i^+$ | ion current density at the position of virtual cathode |
| $j_{is}$ | ion saturation current density |
| $k$ | Boltzmann constant |
| $l$ | length |
| $m$ | mass |
| $n$ | plasma density |
| $n_e$ | electron density |
| $n_e^p$ | plasma electron density |
| $n_e^s$ | emitted electron density |
| $n_i$ | ion density |
| $p$ | pressure |
| $q$ | charge |
| $R$ | reflection coefficient |
| $r$ | radial coordinate |

| | |
|---|---|
| $R_p$ | probe wire resistance |
| $r_p$ | probe wire radius |
| $\vec{r}$ | position vector |
| $s$ | sheath thickness |
| $T$ | temperature |
| $t$ | time, simulation time |
| $T_e$ | electron temperature |
| $T_{eW}$ | temperature of emitted electrons |
| $T_i$ | ion temperature |
| $T_W$ | temperature of emitting wall |
| $U$ | voltage, discharge voltage, probe voltage |
| $U_c$ | breakdown voltage |
| $U_{fl}$ | floating potential |
| $U_{pl}$ | plasma potential |
| $v$ | velocity |
| $z$ | axial coordinate |

**Greek Symbols**

| | |
|---|---|
| $\alpha$ | ionization coefficient |
| $\chi$ | work function |
| $\lambda_D$ | Debye length |
| $\epsilon_i$ | energy of state $i$ |
| $\varepsilon_0$ | electric constant |

| | |
|---|---|
| $\gamma_{se}$ | coefficient of the secondary emission |
| $\gamma$ | emission coefficient |
| $\mu_i$ | mobility of ions |
| $\nu$ | particles species ($\nu = e, i$) |
| $\omega_c$ | gyrofrequency |
| $\omega_{el}$ | plasma frequency |
| $\phi$ | normalized potential ($\phi = \frac{e\varphi}{T_e}$) |
| $\varphi$ | potential |
| $\varphi_{VC}$ | potential at virtual cathode position |
| $\varphi_W$ | wall potential |

## Other Symbols

| | |
|---|---|
| $\triangle t$ | time step |

## Acronyms

| | |
|---|---|
| $CPU$ | central processing unit (processor) |
| $DADI$ | Dynamic Alternating Direction Implicit method |
| $PIC - MCC$ | Particle-In-Cell simulation scheme with Monte Carlo method treated Collisions |

# Chapter 1

# Introduction, aims of the thesis

This work is focused on the low temperature plasma at intermediate pressures and in the presence of the weak magnetic field. This type of plasma is used in many technological applications and it is therefore the object of our interest. The main part of the experimental work was done in the cylindrical magnetron plasma in Department of Surface and Plasma Science, Charles University in Prague. Part of data important for comparison of results was obtained in low temperature non-magnetized plasma of Double Plasma machine (DP-machine) in laboratory of the Experimental plasma physics group at the Institute of Ion Physics and Applied Physics, University of Innsbruck, Austria.

Experiment presented in the first part of the thesis is aimed at the emissive probe diagnostics in the low temperature plasma. Motivation for the emissive probe measurements in the cylindrical magnetron plasma was the discrepancy of results of the PIC-MCC model of the discharge in the cylindrical magnetron, that is described in the second part of thesis, with the data obtained by Langmuir probe. The discrepancy was marked especially in the plasma potential profile. Emissive probe was therefore used as an independent technique for determination of the plasma potential for verification of the Langmuir probe data. Since the very interesting phenomena of the electron saturation current variations and overestimation of the plasma potential by the strongly emitting probe were found in our experiments, the first part of this thesis focuses on this problem in the more detail.

The aim of the first part of this work was therefore systematic study and characterization of variations of the electron saturation current of emissive probe at varying probe emission that were observed by several groups and that was not to our knowledge systematically studied and explained yet and on phenomenon of overestimating of the plasma potential by the strongly emitting probe technique in a low temperature plasma. Cylindrical magnetron system as well as DP-machine were in this part of thesis used only as plasma sources for emissive probe technique study.

In contrast to that the second part of the thesis is focused on a discharge. The aim of this part was to create functional two dimensional numerical model of the dc discharge in the cylindrical magnetron system. The plasma parameters of the dc discharge in this system at various discharge conditions was systematically experimentally studied by our group and also recently published in several publications. Good experimental base is therefore available for comparison of the numerical data with experiment. The numerical simulation was performed by using OOPIC code developed at the University of California, Berkeley, USA [Verboncoeur *et al.* (1995)]. It is well established 2d3v electromagnetic Particle-In-Cell code – two dimensional in space, three dimensional in velocities – used by several groups for solving problems in various types of plasma. The created model of the dc discharge in the cylindrical magnetron system is presented the second part of the thesis, its results are compared with experiment, discussed and next advance of the work is suggested.

# Part I

# Experiment – Emissive Probe Diagnostic

# Chapter 2

# Theory

As mentioned in Chapter 1, this part of the thesis is devoted to the emissive probe diagnostic in a low temperature plasma. Particularly on the variations of the electron saturation current at varying probe emission. This problem was to our knowledge not systematically studied and explained yet. Discussion of an overestimation of the plasma potential by strongly emitting probe technique in the low pressure plasma is performed in this part as well.

## 2.1 Plasma potential determination by the Langmuir probe

The plasma potential is an important quantity describing the plasma. It can be determined by several experimental techniques. One of the fundamental and well established methods is determination of the plasma potential as a potential at which the zero cross of the second derivative of the Langmuir probe characteristic occurs.

Typical Langmuir probe characteristic obtained in the low temperature plasma is depicted in figure 2.1. The probe characteristic can be divided into three regions according to particle currents flowing to the probe :

- ion accelerating region (for $U < 2U_{fl}$), sometimes called ion saturation current region

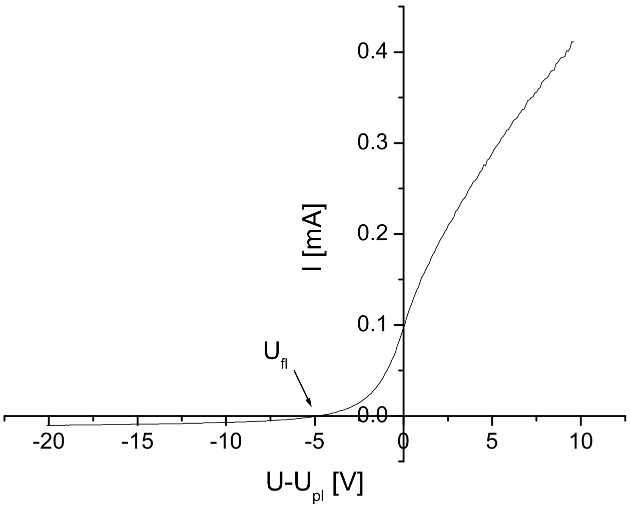

Figure 2.1: An example of Langmuir probe characteristic.

- transition region (for $2U_{fl} < U < U_{pl}$), sometimes called electron retarding region
- electron accelerating region (for $U > U_{pl}$), sometimes called electron saturated current region

where $U_{pl}$ is the plasma potential and $U_{fl}$ is the floating potential. Floating potential $U_{fl}$ is the potential at which no net current is flowing through the probe. Current flowing to the probe biased at plasma potential ($U = U_{pl}$) is given for each kind of charged particles species separately by:

$$I_{p\nu} = \frac{1}{4} A_p q_\nu n_\nu \overline{v_\nu}, \tag{2.1}$$

where $A_p$ is probe area, $q_\nu$ is charge of particle species $\nu$ ($\nu = e, i$), $n_\nu$ its density and $\overline{v_\nu}$ average velocity of particles of species $\nu$. At assumption of Maxwell-Boltzmann distribution $\overline{v_\nu}$ is:

$$\overline{v_\nu} = \sqrt{\frac{8kT_\nu}{\pi m_\nu}}. \tag{2.2}$$

Since electrons are lighter than ions, electron current flowing to the probe at plasma potential is higher than that of ions. The floating probe, however, has to charge negatively with respect to plasma potential in order to repel electrons and fulfill floating condition (no net current).

At plasma potential occurs in the probe characteristic change of curvature – inflection.

Inflection is reflected in the second derivative of the characteristic with respect to probe potential as a zero cross.

In semi-logarithmic scale there occurs a minimum as marked in figure 2.2.

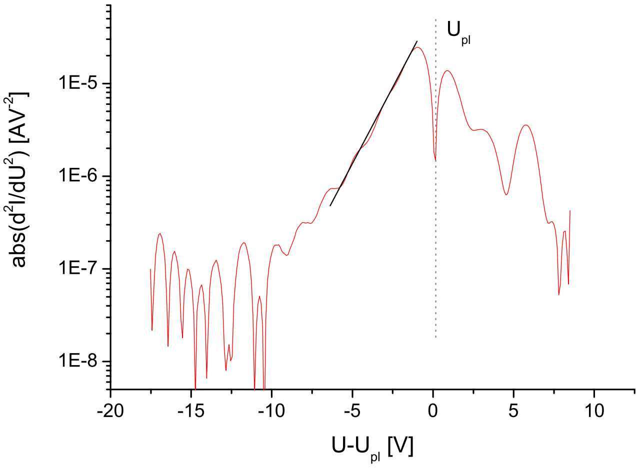

Figure 2.2: Absolute value of the second derivative of the Langmuir probe characteristic depicted in logarithmic scale.

In case of Maxwell-Boltzmann velocity distribution of electrons the electron current decays exponentially in the transition region. Consequentially, from the straight-line-approximated part of the second derivative in the electron retarding region it is possible to calculate the electron temperature. The details of this technique as well as derivation of other plasma parameters from the Langmuir probe characteristic can be be found in basic plasma literature, which also tackles the plasma diagnostics – e.g. [Auciello & Flamm (1989); Hippler *et al.* (2001)].

## 2.2 Emissive Probe diagnostic

Another diagnostic used for the plasma potential determination is an emissive probe diagnostic. Since this technique is in special interest of this work, more extensive description of this technique will be given here.

Emissive probes are nowadays used as a suitable experimental tool for determining the plasma potential in many types of plasmas ranging from hot isothermal plasma [Balan *et al.* (2003); Schrittwieser *et al.* (2001)] through low-temperature and low-pressure applications [Bradley *et al.* (2004); Wilson *et al.* (2002)] to dense plasma [Yan *et al.* (1996)]. They can be used also in presence of electron tails, drifts and even within non-neutral plasma of cathode sheaths [Okuno & Fujita (1991)]. Emissive probes were also successfully used for study of plasma potential fluctuations in small fusion devices [Schrittwieser *et al.* (2001)]. Several techniques of the plasma potential determination were established. Their basic overview is given e.g. in [Auciello & Flamm (1989)].

Two base techniques for the plasma potential determination by the emissive probe are frequently used – the strongly emitting probe technique and the inflection point in the limit of zero emission technique. Both techniques are based on the effect of thermionic emission of electrons from a probe wire.

### 2.2.1 Thermionic emission

Thermionic emission is process in which electrons overcome forces keeping them in material thanks to energy received by thermal excitation. The potential experienced by an electron in metallic material is schematically depicted in figure 2.3. The outer shell electrons of the metal atoms form a gas of nearly free electrons, moving as an electron gas in a background of positive charge formed by the ion cores. Not all the energy states in the conduction band are filled in metal. At absolute zero temperature only the lower part of the band is filled, while the higher energy states are unoccupied. However, when the metal is at room or higher temperature, a few of the electrons are excited to higher states by thermal excitation. The distribution of electrons in energy states is governed by Fermi-Dirac

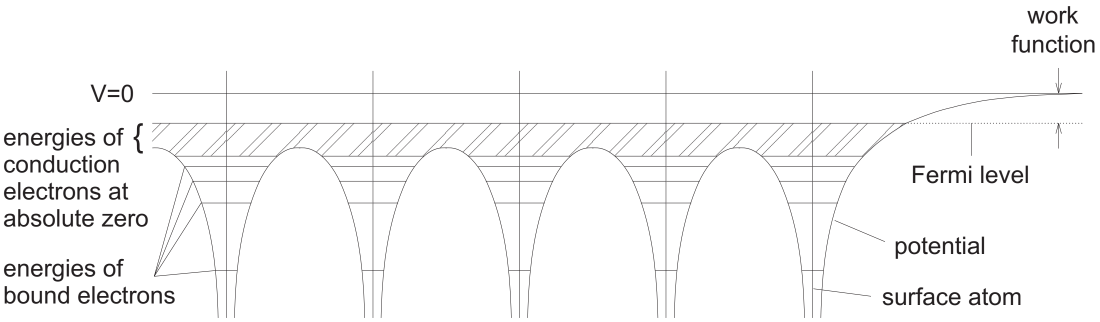

Figure 2.3: Periodic potential in metal. The potential is plotted along a line running through the centers of several of the atoms. The vertical lines in the figure indicate the locations of the atomic centers. The conduction band can extend from the bottom of shaded region to well above $V = 0$. Figure was taken from [Gewartowski & Watson (1965)].

statistic:

$$n(\epsilon_i) = \frac{g_i}{e^{\frac{\epsilon_i - E_F}{kT}+1}}, \tag{2.3}$$

where $n(\epsilon_i)$ is number of electrons in state with energy $\epsilon_i$, $g_i$ is the degeneracy of state $i$, $E_F$ is Fermi energy, $k$ is Boltzmann constant and T is temperature. Fermi energy $E_F$ is energy of the last populated state in the conducting band at temperature of absolute zero. The potential corresponding to this energy is frequently called the Fermi level. Fermi level is schematically depicted in figure 2.3. The energetic difference between Fermi level and potential of vacuum is called work function. Work function $\chi$ is therefore energy that must be given to an electron at the Fermi level to enable it to escape from the metal with zero velocity. Work function is characteristic quantity for each material.

Number of emitted electrons can be obtained by integration of those of them whose part of energy belonging to momentum in the direction of towards the metal surface is sufficient to overcome the work function. The thermionic current density can be obtained from:

$$j_{em} = e \int_{-\infty}^{\infty} \int_{-\infty}^{\infty} \int_{p_{x0}}^{\infty} [1 - R(E)] \frac{2}{m_e h^3} \frac{p_x dp_x dp_y dp_z}{e^{\frac{p_x^2 + p_y^2 + p_z^2 - E_F}{kT}} + 1}, \tag{2.4}$$

where $R(E)$ is reflection coefficient of the surface since some electrons can be reflected back into the material, $h$ is Planck constant, $p_x$ is momentum in direction $x$, where $x$ is direction towards surface, and $p_{x_0}$ is momentum of electron in this direction sufficient for overcoming of surface barrier. Energy dependent reflection coefficient $R(E)$ is usually replaced by its mean value $\overline{R}$ determined from experiment. By integration is obtained so called Richardson-Dushmann formula:

$$j_{em} = A_0(1-\overline{R})T^2 e^{-\frac{\chi}{kT}}, \tag{2.5}$$

where $A_0 = \frac{4\pi m_e k^2 e}{h^3} = 1.2 \times 10^6$ Am$^{-2}$K$^{-2}$ is so called Sommerfeld constant. Work function $\chi$ is not in reality temperature independent. The temperature dependence of the work function is in case of clean metal surface small and can be linearized in first approximation:

$$\chi(T) = \chi_0 + \alpha T, \tag{2.6}$$

where $\alpha \sim 10^{-4} - 10^{-5}$ eVK$^{-1}$. The Richardson-Dushmann formula determining thermionic electron current density from material at temperature $T$ can be than expressed by:

$$j_{em} = A_0(1-\overline{R})e^{-\frac{\alpha}{k}}T^2 e^{-\frac{\chi_0}{kT}} = A_{RD}T^2 e^{-\frac{\chi_0}{kT}}, \tag{2.7}$$

where $A_{RD}$ is Richardson constant, that varies with material (e.g. for tungsten $A_{RD} = 7 \times 10^5$ Am$^{-2}$K$^{-2}$, for tantalum $A_{RD} = 3.7 \times 10^5$ Am$^{-2}$K$^{-2}$; $\chi_0 = 4.5$ eV for tungsten, $\chi_0 = 4.12$ eV for tantalum ).

Energy distribution of emitted electrons is often assumed to be half Maxwell-Boltzmann in first approximation with characteristic temperature $T_{eW} = T$, where $T_{eW}$ is temperature of emitted electrons and $T$ is temperature of emitting wall. In contrast to that [Gewartowski & Watson (1965)] showed that energy distribution of thermionic electrons in direction normal to emitting surface is

$$dP(E_x) = \frac{1}{kT}e^{-\frac{E_x}{kT}}dE_x, \tag{2.8}$$

giving average energy carried in this direction

$$\overline{E_x} = \int_0^\infty E_x dP(E_x) = kT. \tag{2.9}$$

The total energy distribution of thermionic electrons is described by

$$dP(E) = \frac{E}{(kT)^2} e^{-\frac{E}{kT}} dE, \tag{2.10}$$

giving average energy carried by thermionic emitted electrons $\overline{E} = 2kT$.

### 2.2.2 Emissive probe characteristic

Thermionic emission of electrons from probe appears in emissive probe characteristic as an increase of ion saturation current in ion accelerating region as can be seen in figure 2.4, because the emission current superimposes on the ion saturation current. At increasing emission of electrons from the probe the floating potential of the probe moves towards the plasma potential as it is visible in figure 2.4. This fact is base of the plasma potential determination via strongly emitting probe technique described in detail in Chapter 2.2.3. Electron saturation current is expected to remain unaffected by emission of electrons from the probe since the emitted electrons are attracted back to the probe when the probe voltage becomes positive with respect to the plasma potential. In first approximation it is also true in many cases. On the other hand, in some cases the variation of electron saturation current cannot be neglected as it is shown in Chapter 2.2.5.

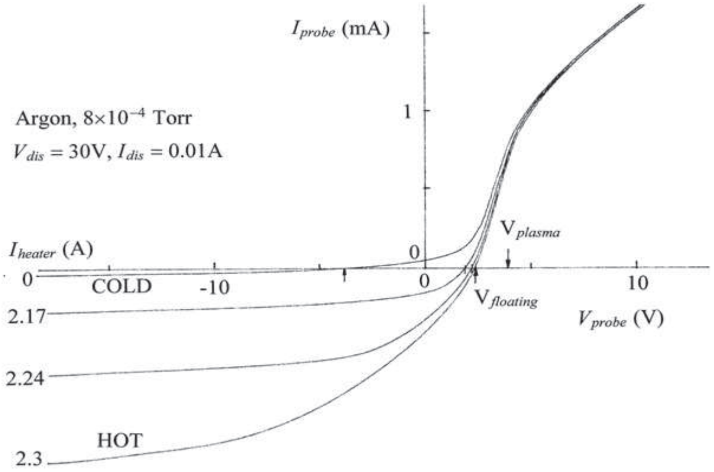

Figure 2.4: Emissive probe characteristics at different probe wire temperature. Figure taken from [Stenzel (1997)].

### 2.2.3 Strongly emitting probe technique

The strongly emitting probe technique of the plasma potential determination is one of the basic emissive probe techniques. It is based on the fact that the floating potential of the emissive probe moves towards the plasma potential if the emission from the probe increases as illustrated in figure 2.4. The dependence of the floating potential on the emission current can be expressed according to [Balan *et al.* (2003)] in case of plasma with Maxwell-Boltzmann distribution for $U_{fl} \leq U_{pl}$ by:

$$U_{fl} = U_{pl} - T_e \ln \frac{I_{es}}{I_{is} + I_{em}}, \tag{2.11}$$

where $I_{es}$ is electron saturation current, $I_{is}$ ion saturation current and $I_{em}$ is emission current from the probe. From this follows that floating potential should attain the plasma potential if $I_{em} = I_{es} - I_{is}$.

However, the situation is more complicated since thermionic emitted current given by eq. 2.7 is limited by space charge formed in front of the emitting probe at strong emission. This is illustrated in figure 2.5, where the potential profile in front of an infinite plane electrode immersed into plasma is schematically depicted

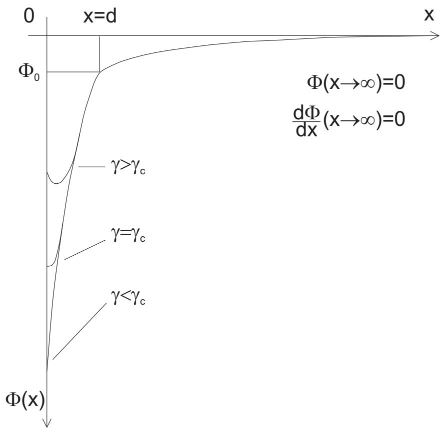

Figure 2.5: Schematic of the potential profile in front of an infinite plane electrode immersed into plasma depicted for different electron emission from electrode described by emission coefficient $\gamma$. Schematic was taken from [Gyergyek & Čerček (2005)].

for various electron emission from the electrode, where the electron emission is described by the emission coefficient $\gamma$. If the emission reaches a certain critical value, $\gamma = \gamma_C$, the electric field in front of the collector becomes zero as indicated in figure 2.5. If the emission is further increased, $\gamma > \gamma_C$, a potential well is formed in front of the collector which then prevents emitted electrons to enter into the plasma.

Effect of the space charge barrier in front of an emissive probe appears as a saturation of the floating potential value in dependence on increasing probe heating (increasing emission) as it is depicted in figure 2.6. The saturation of the floating potential at strong emission from the probe is used as an approximation of the plasma potential in strongly emitting probe technique.

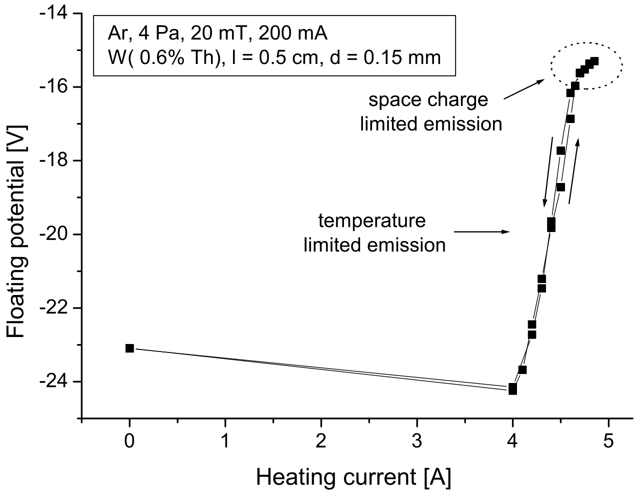

Figure 2.6: Dependence of the floating potential on the probe heating in low temperature plasma of the cylindrical magnetron as determined by current heated emissive probe described in Chapter 3.3.

[Hobbs & Wesson (1967)] showed, that if the temperature of emitted electrons $T_{eW}$ is negligible in comparison to temperature of electrons in plasma $T_e$ (i.e. limit of $T_{eW} \to 0$), the plasma potential valley that is formed at strong emission in front of emitting probe in figure 2.5 is only infinitesimaly deep and the plasma potential determined by strongly emitting probe is then underestimated by approximatively 0.99 $kT_e/e$ in the case of hydrogen plasma and by 1.02 $kT_e/e$ in case of plasma in heavier gas as is e.g. argon. This condition ($T_{eW} \rightarrow 0$) is more or less fulfilled e.g. in hot plasma of fusion devices[1].

In case of low temperature plasma, where the temperature of emitted electrons cannot be neglected in comparison to the electron temperature in plasma, the situation is different. In that case potential valley is formed in front of strongly emitting probe due to the space charge as indicated in figure 2.5 and a difference between the potential measured on the wall at strong emission and the real plasma potential depends on ratio $T_e/T_{eW}$ and plasma density. In general, the plasma potential determined by strongly emitting probe technique in the low temperature plasma is underestimated by less than 0.99 eV, that was underestimating at condition $T_{eW} \rightarrow 0$, and as it was showed e.g. in [Gstrein *et al.* (2006); Ishiguro & Sato (1993)] it can be even overestimated.

Theoretical description of the situation if temperature of emitted electrons cannot be neglected ($T_{eW} \neq 0$) was done in [Takamura *et al.* (2004)] and than extended for two temperature population of plasma electrons in [Gyergyek & Čerček (2005)]. Analytical model developed in [Takamura *et al.* (2004)] was applied in this work for the floating probe condition and is given in detail in Appendix A, its results are shown in Chapter 5.2.

---

[1] e.g. in case of CASTOR tokamak is $T_e = 8 - 25$ eV in edge plasma and $T_e = 150 - 300$ eV in core plasma according to [Balan *et al.* (2003)] and $T_{eW} < 0.32$ eV in case of tungsten since $T \doteq 0.32$ eV is the melting point of tungsten

### 2.2.4 Inflection point in the limit of zero emission technique

An alternative technique for determining of plasma potential by emissive probe is the inflection point in the limit of zero emission method described in [Auciello & Flamm (1989); Smith *et al.* (1979)]. The basic idea of the inflection point technique is to follow the inflection point of the emissive probe I-V characteristic as the emission is varied to the point of zero emission. When space charge effects can be neglected, the inflection point corresponds to the plasma potential. Space charge effects associated with emitted electrons go to zero in the limit of zero emission. Space charge is also reduced by choosing probes of sufficiently small radii. As an example of determination of plasma potential by inflection point in the limit of zero emission technique is given in figure 2.7. This technique is not so perturbing the plasma as the strongly emitting probe technique, enables

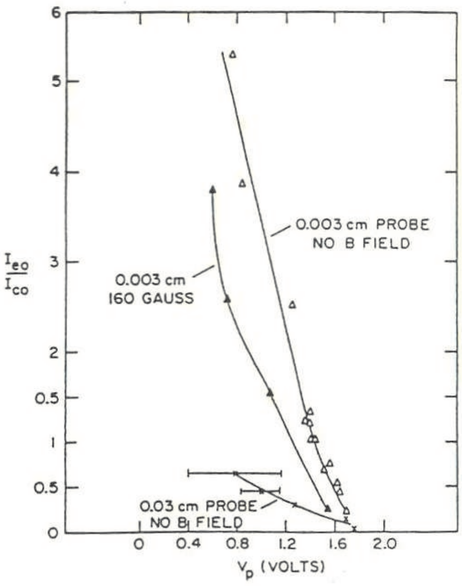

Figure 2.7: Determination of the plasma potential by method of inflection point in the limit of zero emission for different probes and discharge conditions. $I_{e0}$ is electron emission saturation current. Figure is taken from [Auciello & Flamm (1989)].

plasma potential measurements even in non-neutral plasmas in cathode sheaths [Okuno & Fujita (1991)] and also in vacuum [Cho *et al.* (1984)]. On the other hand the determination of plasma potential by the inflection point technique is not direct – i.e. needs capturing of characteristics, emissive current variation and data evaluation. For this reason this technique is not suitable e.g. for study of plasma potential fluctuations.

### 2.2.5 Changes of the electron saturation current of a dc-heated emissive probe

As mentioned at description of the emissive probe characteristics at different probe heating in Chapter 2.2.2, the electron accelerating part of emissive probe characteristic is expected to remain unaffected by electron emission from the probe since the emitted electrons are attracted back to the probe when the probe voltage becomes highly positive with respect to the plasma potential. In first approximation it is true in many cases [Mahdizadeh *et al.* (2005); Wilson *et al.* (2002)].

On the other hand several authors found that electron saturation current varied with different probe heating [Madani *et al.* (2004); Mravlag & Krumm (1990)] as it is illustrated in figure 2.8. Similar variations were observed in measurements in DP-machine in Innsbruck as well as in emissive probe measurements in our experimental device cylindrical magnetron in Prague. Since this problem was to our knowledge not systematically studied and explained yet, the study of variation of the electron saturation current is one of the aims of this part of my thesis.

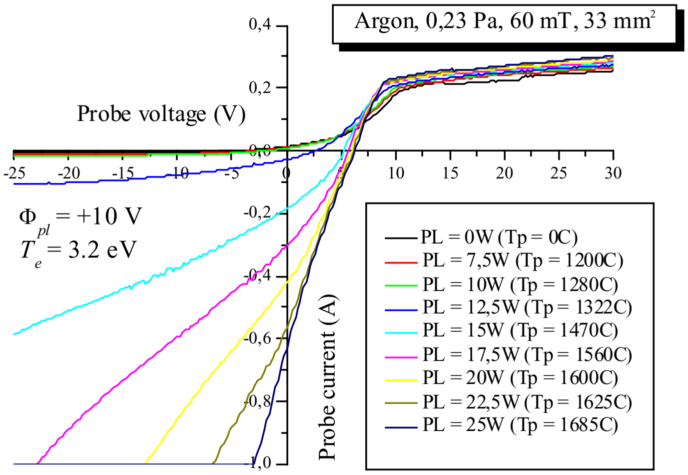

Figure 2.8: $I - V$ characteristics of the laser heated emissive probe with the temperature of the LaB$_6$ probe as parameter. The indicated electron temperature and plasma potential were determined from the cold characteristic for PL= 0 W. Figure is taken from [Madani *et al.* (2004)].

# Chapter 3

# Experimental set-up

## 3.1 Cylindrical magnetron

Major part of the experiments presented in this work was performed in the cylindrical magnetron placed in laboratory of plasma chemistry at the Department of Surface and Plasma Science, Faculty of Mathematics and Physics, Charles University in Prague, Czech Republic. The description of this device was done in detail e.g. in [Holík *et al.* (2002)]. Its scheme is depicted in figure 3.1. It consists of two coaxially placed cylindrical electrodes. The outer discharge electrode with 58 mm in diameter is grounded and serves as anode. The inner coaxially placed water cooled electrode has diameter of 18 mm and serves as cathode. One half of the cathode is segmented and allows therefore measurement of axial distribution of the discharge current in the discharge region. The discharge region is delimited to the length of 300 mm by a pair of limiters held on the cathode potential. Plasma in the magnetron is confined by homogenous magnetic field parallel to the axis. It is created by six magnetic coils and can vary up to 40 mT. The system is evacuated by turbomolecular vacuum pump backed by oil free piston vacuum pump. The ultimate pressure in the system is in the order of $10^{-3}$ Pa. The pressure of the working gas in the system is regulated by MKS flow controller. Discharge in the magnetron is usually produced in noble gases at pressures 1–10 Pa. Discharge is powered by dc power supply – typically in constant current mode at typical discharge currents 100 – 400 mA.

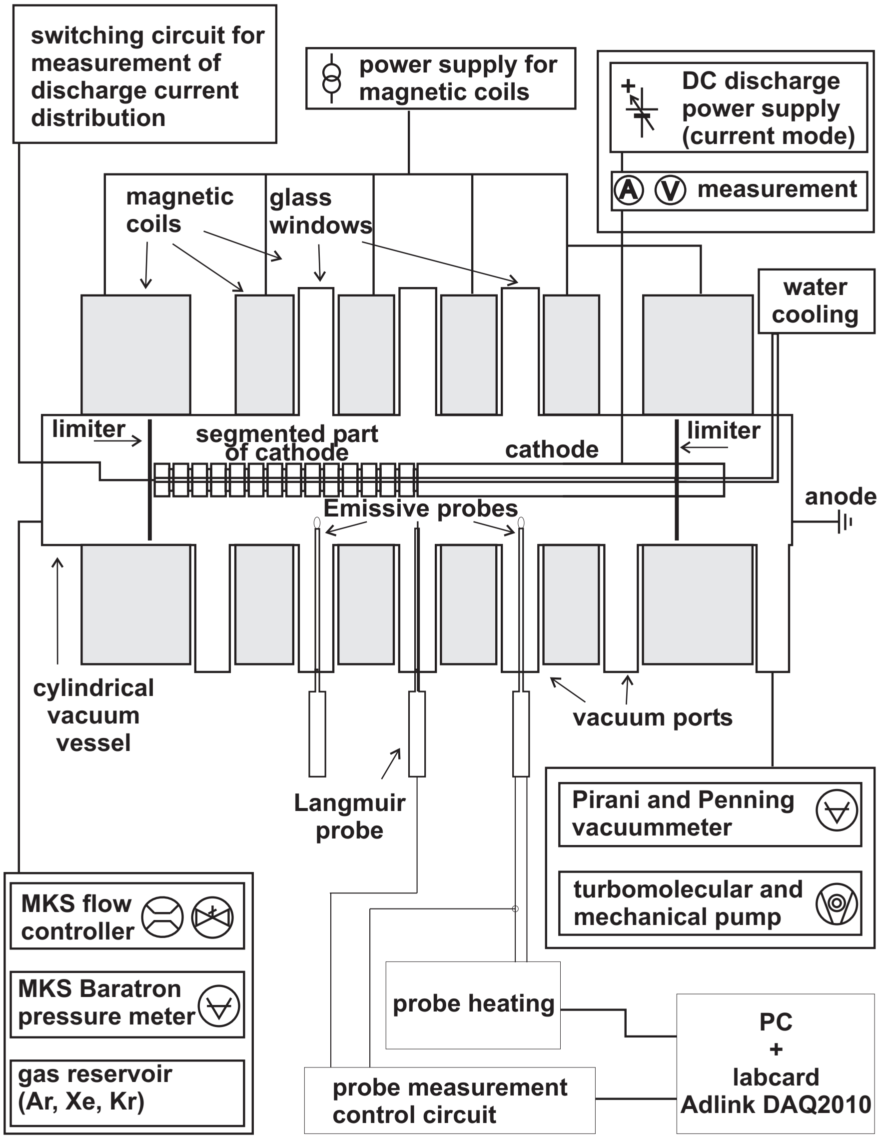

Figure 3.1: Scheme of the cylindrical magnetron; Department of Surface and Plasma Science, Charles University in Prague.

Plasma parameters can be determined by means of electrical probes placed in vacuum ports equidistantly distributed along the discharge region. Composition of the working gas can be analyzed by quadrupole mass analyzer. Typical electron densities achieved in this system are in the order of $10^{16}$ $m^{-3}$. Electron temperature in positive column ranges typically from fractions of electronvolts to a few electronvolts depending on the discharge conditions. Radial profiles of the plasma parameters are similar as those presented for the case of ”shorter” magnetron presented in Chapter 8.1.

In the present experiments, plasma in magnetron was produced in argon at following discharge conditions: Ar, $p = 4$ Pa, $B = 20$ mT, $I = 200$ mA. The plasma was relatively homogeneously distributed along the discharge region at these conditions as shown e.g. in [Holík *et al.* (2002)]. Stability of the discharge was monitored during emissive probe measurements by the floating Langmuir probe placed in the central vacuum port of the magnetron as it is schematically shown in figure 3.1. Thanks to axial homogeneity of the discharge at presented discharge conditions the same plasma conditions could be assumed at position of emissive probes and in-between positioned Langmuir probe.

## 3.2 DP-machine

Part of the experimental work was done in Double Plasma machine (DP-machine) in laboratory of the Experimental plasma physics group at the Institute of Ion Physics and Applied Physics, University of Innsbruck, Austria. DP-machine is schematically depicted in figure 3.2 and it was described e. g. in [Dimitriu *et al.* (2004)]. It consists of a vacuum cylinder of 44 cm in diameter and 90 cm in length. The chamber is divided into a source chamber and a target chamber by a fine-mesh grid. The grid is isolated from the walls and usually biased at about $-100$ V. In each part of the DP-machine a heated double filament of 0.2 mm in diameter tungsten wire serves as hot cathode for a low-temperature discharge in argon. The inner side of the entire chamber is covered by rows of strong permanent magnets with opposite polarity to minimize the plasma-wall interaction. The achievable plasma density lies at discharge current between 50 and 300 mA and Argon pressure between $10^{-2}$ and $10^{-1}$ Pa in the range of $10^{15}$ and $10^{16}$ m$^{-3}$. In the present experiments, plasma was produced only in the target chamber. The discharge was produced in Argon at a pressure of 0.1 Pa and a discharge current of 200 mA which corresponded to a density of about $3 \times 10^{15}$ m$^{-3}$.

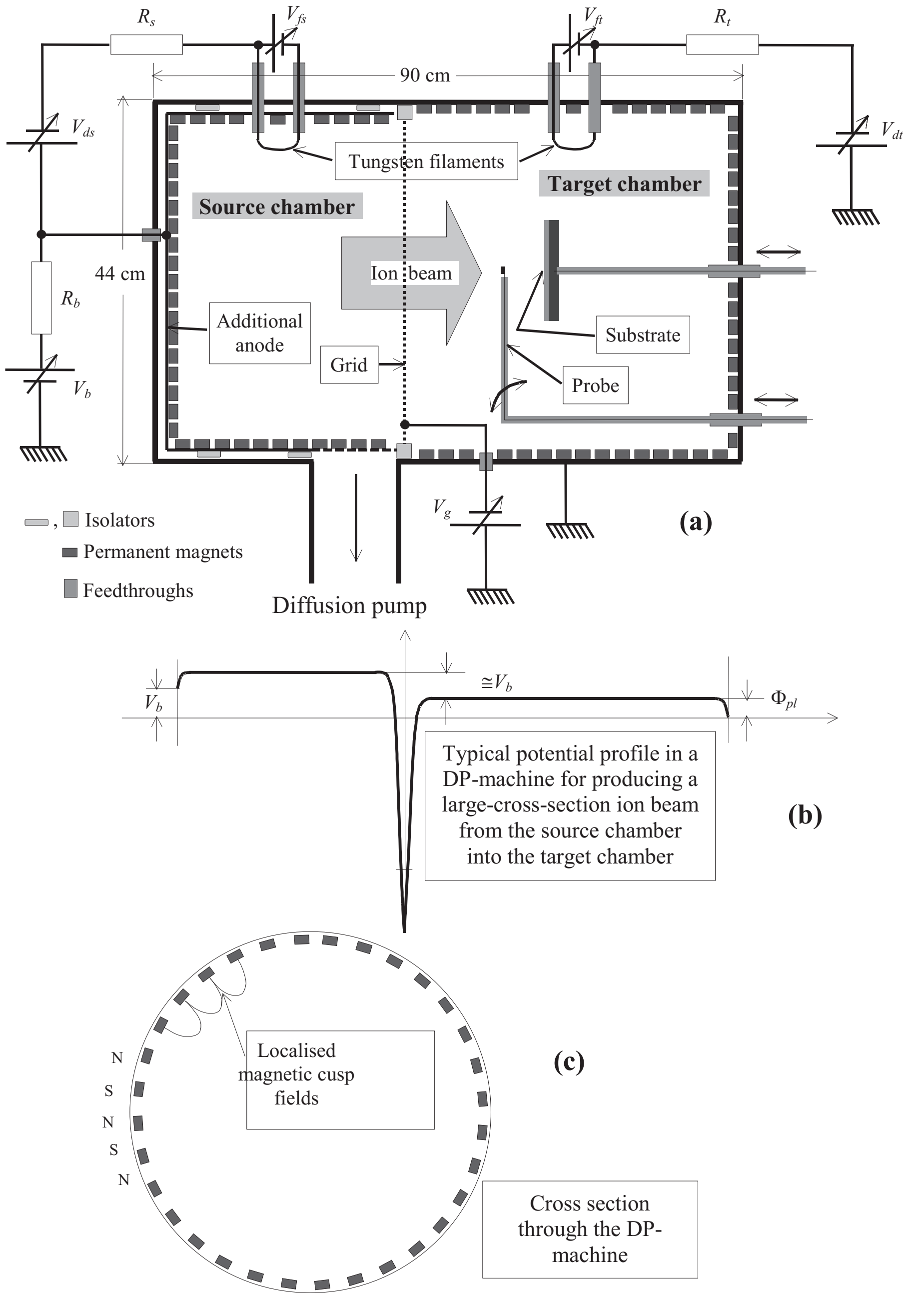

Figure 3.2: Schematics of the DP-machine; Institute of Ion Physics and Applied Physics, University of Innsbruck, Austria. (a) side view of the vacuum cylinder, (b) typical axial potential profile, (c) cross section with permanent magnets.

## 3.3 Emissive probe construction

The construction of emissive probes used in present experiments is depicted in figure 3.3. It was described and discussed in detail in [Siebenförcher & Schrittwieser (1996)]. Photography of used emissive probe is given in figure 3.4. The probe wire was made from tungsten, thoriated tungsten or from tantalum wire with diameter typically $d = 100\ \mu$m. Electrical contact between the probe wire and feeding line was realized by fine copper wires that were tightly bounded around the probe wire. This construction ensured excellent electrical contact and relatively easy probe preparation. Probe was placed into the double bored flat Degusit tube with 2.4 mm in major diameter.

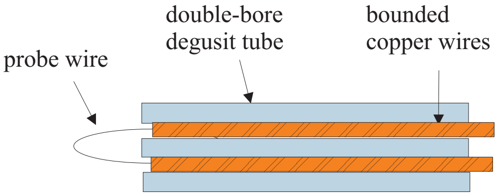

Figure 3.3: Scheme of the emissive probe construction.

Figure 3.4: Photography of emissive probe used in experiments. Author: M. Komm.

Emissive probes were conditioned before measurements by approximatively 10 minutes preheating in vacuum at bright yellow glow in order to evaporate impurities and oxides from the probe surface and also in order to allow the relaxation of the probe material. Furthermore the tungsten wires were cleaned by water solution of $K_3[Fe(CN)_6]$ and Na(OH)[1] prior the probe making in order to clear away graphite layer present on the wire surface due to the technology of the tungsten wire production. Since the described solution dissolves tungsten, the graphite was cleared out together with thin layer of tungsten. The probe wire diameter indicated at results is therefore the diameter measured after cleaning. More careful approach of removal the graphite could be that suggested by [Popov (2006)] – electrolysis in water solution of K(OH).

## 3.4 Probe circuit & data acquisition system

Emissive probe circuit is schematically depicted in figure 3.5. Probe heating was realized by stabilized dc power supply. The probe heating was onset in the constant current mode and after temperature stabilizing (i.e. the probe resistance stabilized) the power supply was switched into the constant voltage mode,

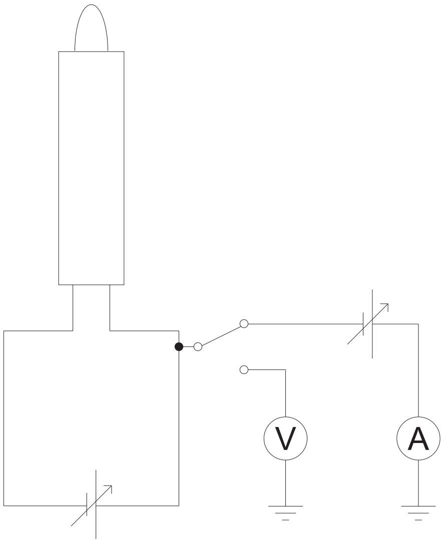

Figure 3.5: Scheme of the emissive probe circuit.

---

[1] Solution composition: 305 g $K_3[Fe(CN)_6]$ + 44.5 g Na(OH) + 1000 ml $H_2O$ – according to [Kohl (1995)].

because this regime ensured better control of the probe wire temperature and it was therefore less dangerous for the hot probe wire[1]. Probe circuit depicted in figure 3.5 was switched between the floating potential measurements mode and the probe voltage-current characteristics measurements mode during experiments. Since the data acquisition circuit was connected to the positive pole of the emissive probe, one half of the heating voltage was subtracted from the probe bias after measurements in order to process the data with the potential at the probe tip.

In case of experiments in the DP-machine the emissive probe current-voltage characteristics were obtained using 1 kHz sawtooth signal and the data were recorded by an oscilloscope. The floating potential of the emitting probe was extra measured manually by multimeter in that case.

In the cylindrical magnetron device the data acquisition was prepared as fully computer controlled because it was planned to obtain large amount of data. Data acquisition in the cylindrical magnetron was realized via labcard Adlink DAQ2010 in combination with devices connected to the computer via GPIB interface. The measurements were governed by program created in Agilent VEE environment. The current-voltage characteristics were measured step by step in this case. The output signal from the labcard was amplified by operational amplifier powered by batteries that avoided next source of the noise coming from the net ground. The amplified voltage applied on the probe and the probe current were measured after proper transformations also by labcard Adlink DAQ2010. Each point of characteristic was averaged from 50 samples in order to suppress the noise of the cylindrical magnetron discharge. Extra measurement of the floating potential of the emissive probe was realized by multimeter connected to computer via GPIB interface as well as it was done in case of the computer controlled power supply used for the emissive probe heating. Simultaneously with the emissive probe measurements the floating potential of the Langmuir probe placed in central vacuum port was measured by another multimeter connected via GPIB interface

---

[1] Constant voltage mode acts as negative feedback for changes of the probe wire resistance caused by additional probe heating due to electron current flowing from plasma to the probe if positively biased or due to evaporating of the probe material. Constant current mode acts vice versa and an increase of the wire resistance results in additional increase of the applied power.

in order to monitor possible influence of the high electron emission from the emissive probe on the discharge.

# Chapter 4

# Results

We tried to found sufficient experimental evidence to characterize the variation of the electron saturation current that was observed with increasing probe heating in previous experiments. The study was done in two types of plasma – a cylindrical magnetron plasma and the non–magnetized plasma of a DP machine. Two possible explanations for such changes were considered: (a) the influence of the space charge around the probe shaft, (b) the change of the probe material work function due to the probe heating. In order to assess importance of these effects the emissive probes with three different loop lengths (3, 5 and 10 mm in the magnetron plasma and 5, 10 and 20 mm in the DP–machine) were used to check on hypothesis (a), and three different materials (W, thoriated W [with 0.6 % Th] and Ta) to check on hypothesis (b). Characterization of changes of the electron saturation current at varying probe heating was the aim of present work since this phenomenon was not, to our knowledge, systematically studied and explained as yet.

An example of experimental results obtained in cylindrical magnetron is given in figure 4.1 where emissive probe characteristics are depicted at different probe heating. Increase of the ion-accelerating part of the probe characteristic due to the superimposition of the emitted electrons to the ion current is well pronounced there as well as the changes of the electron saturation current at increasing probe heating. Variation of the electron saturation current shows in detail figure 4.2 where the electron saturation current is picked out from characteristics at fixed voltage and plotted versus the probe heating current. Fixed voltage was chosen

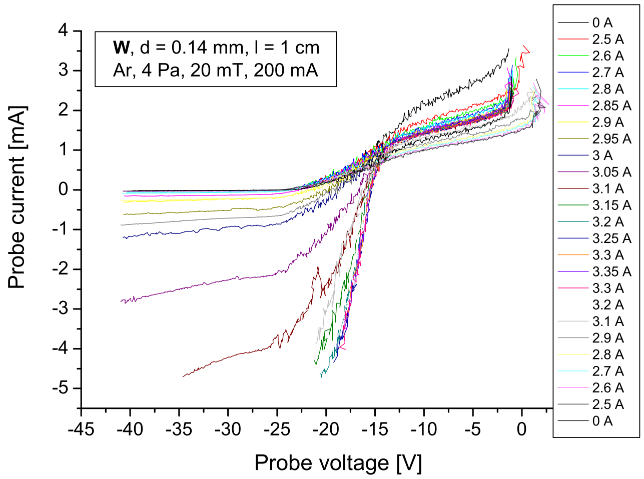

Figure 4.1: Probe#79 – W, $d = 0.14$ mm, $l = 10$ mm. Emissive probe characteristics for different probe heating current (50× averaged).

appropriately far from the plasma potential since at higher probe voltage the variation is more pronounced. Linear fit of the electron saturation current was used in vicinity of the chosen voltage in order to suppress the noise.

The typical electron saturation current profile is depicted in figure 4.2. The current steadily decreased at increasing probe heating almost till the maximal accessible probe heating. At the maximal probe heating the electron saturation current slightly increased and then again steadily decreased as the heating current was lowered down to approximately 2.5 A. In the remaining part of the profile (the heating current was decreased towards zero) the electron saturation current grew from minimum of 1.2 mA to 1.4 mA at zero probe heating. The depicted dependence of the electron saturation current on the probe heating is not reversible. That gives evidence that the probe parameters or the plasma properties changed during experiment. Great care about experimental conditions has to be therefore taken to characterize the electron saturation current variations.

The probes were cleaned and conditioned before experiment as described in Chapter 3.3 by approximately 10 minutes of preheating at bright yellow glow in vacuum in order to avoid interlacing of the effects caused by the probe surface

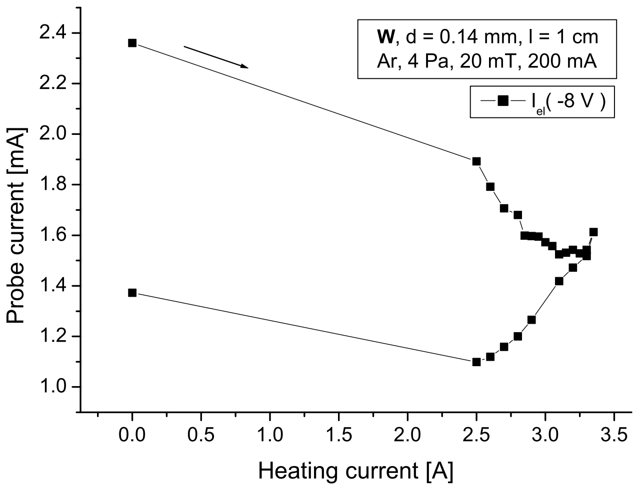

Figure 4.2: Probe#79 – W, $d = 0.14$ mm, $l = 10$ mm. Dependence of the electron saturation current on the probe heating. Arrow indicates data points sequence.

itself and by electrical junctions conditioning into studied electron saturation current variations. Probes were afterwards once more shortly preheated (for approximatively 1-2 minutes) directly before measurements in order to clean the probe surface from impurities and adsorbed working gas. Further, the probe current was limited during experiments in the cylindrical magnetron device, where the probe characteristics were obtained point to point, since the large current flow through the probe could be dangerous for the probe and it could also readily influence the discharge. The emission current was usually limited to $-5$ mA in the ion acceleration region and the electron saturation current was usually limited to approximately 3 mA – depending on the probe properties. The probe current limitation was needed at both polarities since the discharge started to burn to the probe if it was highly positively biased with respect to the plasma potential. That can be seen from the increase of the electron saturation current in figure 4.1 at maximum positive probe bias.

Stability of the discharge was monitored by the floating Langmuir probe placed in the central vacuum port of the magnetron during emissive probe measurements and by observing the changes in the discharge voltage. Data that correspond to the emissive probe characteristics given in figure 4.1 are presented in figure 4.3 together with the dependence of the floating potential of the emissive probe on

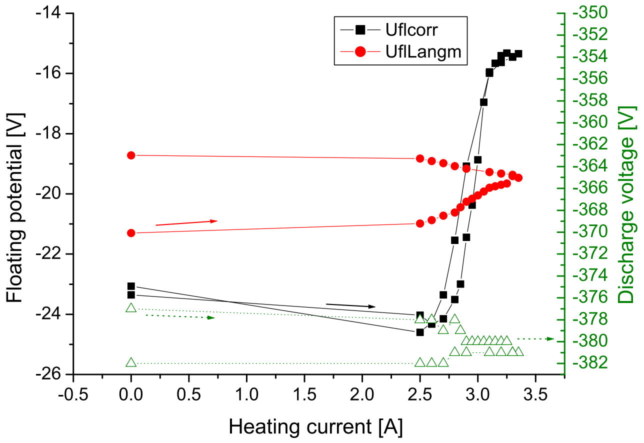

Figure 4.3: Probe#79 – W, $d$ = 0.14 mm, $l$ = 10 mm. Dependence of the floating potential of emissive probe on the probe heating (■) and characterization of stability of the discharge during experiment monitored by floating Langmuir probe (•) and by changes in discharge voltage (△). Arrows indicate data points sequence.

the probe heating current. The ordinate of the point of saturation of the floating potential profile of the emissive probe in dependence on the heating current at the high probe heating depicted in figure 4.3 indicates the plasma potential as determined by strongly emitting probe technique (see Chapter 2.2.3). Reversibility of the floating potential of the emissive probe at various probe heating gives an important measure of the reliability of the data and of the emissive probe condition[1]. It is useful because tungsten of the probe wire can evaporate readily

---

[1] Since the $U_{fl}$ depends on the electron emission from the probe and the electron emission is bound exponentially with the probe wire temperature in case of the temperature limited emission (see eq. 2.7), already small difference in probe resistance (affecting of the probe by evaporation) appears as an hysteresis in the dependence of the floating potential of emissive probe on the heating current, because a smaller heating is needed for sustaining the same emission in that case.

during experiment if the heating current is set too high or if it is set for too long time. The applied heating power is furthermore concentrated at the place with highest resistance (i.e. at the hottest point of probe wire) giving the positive feedback for more intensive tungsten evaporation, because the Ohmic losses are higher there.

According to this consideration, the probe corresponding to data given in figure 4.3 was in good condition since the hysteresis of the floating potential in dependence on the heating current was comparatively small. Especially at considering that it can be partially ascribed to the probe holder thermal inertia. As it can be seen in figure 4.3, the discharge was stable and unaffected substantially by the emitting probe in this case. The discharge voltage changed only negligibly – by about 4 V what is roughly 1 % of applied voltage – and totally independently on the emission from the probe during measurements. The small increase of the discharge voltage in this particular case was probably caused by cleaning of the argon discharge from impurities with lower ionization treshold during experiment. The steady increase of the floating potential of the Langmuir probe in figure 4.3 can be attributed to covering of the probe surface by sputtered metal and to adsorption of argon gas on the probe surface since the same trend was found in all measurements even if the discharge voltage didn't change at all. Furthermore the floating potential determined by the emissive probe without any applied heating at the beginning and at the end of the experiment coincided with each other as it can be seen in figure 4.3 and confirmed in this way that the plasma parameters remained unaffected and the discharge was stable during the presented experiment.

Stability of experimental conditions was controlled in the way described above in all emissive probe measurements performed in the cylindrical magnetron plasma that are presented in this work.

In the case of former experiments performed in the DP-machine the discharge conditions were not so attentively monitored as in the case of latter experiments in the cylindrical magnetron. Therefore possible influencing of the DP-machine plasma by the emitting probe have to be discussed and eventually taken into an account in interpreting of the emissive probe data obtained there as it will be done later in this work.

## 4.1 Characterization of the electron saturation current variations

In order to characterize electron saturation current variations at varying emissive probe heating comparatively large data set was obtained in the cylindrical magnetron and in the DP-machine plasma for different probe parameters as described at the beginning of the Chapter 4. In order to validate the obtained data at least three specimens of the probe with the same parameters were prepared and their results were compared with each other to assess the error of measurements in the case of cylindrical magnetron. Three examples of such comparison that shows reproducibility of the emissive probe results are given in figures 4.4, 4.5 and 4.6.

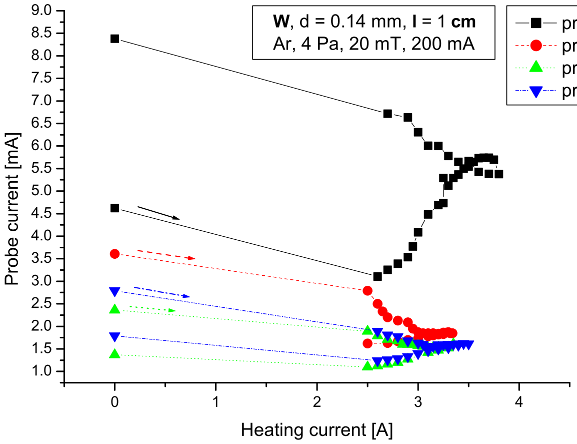

Figure 4.4: Comparison of the electron saturation current variation in dependence on the probe heating for three specimens of the W, $d = 0.14$ mm, $l = 10$ mm probe in the cylindrical magnetron plasma.

Whereas in the cases of data depicted in figures 4.4 and 4.5 all probe specimens were in good condition during the whole measurement (i.e. with practically no hysteresis in the dependence of the floating potential on the heating current similarly as it was for the probe#79 in figure 4.3), the specimens in the figure 4.6 were partially affected by stronger probe material evaporation at high

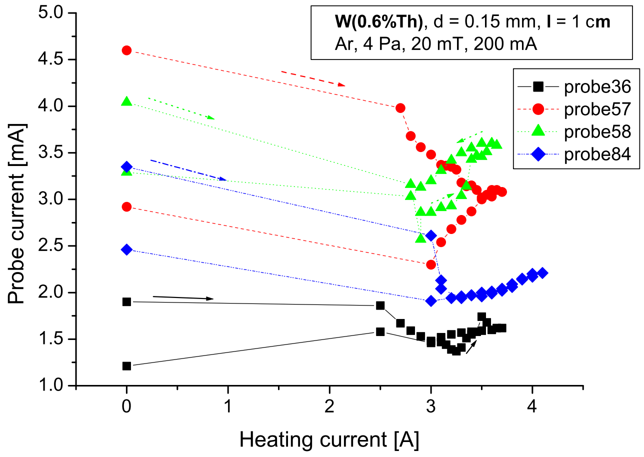

Figure 4.5: Comparison of the electron saturation current variation in dependence on the probe heating for four specimens of the W(0.16% Th), $d = 0.15$ mm, $l = 10$ mm probe in the cylindrical magnetron plasma.

probe heating current. That is displayed as hysteresis in the dependence of the floating potential on the heating current and in distortion of the shape of the electron saturation current variations. The hysteresis in the dependence of the floating potential on the heating current is showed as an example for the case of the probe#49 in figure 4.7. The measurements were in general more difficult with shorter probes and it was more demanding to keep them unperturbed by probe wire evaporation.

From the data depicted in figures 4.4 and 4.5 it is possible to see that the profiles of the electron saturation current differed although probes with the same parameters were prepared and the discharge was stable and probes were not affected by extreme probe wire thickness changes. These data shows complexity of presented measurements. However, similar shape of electron saturation current variations can be found in the most of undisturbed data. As the representative data can be taken from probes#53, #79 and #80 in figure 4.4 or probe#57 and #84 in figure 4.5. Those profiles show steadily decrease almost till the maximum heating where they increased a little bit. At consecutive decrease of emission the

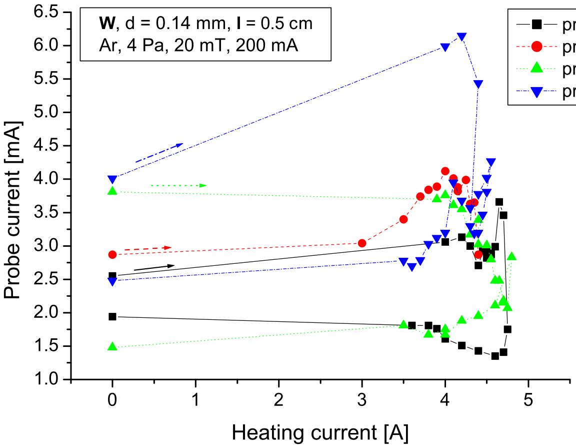

Figure 4.6: Comparison of the electron saturation current variation in dependence on the probe heating for four specimens of the W, $d = 0.14$ mm, $l = 5$ mm probe in the cylindrical magnetron plasma.

electron saturation current decreased again and finally grew up to the value at the zero heating, that was smaller than the starting one.

In case of the DP-machine measurements the trend of variations was different – typically steadily increasing as displayed in figure 4.8 for tantalum probes or in figure 4.9 for tungsten probes, although the trend was not so clear in case of figure 4.9. Unfortunately the data collected in DP-machine were obtained only at increasing probe heating that was increased till overburning of the probe. Therefore there is not available the information about the probe condition as it was in the case of the cylindrical magnetron data. However, steady increase of the electron saturation current at increasing heating is characteristic for DP-machine results.

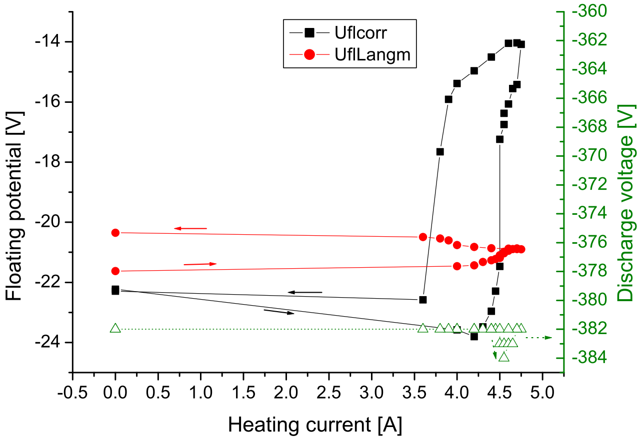

Figure 4.7: Probe#49 - W, $d = 0.14$ mm, $l = 5$ mm. Dependence of the floating potential of emissive probe on the probe heating (■) and characterization of stability of the discharge during experiment monitored by floating Langmuir probe (•) and by changes in discharge voltage (△). Arrows indicate data points sequence.

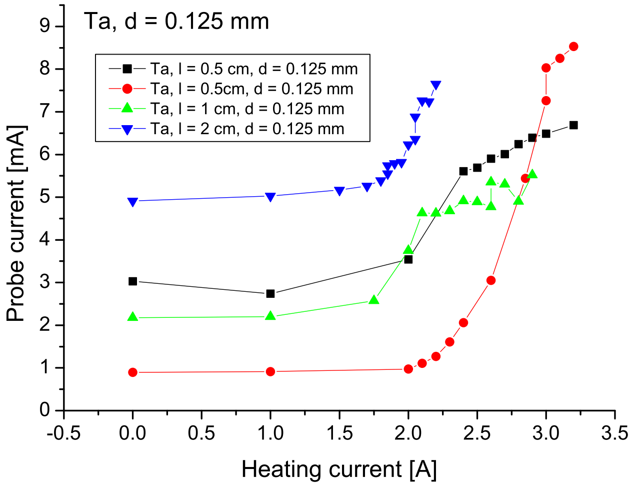

Figure 4.8: Comparison of the electron saturation current variation in dependence on the probe heating for tantalum probes in the DP-machine.

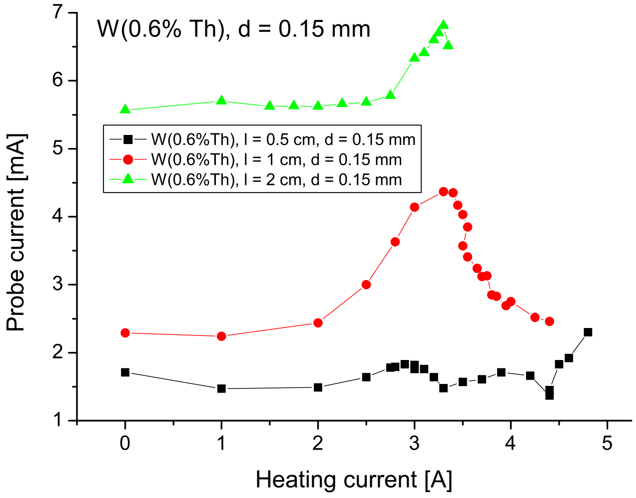

Figure 4.9: Comparison of the electron saturation current variation in dependence on the probe heating for W(0.6% Th) probes in the DP-machine.

## 4.2 Magnitude of changes

Although the electron saturation current did not change with increasing heating in the same way in all cases and some probes were partially affected by stronger evaporation at the high probe heating, it was possible to quantitatively describe and compare the magnitude of changes induced by varying probes heating in both types of plasma and to find the sufficient experimental evidence for investigation of the dependence of magnitude of changes on the probe length and on the probe material to prove ideas suggested at the beginning of Chapter 4 this way. To that end the variations of the electron saturation current were simply characterized as the difference of the extreme values. Only the extreme values before reaching the maximum probe heating were chosen in order to minimize the effect of the probe wire evaporation. Figure 4.10 shows the difference in electron saturation current

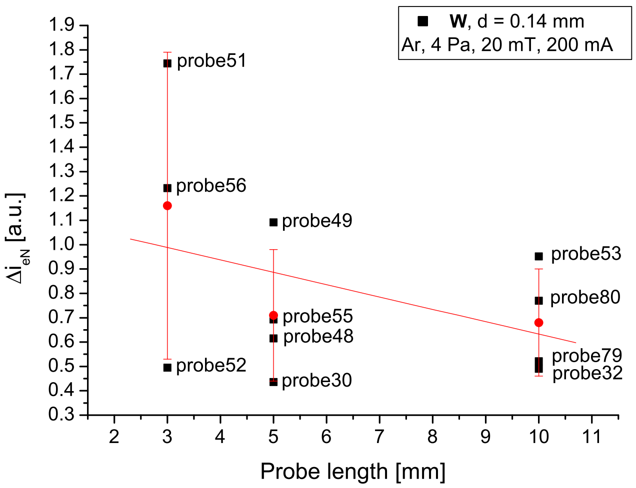

Figure 4.10: Difference in electron saturation current for tungsten with $d = 0.14$ mm wire probes for three different probe lengths normalized on the electron saturation current at the maximal probe heating. Data were obtained in the cylindrical magnetron.

for tungsten with $d = 0.14$ mm wire probes for three different probe lengths gained from the cylindrical magnetron data. Each point represents several different realization of a probe. The data on the ordinate axis of figure 4.10 are normalized to the electron saturation current collected by the probe at the maximum probe heating, which characterizes the emitting area. Figure 4.10 clearly shows that the magnitude of changes of the electron saturation current ($\triangle i_{es}$) decreases as the probe length increases; the decreasing trend is indicated by linear regression. Similar trend was observed in the case of W(0.6 % Th) probes too; the results are displayed in figure 4.11. Measurements with tantalum probes were unfortunately too complicated[1] and for that reason satisfactory data set was not obtained for comparison with the data with W and W(0.6 % Th) in the cylindrical magnetron case.

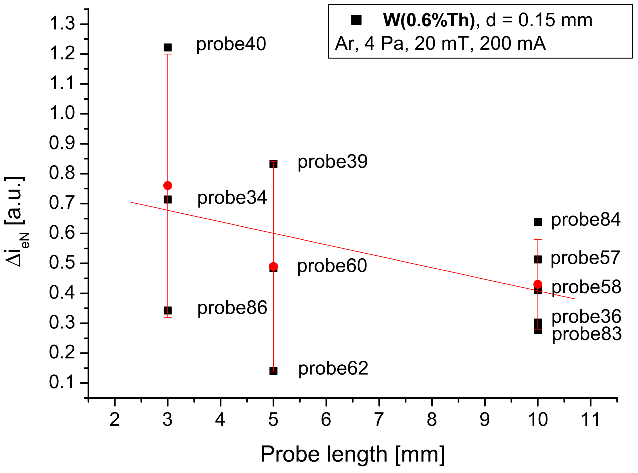

Figure 4.11: Difference in electron saturation current for W(0.6% Th), $d$ = 0.15 mm wire probes for three different probe lengths normalized on the electron saturation current at the maximal probe heating. Data were obtained in the cylindrical magnetron.

---

[1] Difficulties with tantalum probes were probably connected to the dielectric oxide film ($Ta_2O_5$) on the probe wire surface since the electrical contact with the bounded copper wires was difficult to establish if not mechanically cleaned. Furthermore tantalum partially works as a "getter" and $Ta_2O_5$ can therefore diffuse also into the probe wire volume.

A comparison of trends of $\triangle i_{es}$ for W and W(0.6 % Th) is given in figure 4.12 that shows that for all the probe lengths that difference in electron saturation current normalized on the electron current at maximal probe heating was systematically higher for tungsten wire. It has to be noted that the difference was not caused by the different wire diameter, since this acts in opposite sense: at larger probe wire diameter the difference of the electron saturation current is systematically higher as it can be seen in figure 4.13. The data depicted in figure 4.12 shows that the magnitude of variations of the electron saturation current depends not only on the probe length but also on the probe material.

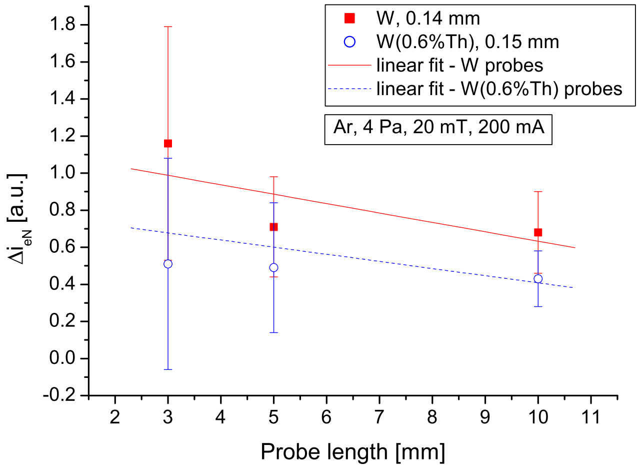

Figure 4.12: Comparison of trends in variations of the electron saturation current for W and W(0.6% Th) probes in the cylindrical magnetron plasma.

The data of Prague's cylindrical magnetron presented above are backed up by measurements done in the Innsbruck DP–machine in a different type of plasma. Electron saturation current variations were processed in the same way as described in the case of data obtained in the cylindrical magnetron and resulting data are depicted in figure 4.14 that shows that the variations were less pronounced in the case of longer probes similarly as it was in the case of probes in the cylindrical magnetron.

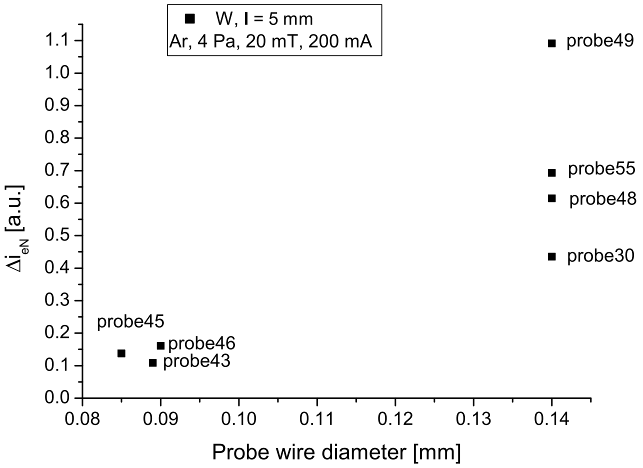

Figure 4.13: Dependence of the $\triangle i_{eN}$ on the probe wire diameter. Data were obtained in the cylindrical magnetron.

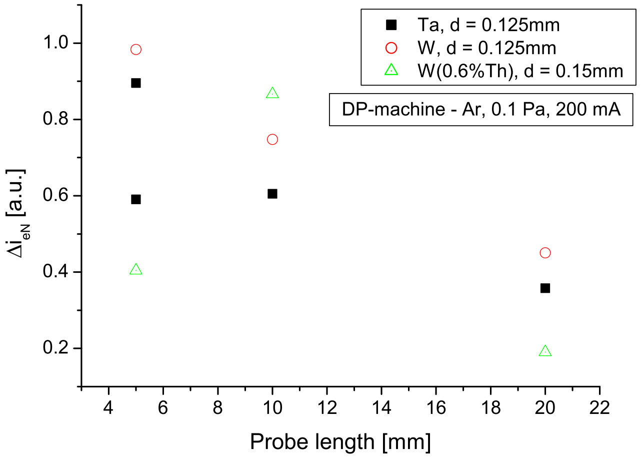

Figure 4.14: Difference in the electron saturation current normalized on the electron saturation current at the maximal probe heating as obtained in the DP-machine.

## 4.3 Overestimation of the plasma potential by the strongly emitting probe

According to the review given in the Chapter 2.2.3 the plasma potential determined by the strongly emitting probe technique should be lower than the real plasma potential if the temperature of emitted electrons can be neglected (according to [Hobbs & Wesson (1967)] by about $kT_e/e \doteq 1$). If the temperature of emitted electrons cannot be neglected and is sufficiently large the plasma potential determined by the strongly emitting probe can be even more positive than the real plasma potential.

The plasma potential determined by strongly emitting probe technique in the cylindrical magnetron plasma as well as in the case of DP-machine plasma exceeded substantially the real plasma potential as it is illustrated in figure 4.15. The real plasma potential was determined from the second derivative of Langmuir probe characteristic obtained by Langmuir probe placed at the same radial

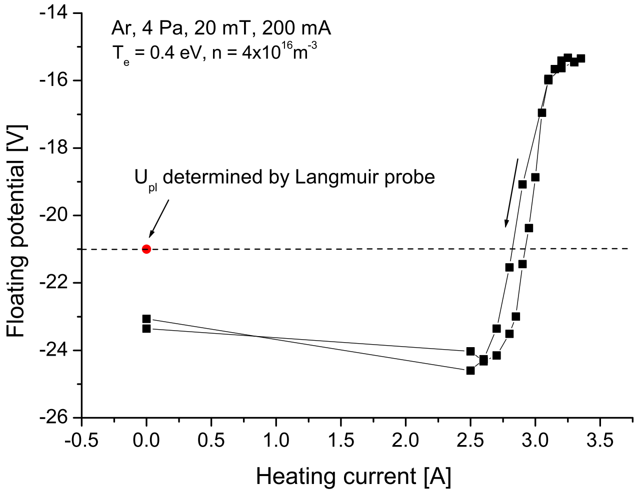

Figure 4.15: Illustration of overestimating of the plasma potential by strongly emitting probe in the cylindrical magnetron plasma. Probe#79 – W, $d$ = 0.14 mm, $l$ = 10 mm.

| Probe No. | $l$[mm] | $U_{pl}$[V] | $T_e$[eV] | $U_{plEM}$[V] | $\Delta U_{pl}$[V] |
|---|---|---|---|---|---|
| 84 | 10 | -22 | 0.42 | -17.56 | 4.44 |
| 83 | 10 | -22 | 0.54 | -17.16 | 4.84 |
| 57 | 10 | -19 | 0.4 | -16.3 | 2.7 |
| 58 | 10 | -19 | 0.4 | -15.8 | 3.2 |
| 36 | 10 | -22 | 0.35 | -19.9 | 2.1 |
| 32 | 10 | -24 | 0.42 | -18.5 | 5.5 |
| 62 | 5 | -20 | 0.7 | -15.3 | 4.7 |
| 39 | 5 | -22 | 0.46 | -18.4 | 3.6 |
| 40 | 3 | -20 | 0.5 | -16.1 | 3.9 |
| 33 | 3 | -22 | 0.5 | -19.56 | 2.44 |
|  |  |  |  |  | $average = 3.74$ |

Table 4.1: Overestimation of the plasma potential via strongly emitting probe technique in the cylindrical magnetron plasma, where $U_{plEM}$ is plasma potential determined by strongly emitting probe: W(0.6 % Th), $d = 0.15$ mm.

position as the emissive probe tip in the cylindrical magnetron case and further confirmed (within the experimental error) by the plasma potential derived from characteristic of the emissive probe without applied heating. The above mentioned experimental error was connected mainly with the fact that the plasma potential was averaged along the whole emissive probe loop in the case of the cold emissive probe whereas in the case of the strongly emitting probe the potential at the probe tip was determined. However, the difference is small in the positive column region. In the case of DP-machine data the plasma potential determined by strongly emitting probe technique was compared only with the plasma potential derived from characteristic of the emissive probe without applied heating. That gave sufficient measure of the plasma potential at position of the emissive probe tip since the plasma parameters did not substantially vary along the probe wire in the DP-machine too.

Overestimation of the plasma potential by strongly emitting probe was relatively extensive in case of the cylindrical magnetron as it is documented in tables 4.1, 4.2 and 4.3 for different probe materials. The overestimation was in the range of 2.1–5.5 V for the W(0.6 % Th), $d = 0.15$ mm probes giving 3.74 V in

| Probe No. | $l$[mm] | $U_{pl}$[V] | $T_e$[eV] | $U_{plEM}$[V] | $\Delta U_{pl}$[V] |
|---|---|---|---|---|---|
| 80 | 10 | -21.3 | 0.48 | -15.37 | 5.93 |
| 79 | 10 | -21 | 0.4 | -15.34 | 5.66 |
| 53 | 10 | -20 | 0.8 | -15.77 | 4.23 |
| 55 | 5 | -20.2 | 0.36 | -15.75 | 4.45 |
| 49 | 5 | -20.7 | 0.55 | -14.1 | 6.6 |
| 48 | 5 | -19.6 | 0.63 | -15.54 | 4.06 |
| 56 | 3 | -21.7 | 0.42 | -15.3 | 6.4 |
| 52 | 3 | -19 | 0.5 | -14.8 | 4.2 |
| 51 | 3 | -19.8 | 0.49 | -15.2 | 4.6 |
| | | | | | $average = 5.13$ |

Table 4.2: Overestimation of the plasma potential via strongly emitting probe technique in the cylindrical magnetron plasma: W, $d = 0.14$ mm.

| Probe No. | $l$[mm] | $U_{pl}$[V] | $T_e$[eV] | $U_{plEM}$[V] | $\Delta U_{pl}$[V] |
|---|---|---|---|---|---|
| 46 | 5 | -22 | 0.65 | -15.4 | 6.6 |
| 45 | 5 | -21 | 0.3 | -14.1 | 6.9 |
| 43 | 5 | -21 | 0.4 | -14.1 | 6.9 |
| | | | | | $average = 6.8$ |

Table 4.3: Overestimation of the plasma potential via strongly emitting probe technique in the cylindrical magnetron plasma: W, $d \doteq 0.09$ mm.

average. For the W, $d = 0.14$ mm probes it was in the range of 4.1–6.6 V giving 5.13 V in average and for W, $d \doteq 0.09$ mm probes it was in the range of 6.6–6.9 V giving overestimation of the plasma potential by 6.8 V in average. The plasma density was in the order of $n = 10^{16}$ m$^{-3}$. Electron temperature of the body of the distribution function, that was determined for each probe and is given at the data in tables, was typically $T_e = 0.5$ eV. Whereas the overestimation of the plasma potential by the strongly emitting probe differed for different probe wire thickness and material it did not significantly depend on the probe wire length.

Overestimation of the plasma potential in case of the DP-machine was $2 - 4$ V depending on the probe parameters. The plasma conditions were typically $n_e \leq 10^{16}$ m$^{-3}$ and $T_e = 2 - 3$ eV. The overestimation of the plasma potential in the DP-machine device as well as variations of the electron saturation current at varying probe heating are shown in more detail for the case of DP-machine in [Gstrein *et al.* (2006)] that is attached in Appendix D.

The overestimation of the plasma potential by strongly emitting probe is also readily seen in radial plasma potential profile depicted in figure 10.7. There are shown data measured by M. Komm by means of strongly emitting probe in the ”shorter” cylindrical magnetron that is described in Chapter 8.1. The plasma potential should tend to zero at the position of the grounded anode instead of approximatively 3 V determined by strongly emitting probe technique as depicted in figure 10.7.

# Chapter 5

# Discussion

## 5.1 Characterization of electron saturation current variations

Studied variations of the electron saturation current in dependence at the varying probe heating had different profile in the cylindrical magnetron plasma and in the DP-machine plasma. Whereas in the DP-machine the electron saturation current typically increased at increasing probe heating, in case of the more extensive experiment in the cylindrical magnetron the electron saturation current typically steadily decreased almost till the maximal probe heating where it increased a little bit and during the following decreasing of emission the electron saturation current decreased again and finally grew up to the value at the zero heating as described in Chapter 4.1 and depicted e.g. in figure 4.2. The profile of the electron saturation current depicted in figure 4.2 is characteristic for the data obtained in the cylindrical magnetron. The initial decrease of the electron saturation current at increasing probe heating was not present in all cases as can be represented e.g. by probe#55 in figure 4.6. (This probe was affected by stronger evaporation at higher probe heating that lead to deformation of the electron saturation current variations in the last part of profile. However, it is obvious that at the beginning, where the probe was in a good condition, the electron saturation current readily increased with increasing heating, analogous to the DP-machine data.)

The electron saturation current variations were recorded during increasing as well as afterwards at decreasing probe heating in the cylindrical magnetron. This gives better experimental base for explanation of observed variations and for assessing their dependence on the electron emission from the probe. As can be seen in all presented cylindrical magnetron data (figures 4.2, 4.4, 4.5 and 4.6) the variations of the electron saturation current on the probe heating was not reversible. The studied variations can be therefore divided into reversible variations connected with varying electron emission from the probe and into the non-reversible changes connected with the change of experimental conditions.

### 5.1.1 Non-reversible changes

The non-reversible changes of the emissive probe properties are displayed in the marked decrease of the collected electron saturation current during the variation of the probe heating. As described above, they are combined with the studied electron saturation current variations in dependence on the electron emission from the probe. Presence of the non-reversible changes in collected electron saturation current gives an evidence that the probe parameters or the discharge properties changed during experiment.

The discharge parameters were monitored during experiment as described at the beginning of Chapter 4. They were practically stable in most cases as is illustrated by data given in figures 4.3, 4.7 and 4.15. From that follows that the discharge was not influenced in global scale by emitting probes in presented experiments. That is why the non-reversibility of the electron saturation current should be ascribed to non-reversible changes of the emissive probe properties although they were tried to be minimized by probes conditioning before measurements and by the care that was taken to the probes condition during experiment as described in Chapter 3.3 and 4.

The following processes inducing the permanent probe parameters change leading into decrease of the electron saturation current can be considered:

1. probe wire evaporation, that reduces the area of the probe surface
2. change of the work function of the emitting surface due to probe material recrystallization (e.g. in case of tungsten the work function differs in range

4.3–6 eV depending on the emitting crystal face and the value $\chi = 4.5$ eV is for polycrystalline surface.)

3. change of the emitting area
4. changes of resistance in the junction of the probe wire with bounded copper feeding line
5. in case of cylindrical magnetron: change of the emissive probe area due to destroying of possible contact with metallic layer deposited on the probe holder

The relevancy of suggested processes can be discussed on the example of the Probe#79. The electron saturation current variations recorded by this probe are depicted in figure 4.2. Obtained profile readily exhibits discussed features. The data monitoring the discharge stability and the probe condition are depicted in figure 4.3 – this probe was not affected by extreme probe wire evaporation and also the discharge was relatively stable[1].

Electron saturation current decreased to one half of its initial value during measurements in case of Probe#79 as it is shown in figure 4.2. It cannot be explained only by reduction of the probe area due to the probe evaporation as was suggested in the first point since the area of the probe $A_p$ is proportional to probe wire radius ($A_p \sim r_p$) whereas the probe wire resistance $R_p$ is inversely proportional to its square ($R_p \sim r_p^{-2}$). Any noticeable probe surface area reduction would be therefore readily seen in hysteresis of the emissive probe floating potential since the increase of probe wire resistance due to probe material evaporation would express itself in lower probe heating current sufficient for achieving the same probe tip temperature and it was not observed in figure 4.3. Furthermore the evaporation is more pronounced on the hottest place (usually the probe tip) and surface area change is therefore small even at strong affecting of the probe tip.

To the second mentioned process: The work function could change during the probe heating. Especially in case of the thoriated probes, where the work function

---

[1] See discussion at description of the data depicted in figure 4.3 in Chapter 4.

of the thorium is substantially lower than in the tungsten case and final probe wire work function depends on its concentration on the probe surface. However, such changes of the work function can influence only the electron emission and cannot explain the difference in electron saturation current values recorded at zero heating – at the beginning and at the end of measurement.

For the same reason the process suggested in the third point can be excluded: Changes of the size of emitting area during experiment cannot explain difference in electron saturation current at zero emission, although the size of emitting area probably decreased during experiment because of two previously described processes (evaporation and the work function change) that are temperature induced.

Next suggested process was the change of contact resistance between the copper feeding line and the probe wire, that was realized by bounding of thin copper wires. Although, the copper wires even annealed in some cases the resistance change of this junction are negligible in comparison to the resistance of the plasma and also any non-negligible change would be visible in figure 4.3.

The last suggested process was the change of the probe area caused by destroying of the contact between metallic layer deposited on the ceramic probe holder and the probe wire at high temperature. In the cylindrical magnetron discharge the material from cathode is sputtered. Covering of the ceramic probe holder by sputtered material sputtered is evident after some time of discharge operation. The contact between this layer and the probe wire can readily increase the probe collecting area. Destroying of the contact can be therefore an explanation of the non-reversible changes in the electron saturation current observed in the cylindrical magnetron data.

### 5.1.2 Reversible variations

The reversible variations of electron saturation current in dependence on varying probe heating, that were combined with non-reversible ones, are those connected with emission of electrons from the probe.

Reversible variations of the electron saturation current are roughly similar to the electron saturation current profile of the probe#84 in figure 4.5 at decreasing probe heating – the electron saturation current decreases at increasing probe heating at the beginning till the onset of the electron emission from the probe wire (it was at $I_{HEAT} = 3.3$ A in the case of probe#84) and than increases with increasing electron emission till the value at the maximal probe heating.

The minimum of above described profile of the probe#84 in figure 4.5 corresponds roughly to onset of emission, as mentioned above. From that it follows that already the heat transfer to the probe shaft or the temperature induced processes on the probe wire can significantly influence collected electron saturation current since no emission is present at low probe heating. Observed decrease can be connected with cleaning of the thin metallic layer that was deposited on the ceramic probe shaft due to the cathode sputtering in cylindrical magnetron discharge. The decrease of $I_{es}$ observed in figure 4.5 at low heating current is small and corresponds therefore to relatively clean surface of the probe shaft at the beginning of measurements. It is right, since the probes were inside of vacuum ports during discharge stabilization (approx. half of an hour) minimizing the metal deposition this way.

Other processes influencing collected electron saturation current $I_{es}$ can appear after onset of the electron emission: First suggested process is reduction of the sheath thickness due to space charge of emitted electrons around the probe. The space charge causes faster fall of the highly positive probe potential to the plasma potential. Reduction of the sheath thickness (i.e. reducing of the effective collecting area in case of cylindric probes) would reduce collected $I_{es}$. On the other hand, steeper potential fall in the sheath with reduced thickness can also cause increase of $I_{es}$ due to additional ionization in the sheath around the probe. This process becomes significant if the emissive probes are used in high pressure plasma as was shown in [Yan *et al.* (1996)]. Another possible process that commences with onset of emission is interaction of the space charge of emitted electrons with space charge around the probe shaft. Finally, the plasma can be locally disturbed in vicinity of the strongly emitting probe and that can be the reason of increase of electron saturation current at high probe heating. Disturbance of the plasma by electron emission from the probe was probably more pronounced in case of DP-machine, where the plasma density is lower than in the cylindrical magnetron case. If the local disturbance of plasma really increases the electron saturation current, it can be possible explanation of the electron saturation current increase, that was more pronounced in DP-machine data as was shown e.g. in figure 4.8, where the increase of electron saturation current was dominant at increasing probe heating.

### 5.1.3 Magnitude of changes

The magnitude of the electron saturation current variations varied with the probe length as well as with the probe material as it was shown in Chapter 4.2. The variations were more pronounced in case of shorter probes as it can be seen in figures 4.10, 4.11 and 4.14. This was probably because the shorter probes were more affected by above described non-reversible temperature induced changes, since the heat transport into the plasma was worse in their case and the probe shaft together with electrical junctions were therefore more exposed to the high temperature. In some extreme cases the copper feed line even melted at the connection with the probe wire in the ceramic double bored probe shaft. Another probe construction would be therefore suitable in these cases.

The variations were systematically less pronounced in case of W(0.6 % Th) probes than in case of probes made from pure tungsten as it was shown in figure 4.12. It was probably connected with the lower work function of the thoriated wire that enabled operating of probes at lower temperature of the wire to keep sufficient emission. At lower temperature the dominant temperature induced non-reversible changes of probe parameters were reduced.

Similar explanation can be given also for the probes made from thinner wire (W, $d \doteq 0.09$ mm). In that case the magnitude of electron saturation current variations was considerably lower than for W, $d = 0.15$ mm probes as it was shown in figure 4.13. The reason for that can be found in smaller thermal conductivity of the thinner wire. The thinner probes were therefore less affected by temperature induced non-reversible changes that were – as mentioned above – the most expressive in presented measurements. The thinner probes were less affected by temperature induced non-reversible changes thanks to their smaller thermal conductivity even if the temperature of the probe tip had to be slightly higher because of smaller emitting probe tip surface.

## 5.2 Overestimating of the plasma potential by the strongly emitting probe

[Takamura *et al.* (2004)] showed that if the temperature of emitted electrons is sufficiently large in comparison to the the temperature of plasma electrons, the plasma potential determined by the strongly emitting probe can be more positive than the real plasma potential; as it was observed experimentally in the cylindrical magnetron plasma as well as in the DP-machine plasma. Their analytical model exhibits overestimation by less than $kT_e/e$ for the plasma facing material LaB$_6$ with $A_{RD} = 2.9 \times 10^5$ Am$^{-2}$K$^{-2}$, $\chi = 2.7$ eV at maximal considered temperature ratio $T_e/T_{eW} = 10$ as was shown in above mentioned article. $T_{eW}$ is temperature of thermionic emitted electrons, which are assumed to be emitted with Maxwell-Boltzmann distribution.

The model developed in [Takamura *et al.* (2004)] is described in Appendix A and is applied to the floating probe condition and discharge conditions typical for the cylindrical magnetron plasma there. The resulting overestimation of the plasma potential obtained in the model in case of cylindrical magnetron plasma with $T_e = 0.5$ eV, $T_i = 300$ K, $n = 4 \times 10^{16}$ m$^{-3}$ and the case of tungsten probe is given figure A.3, where are also given data for $T_e = 10$ eV. The model was created for the case of space charge limited emission and therefore the data depicted in figure A.3 correspond to the space charge limited region marked in figure 2.6.

Probe wire temperature was not measured in experiment presented in this work, however it can be estimated. Considering relatively huge temperature limited emission current from the probe $I_{em} = 50$ mA as an upper limit, emitting area $S = 1$ mm$^2$, work function of tungsten $\chi = 4.5$ eV and Richardson constant $A_{RD} = 70 \times 10^4$ Am$^{-2}$K$^{-2}$, the probe wire temperature computed from equation 2.7 is $T_W = 2820$ K[1], what is $T_W = 0.24$ eV. However, even at highest reachable probe wire temperature (melting point of tungsten), overestimation of the plasma potential by the strongly emitting probe computed using the model was approximatively by 6 $kT_e/e$. That corresponds to overestimating by 3 V at

---

[1] The melting temperature of tungsten is $T = 3695$ K

$T_e = 0.5$ eV as can be seen in figure A.3. It is less than was obtained in presented experimental data given in Tables 4.2 and 4.3, where the overestimation was in average by 5.13 V for W, $d = 0.14$ mm probes and even by 6.8 V in the case of W, $d \doteq 0.09$ mm probes. The difference between experiment and model is probably caused by geometry difference since the above described theory was developed for infinitely large emitting plane metallic surface in contrast to cylindrical symmetry[1] of probes. The model therefore does not take into account the expanding sheath in front of the emitting surface at increasing probe heating and other processes connected with the cylindrical symmetry of the emitting surface. The difference between the model and presented experiment can be partially also caused by experimental error in determining of $T_e$ in argon plasma – in the argon plasma there is typically double temperature Maxwell distribution and the higher "temperature" was not taken into an account. It can be also caused by reducing of electron flow by the magnetic field in cylindrical magnetron.

As it was shown in Chapter 4.3 overestimating of the plasma potential varies with different probe material and also probe wire diameter. Substantially lower overestimation of $U_{pl}$ in case of thoriated probes than in case of tungsten probes is probably connected with lower work function of thoriated wire that enables to gain sufficient emission at lower probe temperature ($T_e/T_{eW}$ is higher). Similarly the difference in overestimation of $U_{pl}$ between W, $d = 0.14$ mm and W, $d \doteq 0.09$ mm probes is probably caused by slightly higher temperature that is needed for sustaining the same emission in case of thinner probes in contrast to thicker probes. However, its role can also play the geometry – the ratio between sheath thickness and probe wire radius.

---

[1] cylindrical in the first approximation

# Chapter 6

# Conclusions of Part I

The study of the electron saturation current variations collected by the emissive probe at varying probe heating was presented and discussed here for cases of the weakly magnetized low temperature argon plasma in the cylindrical magnetron and unmagnetized low temperature argon plasma of DP-machine. It was found that electron saturation current variations can be divided into non-reversible and into reversible changes. The non-reversible variations were dominant and were connected with change of the emissive probe properties. Reversible variations – variations connected with thermionic emission from the probe – were less pronounced. Possible processes responsible for variations were discussed here.

It was found, that variations were more pronounced in case of the shorter probes and for those with higher work function. The variations were less pronounced in case of thinner probes. It was conclude, that it was due to the temperature induced non-reversible changes since the heat transport to the ceramic probe shaft was higher in all described cases with more pronounced electron saturation current variations.

In the second part overestimation of the plasma potential by the strongly emitting probe in the low temperature plasma was studied and compared with analytical model. It was shown, that experimental data overestimate the plasma potential somewhat more than was the model prediction.

# Part II

# PIC-MCC Model of the DC Discharge in the Cylindrical Magnetron

# Chapter 7

# Theory

As mentioned in Chapter 1, this part of the thesis is focused on creation of the two dimensional numerical model of a dc discharge in the cylindrical magnetron system. Relatively thorough experimental data set is available for comparison with the numerical model, that gives good measure of reliability of obtained numerical results.

## 7.1 Modeling approaches

Various approaches were formerly developed for numerical modeling of the plasma. They can be divided into three basic groups:

1. kinetic codes
2. magnetohydrodynamic codes
3. hybrid codes

In the first – kinetic – approach the plasma is assumed as an group of particles and plasma parameters are obtained by statistical methods. Kinetic codes focus a) on solving of the Boltzmann kinetic equation:

$$\frac{\partial f_\nu(\vec{r},\vec{c},t)}{\partial t} + \vec{c}\frac{\partial f_\nu(\vec{r},\vec{c},t)}{\partial \vec{r}} + \frac{\vec{F}}{m_\nu}\frac{\partial f_\nu(\vec{r},\vec{c},t)}{\partial \vec{c}} = \frac{\delta f_\nu(\vec{r},\vec{c},t)}{\delta t} \tag{7.1}$$

for the charged particles distribution function $f$, where $\nu$ denotes charged particles species, $\vec{r}$ is position , $\vec{c}$ is total velocity ($\vec{c} = \vec{u} + \vec{v}$, where $\vec{u}$ is drift velocity and

$\vec{v}$ is chaotic velocity), $t$ is time, $\vec{F}$ are external forces acting in the plasma, $m$ is mass of charged particle and $\frac{\delta f_\nu(\vec{r},\vec{c},t)}{\delta t}$ is so called "collision term" that assesses the effect of collisions on charged particles distribution function, or b) on particle simulation of plasma that is object of interest of this work.

In the second – magnetohydrodynamic – approach the plasma is assumed to be mixture of two or more fluids. Magnetohydrodynamic codes are based on solving of equation:

$$nm\frac{\partial \vec{u}}{\partial t} = \vec{c} \times \vec{B} - \nabla p, \tag{7.2}$$

that can be obtained by integration over velocity space from Eq. 7.1 and at employing some approximations. $p$ in Eq. 7.2 is pressure of the fluid representing the plasma. Eq. 7.2 in combination with continuity equation, generalized Ohm's law, Maxwell equation and the state equation describe plasma in magnetohydrodynamic approach. Since the magnetohydrodynamic codes are not the topic of interest of this work, I redirect interested readers for their detailed description given elsewhere (e.g. [Kracík & Tobiáš (1966)]).

The third – hybrid – approach combines advantages of both approaches. E.g., kinetic description is employed on energetic electrons and magnetohydrodynamic approximation on ions and optionally also low-energetic electrons.

Magnetohydrodynamic description is suitable for dense plasma, kinetic description is suitable for weaker plasma.

## 7.2 Particle In Cell method

One of the frequently used particle simulation techniques describing plasma kinetically is Particle-In-Cell (PIC) technique. In this technique simulation region is divided into cells. The Poisson equation:

$$\triangle\varphi = -\frac{\rho}{\varepsilon_0}, \tag{7.3}$$

where $\varphi$ is potential, $\rho$ is charge density and $\varepsilon_0$ is dielectric constant, is solved on grid points in order to obtain electric field acting in the plasma. This is done instead of computing electric force acting on each charged particle independently from:

$$\vec{F}_i = \frac{q_i}{4\pi\varepsilon_0} \sum_{j=1, j\neq i}^{N} \frac{q_j}{r_{ij}^2} \frac{\vec{r}_{ij}}{r_{ij}}, \tag{7.4}$$

where $\vec{F}_i$ is electric force acting on particle $i$, $q_i$ is its charge, $q_j$ is charge of particle $j$, $r_{ij}$ is distance between particles $i$ and $j$ and $N$ is total number of charged particles in the system.

The fields and energy are obtained independently from first principles of PIC and no assumption is needed to be made about the fields or the energy and velocity distributions.

The flow chart of the Particle-In-Cell technique with Monte-Carlo treated Collisions (PIC-MCC) is schematically depicted in figure 7.1. In each time step following operations are performed:

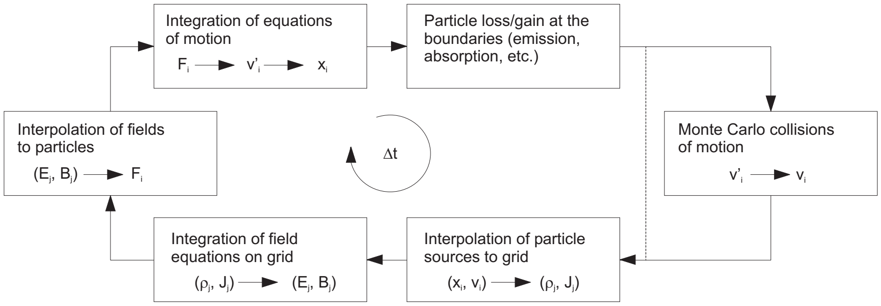

Figure 7.1: A flowing chart of PIC-MCC model. Figure is taken from [Verboncoeur (2005)].

1. The charge density $\rho(r)$ is obtained by weighting of particles to the spatial grid.

2. $\rho(\vec{r})$ is used in Poisson equation to solve for the electric field $\vec{E}(\vec{r})$.

3. $\vec{E}(\vec{r})$ is weighted back to each particle position in order to determine the force acting on each particle.

4. The Newton–Lorentz equations of motion are used to advance the particles to new positions and velocities.

5. The boundaries are checked and out-of-bounds particles are removed.
6. A Monte-Carlo collision handler checks for collisions and adjust the particle velocities accordingly. Also, in the case of ionization collisions, new electron–ion pairs are created.

Relatively thorough description of PIC-MCC technique including of various improvements in implementation is available in literature [Birdsall & Langdon (1991)] or more recently in review article [Verboncoeur (2005)], that is related closely to the PIC-MCC code used in this work. That is why I redirect the readers for more detailed description there and at this place only some basic terms used further in this work will be mentioned:

**Cloud-In-Cell technique:** Different techniques for the particle weighting to the grid can be used with different precision and computational cost. Usually Cloud-In-Cell technique is used where the particles are represented by clouds and they therefore contribute to more grid points simultaneously according to their position as it is demonstrated in figure 7.2. The charge in cloud can be distributed homogenously (as demonstrated in figure 7.2) or decrease with distance from particle – linearly or even with more sophisticated shape.

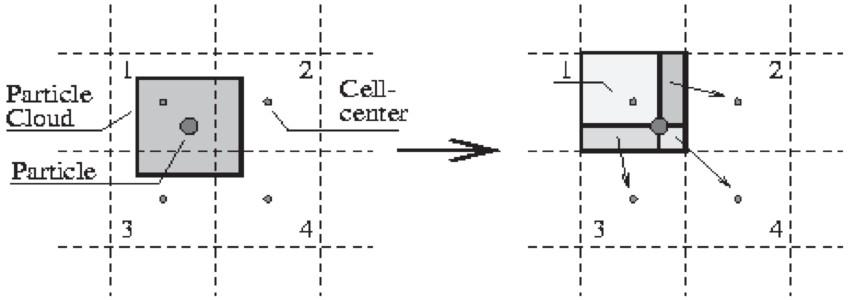

Figure 7.2: Schematics of weighting of particles by Cloud-In-Cell technique to the 2d equidistant grid.

**Leap frog scheme:** The Newton–Lorentz equations of motion used for advancing of particles:

$$m\frac{d\vec{v}}{dt} = q\left(\vec{E} + \vec{v} \times \vec{B}\right) \tag{7.5}$$

and

$$\frac{d\vec{r}}{dt} = \vec{v} \tag{7.6}$$

have to be discretized using some difference scheme. Frequently is used discretization by the second-order accurate center difference scheme called "leap frog" scheme (e.g. [Birdsall & Langdon (1991)]). In equidistant grid with constant volume of cells is expressed by:

$$\begin{aligned} \frac{\vec{v}_{(t+\triangle t/2)} - \vec{v}_{(t-\triangle t/2)}}{\triangle t} &= \frac{q}{m}\left(\vec{E}_t + \frac{\vec{v}_{(t+\triangle t/2)} - \vec{v}_{(t-\triangle t/2)}}{2} \times \vec{B}_t\right) && (7.7) \\ \frac{\vec{r}_{(t+\triangle t)} - \vec{r}_t}{\triangle t} &= \vec{v}_{(t+\triangle t/2)}. && (7.8) \end{aligned}$$

**DADI technique:** DADI is Dynamic Alternate-Direct-Implicit method of solving the Poisson equation. In more detail it is described e.g. in [Hewett *et al.* (1992)].

**Null Collision technique:** Collisions are treated in PIC-MCC model by Monte Carlo technique. The collision probability for the $i$-th particle is calculated, based on the distance $\triangle s_i = v_i \triangle t$ travelled in each time-step $\triangle t$:

$$P_i = 1 - \exp\left(-\triangle s_i \sigma_T(\epsilon_i) n_t(\vec{r}_i)\right) = 1 - \exp\left(-v_i \triangle t \sigma_T(\epsilon_i) n_t(\vec{r}_i)\right), \tag{7.9}$$

where $\sigma_T$ is total collision cross section ($\sigma_T(\epsilon_i) = \sigma_1(\epsilon_i) + \cdots + \sigma_N(\epsilon_i)$ for $N$ types of collisions), $\epsilon_i$ is kinetic energy of $i$-th particle and $n_t(\vec{r}_i)$ is local density of target species at the position of $i$-th particle. In Null Collision technique a virtual "Null Collision" is added into Monte Carlo model that ensures that $v_i(\sigma_T(\epsilon_i) + \sigma_{null}(\epsilon_i))$ is constant over whole velocity space. A collision occurs if a uniformly distributed random number on the interval $[0, 1]$ is less than $P_i$. Advantage of the Null Collision technique is that $\sigma_j(\epsilon_i)$ can be computed only if random number is less than $P_i$. The type of collision is chosen by next uniformly distributed random number. Null collision means no collision. Details are given in [Vahedi & Surendra (1995)].

**Superparticles:** Charged particles in plasma are usually replaced by superparticles in PIC model. Each superparticle represents e.g. $10^3$–$10^6$ real particles. The total charge and mass are conserved.

### 7.2.1 Conditions of stability

According to [Birdsall & Langdon (1991)] following conditions should be fulfilled in order to obtain numerically stable and reliable results via PIC-MCC technique:

1. Particles should not pass the distance longer than one cell per time-step: $v\triangle t/L_c < 1$, where $v$ is characteristic velocity (thermal velocity $v_{th}$ is usually taken in plasma with Maxwell-Boltzmann distribution) and $L_c$ is characteristic length of cell.

2. The time-step in simulation has to resolve the plasma frequency – according to [Kawamura *et al.* (2000)] the stability criterion for the standard explicit leap frog mover is $\omega_{el}\triangle t \leq 2$, the accuracy condition for leap frog mover is $\omega_{el}\triangle t \lll 1$. Usually $\omega_{el}\triangle t \lesssim 0.2$ is used. (In presence of magnetic field also electron cyclotron frequency has to be resolved: $\omega_c\triangle t \lll 1$.)

3. The grid should resolve the Debye length in order to proper resolve electric field: $L_c/\lambda_D < 1$. Coloumbic interactions between particles are neglected in scales smaller than one cell.

4. Number of computational particles in cell should be much bigger than one in order to reduce numerical noise: $N_c \ggg 1$. The numerical noise decreases as $N_c^{-1/2}$ according to [Verboncoeur (2005)]. E.g. in [Hammel & Verboncoeur (2004)] typically $N_c = 30 - 50$ was used.

If the above mentioned conditions are not fulfilled, numerical fluctuations and additional nonphysical heating of particles can occur in simulation that leads to inaccurate or even to physically incorrect solution.

### 7.2.2 Speeding up the model

The PIC-MCC method is a strong approach that enables self-consistent plasma description at broad range of plasma parameters. However, the PIC-MCC technique is relatively computationally consuming method. Big computational power is needed especially in case solving of 2d or even 3d problems. The time required for one time-step of PIC-MCC code is proportional to $T_1 \sim N \ln N$. With the increase of spatial dimensions of the model the number of computational particles in simulation quickly increases if conditions given Chapter 7.2.1 have to be fulfilled.

In order to reduce computational power a suitable computational parameters have to be set in the model in order to minimize computational time needed for obtaining stable and physically correct solution. Also further techniques are available for speeding up the computation – some of them are listed below:

- Using proper starting density profiles and energy distributions close to expected results. Starting with density profiles close to final results and corresponding velocity distribution significantly decreases required simulation time. It is caused especially by the time that is required for redistribution of cold ions to their final positions otherwise.

- Using adaptive grid – a grid that has smaller cells in region with steep change of potential and bigger cells otherwise.

- Smoothing of the computed potential profile – smoothing of the potential profile obtained by solving of Poisson equation reduces the numerical noise in the model and allows therefore decrease of number of simulating particles in the model.

- Subcycling of ions. Since ions are much heavier than electrons they move slower and longer time-step can be therefore used for them. Ions are moved every $k$-th step if they are subcycled (with $\triangle t_i = k \triangle t_e$). Maximal achievable gain of this technique is 2 in case of electropositive discharges, where the number of electrons and ions is comparable. In the case of electronegative discharges the speeding up of simulation is higher.

- Light ions – the simulation can be accelerated by using ions with lower mass in initial part of simulation, that enables them faster redistribution close to their final positions. After this initial phase, the mass has to be set to the real value and also their velocity should be corrected by factor $(m_i/m_{i-light})^{1/2}$ to conserve their kinetic energy. At assumption that ions reach their final positions quickly after correcting their mass, the maximal achievable gain of this technique is $(m_i/m_{i-light})^{1/2}$.

- In case of radio-frequency (rf) discharges the direct implicit particle advance can be used [Kawamura *et al.* (2000)] instead of explicit scheme used otherwise. The implicit movers are stable over a wider range of time-steps and gird spacings than explicit movers. Furthermore direct implicit particle simulation relaxes the $\omega_{el}\triangle t$ time stability constraint and the $L_c/\lambda_D < 1$ accuracy constraint that way that $\triangle t$ must resolve only rf drive frequency $\omega_0$ and $L_c$ must resolve the time averaged sheath size $s$ at the boundary. In a driven rf discharges the $s \gg \lambda_D$. This way of speeding up the simulation is helpful if the fast phenomena are not objects of interest.

- Using longer time-step in combination with checking of the distance travelled by particles. Particles should not pass the distance longer than one cell per time-step in PIC-MCC simulation (see Chapter 7.2.1). Simulation can be speeded up using longer time-step in combination with checking of the distance travelled by particles. If some particle pass a distance longer than the width of cell during the time-step, the particle was returned to its initial position in phase space and it was accelerated over two half-time-steps. This technique was used e.g. in [van der Straaten *et al.* (1998)].

- Finally the most powerful approach for shrinking the time needed for the PIC-MCC simulation is using parallel PIC-MCC scheme and solving the problem on multiprocessor supercomputers. This approach enables to solve large and computationally consuming problems that would not be possible to solve on single-processor machine or that would spent years of computational time. Parallel processing is already widely developed. An introduction in parallel processing is given e.g. in [Alaghband (1997)]. An example of parallel implementation of PIC code is published e.g. in [Wang *et al.* (1995)].

## 7.3 Glow discharge structure

The aim of this part of work was to create numerical model of a low temperature weakly magnetized dc glow discharge in the cylindrical magnetron device. Short description of the glow discharge is therefore given here.

Structure of a dc glow discharge is schematically depicted in figure 7.3. Bright and dark regions are usually visible in a glow discharge. Bright regions correspond to regions with higher excitation collision frequencies and subsequent photon emission. Names of bright and dark regions in a glow discharge are given in figure 7.3.

The discharge can be divided into three regions according to distribution of electric field in discharge: cathode layer – region with large space charge and big electric field, region of the Faraday dark space and positive column – region with very weak electric field and anode regions with small potential fall close to anode.

Electrons are emitted from cathode with low energy – usually less than 1 eV. They are emitted due to secondary emission caused by impinging ions that were accelerated in potential fall in the vicinity of cathode (cathode fall). The emitted electrons do not have sufficient energy for exciting of atoms close to the cathode which results in formation of Aston dark space. The electric field in cathode layer accelerates these electrons to an energy sufficient for excitation and the cathode glow appears. Two or three layers of cathode glow may be formed according to [Raizer (1991)] – it corresponds to the excitation of different atomic levels. The energy of accelerated electrons then grows above the maximum of excitation cross section. Electrons cease to excite atoms and cathode dark space is formed. This is the region where ionization of atoms predominantly takes place and most electrons are multiplied there. The newborn ions move much slower than electrons and a large positive space charge builds up. The current is transferred mostly by ions in this region. By the end of cathode layer the electron flux gets fairly large as a results of the avalanche process of multiplication. Most electrons are generated at very end of layer. They continue in weak electric field with energies corresponding approximately to the maximum of the excitation cross section. As a result the negative glow appears. Electrons loose their energy in region of negative glow by excitation collisions and they don't gain new sufficient energy in the weak electric field. That forms Faraday dark space. Most, but not all of the electrons in the negative glow region have moderate energies. Some of them are energetic ones that were liberated from deep inside of cathode layer or at the cathode, having traversed the cathode layer with only a few inelastic collisions. They ionize atoms. As a result the electron density immediately after the cathode layer is higher than in the positive column. In the Faraday dark space the longitudinal electric field increases to the value characterizing the positive column. The electrons in the positive column have random velocity distribution typical of non-equilibrium weakly ionized plasma with slight asymmetry introduced by the drift towards the anode. The average electron energy is typically 1–2 eV. Energetic electrons from the tail of energy distribution undergo excitation collisions, that generate the light emission in the positive column. The anode repels ions but pulls out electrons from the positive column. Thus a region of negative space charge is formed in vicinity of anode. Its higher field accelerates electrons. The result is the anode glow.

### 7.3.1 Cathode fall

The regions of the cathode glow and cathode dark space may be approximated as a matrix sheath (assumption of electron depleted sheath with uniform ion density $n_i$) with a linearly decreasing electric field [Lieberman & Lichtenberg (1994)]:

$$E(x \leq d) \approx E_0 \left(1 - \frac{x}{d}\right), \tag{7.10}$$

where $d$ is the length of the cathode sheath and $E_0$ is the x-directed electric field strength at the cathode. According to figure 7.3, the cathode position is at $x = 0$. Note that it is assumed that the field is not a function of $r$ in this region. The cathode fall voltage $U_c$ and the sheath ion density are related to $E_0$ by Poisson equation:

$$n_i = -\frac{\varepsilon_0}{e}\frac{dE_x}{dx} = \frac{\varepsilon_0 E_0}{ed} = \frac{\varepsilon_0 U_c}{ed^2}, \tag{7.11}$$

where

$$U_c = E_0 \int_0^d \left(1 - \frac{x}{d}\right) dx = \frac{E_0 d}{2}. \tag{7.12}$$

At the cathode, the current density may be determined assuming a collisional matrix sheath. The ion current density $j_i$ is then:

$$j_i(x) = e\mu_i(E)n_iE(x), \tag{7.13}$$

where $\mu_i$ is mobility of ions. At the cathode, the ion current density is:

$$j_i(0) = \frac{\varepsilon_0\mu_i E_0^2}{d} = \frac{4\varepsilon_0\mu_i U_c^2}{d^3}. \tag{7.14}$$

The total current density at the cathode is the sum of electron and ion current densities:

$$j(0) = \frac{4\varepsilon_0\mu_i U_c^2\left(1+\gamma_{se}\right)}{d^3}, \tag{7.15}$$

where $\gamma_{se}$ is coefficient of the secondary emission at the cathode. Using assumption that current density is constant over whole cathode surface, Eq 7.15 can be rewritten for the total current as:

$$I = \frac{4\pi R^2\varepsilon_0\mu_i U_c^2\left(1+\gamma_{se}\right)}{d^3}, \tag{7.16}$$

where $\pi R^2$ is surface of the disc shaped cathode.

### 7.3.2 Self-sustaining of the discharge

A sufficient number of electrons has to be created by ionization in the discharge region (cathode layer) to compensate loss of particles on electrodes in case of self-sustained discharge. In the steady state case and if the diffusion can be neglected in lateral directions the increase of the current density due to ionization collisions is described by:

$$\frac{dj_e}{dx} = \alpha j_e, \tag{7.17}$$

$$\frac{dj_i}{dx} = -\alpha j_e, \tag{7.18}$$

where $\alpha = \alpha(E)$ is ionization coefficient. The total current density, that is constant along the whole discharge region, is given by:

$$j_e + j_i = j = const \tag{7.19}$$

Since the current density of secondary electrons emitted from cathode by the impinging of accelerated ions is described by:

$$j_e(0) = \gamma_{se} j_i(0) = \frac{\gamma_{se}}{1+\gamma_{se}} j, \tag{7.20}$$

the condition that has to be fulfilled for self-sustaining the discharge can be derived from Eq. 7.17, 7.18 and 7.20 as:

$$\int_0^d \alpha(E(x))dx = ln(1 + \frac{1}{\gamma_{se}}). \tag{7.21}$$

Ionization coefficient $\alpha$ is a known function of electric field strength that can be expressed by:

$$\frac{\alpha}{p} = A \exp\left(-\frac{Bp}{E(x)}\right), \tag{7.22}$$

where $A$ and $B$ are roughly constant and are available in tables and $p$ is working gas pressure. In the case of argon $A = 13.6$ cm.Torr$^{-1}$ and $B = 235$ V.cm$^{-1}$.Torr$^{-1}$ for $E/p = 100$–$600$ V.cm$^{-1}$.Torr$^{-1}$.

Using matrix sheath approximation (Eq. 7.10), the condition for self-sustaining the discharge (Eq. 7.21) can be rewritten as:

$$\frac{AB(pd)^2}{2U_c} S\left(\frac{2U_c}{Bpd}\right) = \ln\left(1 + \frac{1}{\gamma_{se}}\right), \tag{7.23}$$

where

$$S(x) = \int_0^x \exp(-\frac{1}{y})dy, \tag{7.24}$$

what is Paschen law for a matrix sheath, where $U_c$ is breakdown voltage. It gives breakdown condition in terms of $U_c$ and the product of $pd$.

In case of magnetized dc discharge lower voltage is needed for sustaining the discharge at intermediate pressures since energetic electrons that are moving on helical curves according to Lorenz force:

$$\vec{F} = q(\vec{E} + \vec{v} \times \vec{B}) \tag{7.25}$$

remain longer in active discharge area in case of proper configuration of magnetic field and probability of ionization collision therefore increases.

### 7.3.3 DC discharge regimes

A typical current–voltage characteristic for dc non-magnetized discharges is schematically shown in figure 7.4. As current is increased, a dark discharge transitions to a self-sustained discharge as the breakdown potential $U_c$ is reached. The discharge is sustained by current flowing through a spot on the cathode. As current is increased, the spot size grows until the whole cathode is covered and the discharge voltage remains approximately constant. This is the normal glow discharge. As current is further increased after current flows through the entire cathode surface, the voltage increases in the abnormal glow regime. If current is further increased, the glow discharge will change to an arc discharge characterized by high current and low voltage. The transition to arc discharge is caused by strong heating of cathode which than emits electrons by thermionic emission.

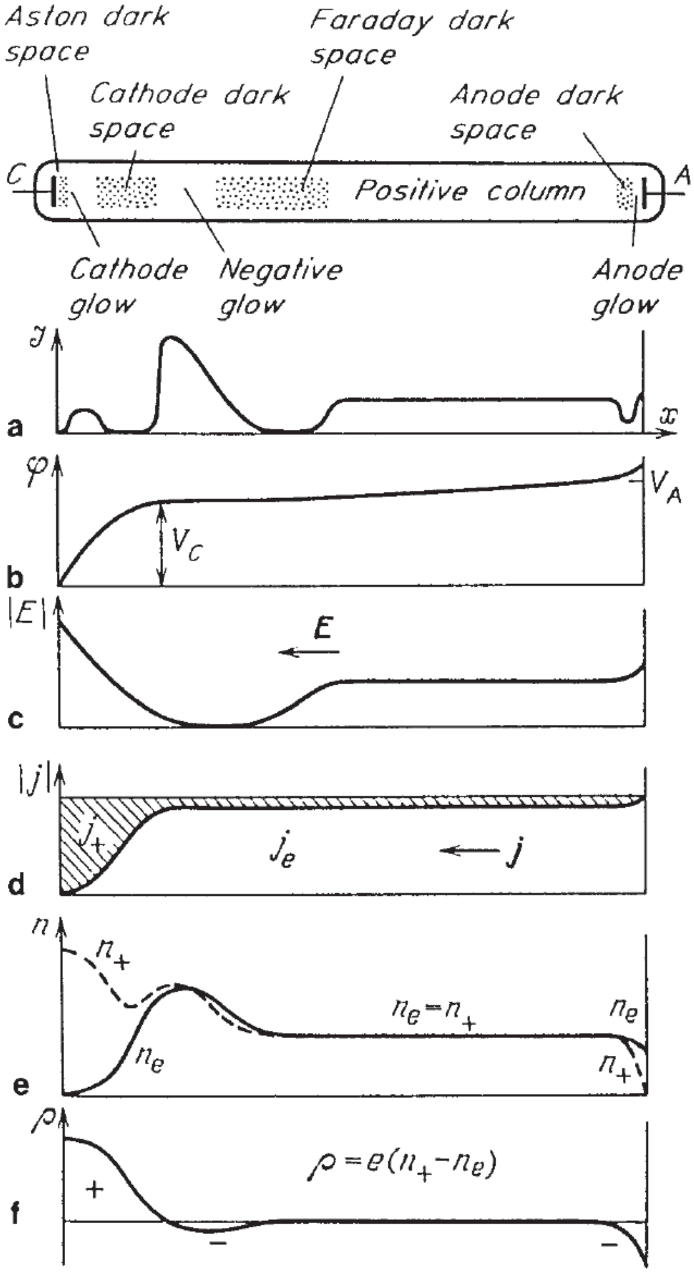

Figure 7.3: Regions of a dc glow discharge in a tube and the distribution of: (a) light intensity, (b) potential, (c) longitudinal electric field, (d) electron and ion current density, (e) charged particles densities and (f) space charge. Figure was taken from [Raizer (1991)].

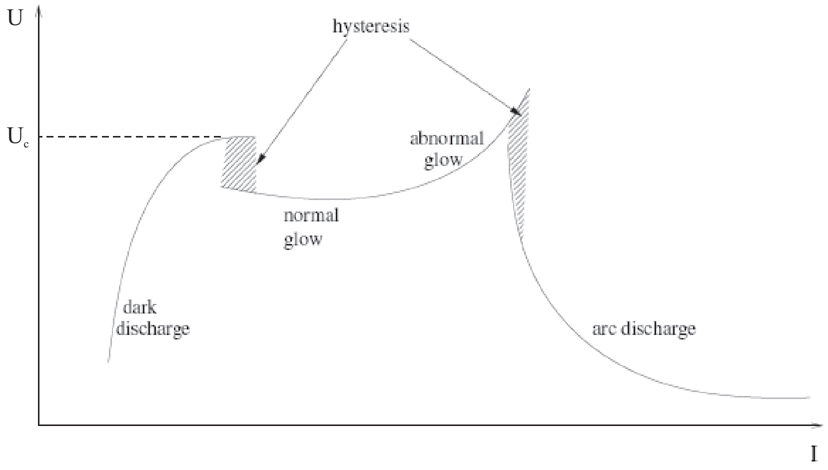

Figure 7.4: Current–voltage characteristic of DC discharges.

# Chapter 8

# Model description

## 8.1 Cylindrical magnetron

Scheme of the cylindrical magnetron device, that is described by the model, is depicted in figure 8.1. Detailed description of this device is given e.g. in [Passoth *et al.* (1997)]. It is similar to that described in previous part of the thesis in Chapter 3.1 and differs substantially only in length of the discharge area and in electrodes radii. The grounded anode has 60 mm in diameter, the coaxially positioned water cooled cathode has diameter of 10 mm. Discharge area is limited to the length of 120 mm by a pair of metallic limiters that are connected to the cathode potential. The discharge vessel is made from nonmagnetic stainless steel. Some experiments presented here were done with aluminium anode, but it had practically no influence on the discharge parameters since the secondary emission from anode is small and it is not so important for sustaining the discharge. The plasma in the cylindrical magnetron is confined by homogenous magnetic field parallel to axis. It is created by couple of magnetic coils and can vary up to 40 mT. The system is evacuated by turbomolecular vacuum pump backed by oil free piston vacuum pump. The ultimate pressure in this system is in order of $10^{-3}$ Pa. Discharge in the magnetron is usually produced in noble gases at pressures 1–10 Pa. The pressure of the working gas in the system is regulated by MKS flow meter. Typical total discharge current of dc discharge in this device is in the range of 50–250 mA.

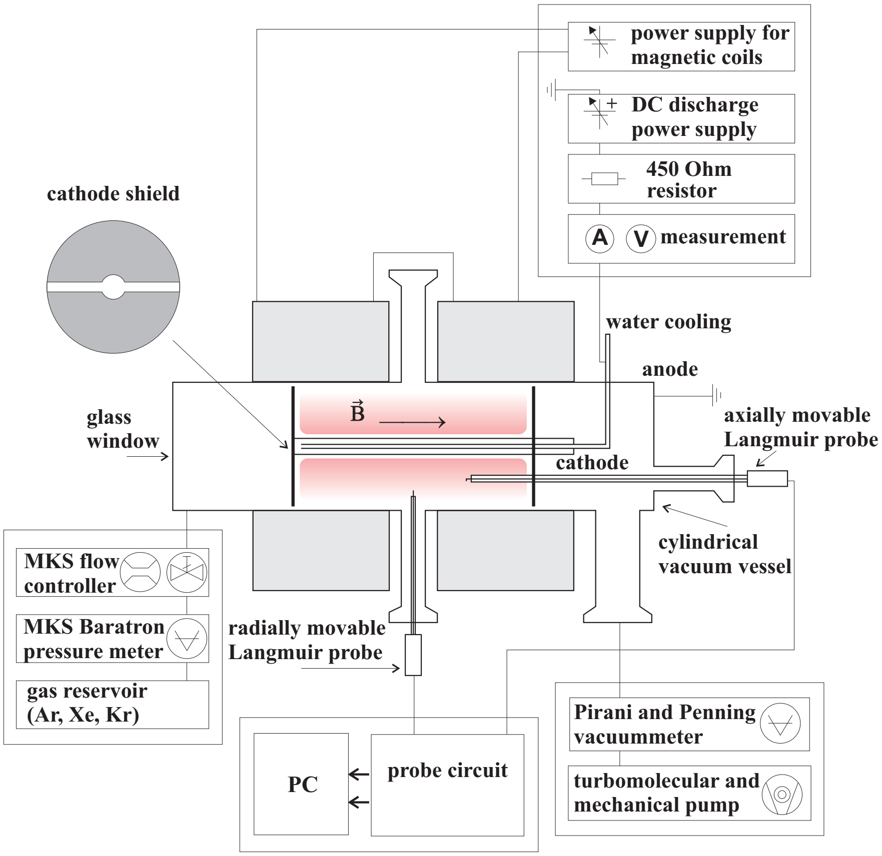

Figure 8.1: Scheme of the cylindrical magnetron; Department of Surface and Plasma Science, Charles University in Prague.

Plasma parameters were determined by means of electrical probes placed in the vacuum port in the central plane of the magnetron and in the vacuum port situated on one end of the magnetron. Schematics of the used Langmuir and emissive probes are given in figure 8.2 and in figure 8.3 respectively.

Langmuir probe shaft was composed from two Degusit® ceramic tubes. The thinner one was inserted into the thicker one in order to avoid electrical contact between the probe wire and the probe shaft that can be covered by material sputtered from cathode that deposits all around when the discharge in magnetron is burning. The Langmuir probe was constructed from the tungsten wire formed into the right-angle and aligned tangentially at the end of ceramic tube as shown in figure 8.2. This construction provides good radial resolution of the probe. The

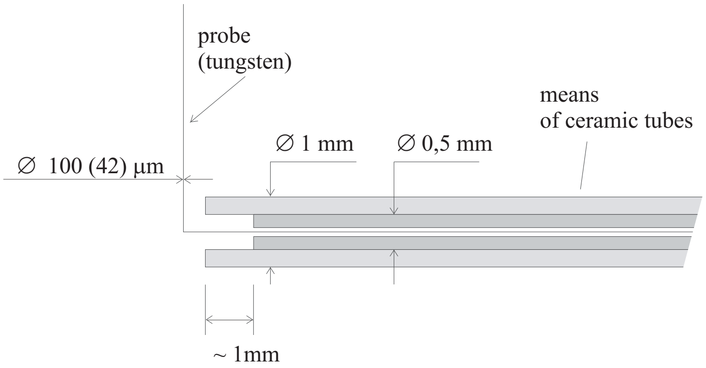

Figure 8.2: Scheme of the Langmuir probe.

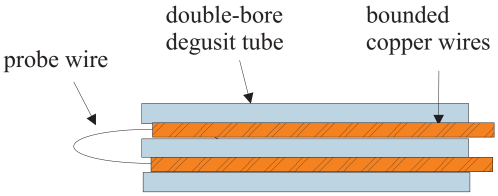

Figure 8.3: Scheme of the emissive probe.

probe wire was set perpendicularly to the magnetic field during experiments in order to minimize the effect of magnetic field to the Langmuir probe current.

The emissive probe construction was described in detail in Chapter 3.3. Emissive probe loop was also set perpendicularly to the magnetic field minimizing its effect this way.

Typical electron densities achieved in the cylindrical magnetron are of the order of $10^{16}$ m$^{-3}$. An example of the radial electron density profile as determined by the Langmuir probe is depicted in figure 8.4.  he mean electron energy is a few electronvolts in the entire discharge region as can be seen in the figure 8.5. The energy distribution function is not purely Maxwell-Boltzmann in the cylindrical magnetron argon plasma and can be characterized as bimaxwellian at some discharge conditions. However, for the purpose of the comparison with model can be assumed as Maxwell-Boltzmann in the first approximation. The detailed experimental study of plasma parameters in described magnetron is given for various discharge conditions in [Bilyk (2005)].

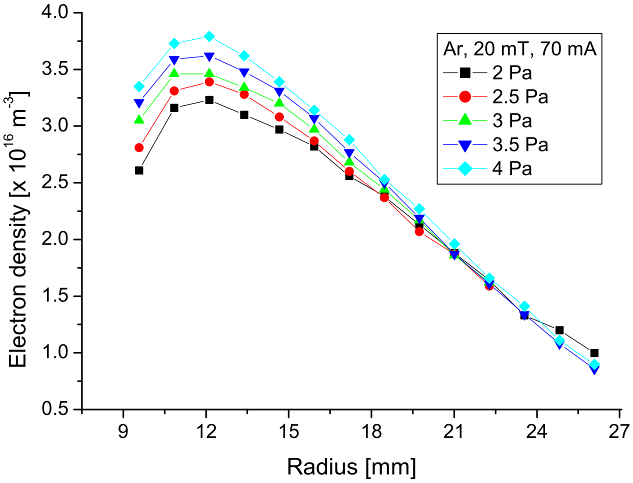

Figure 8.4: Radial profiles of the electron density in the cylindrical magnetron at magnetic field $B = 20$ mT, discharge current $I = 70$ mA and for different pressures.

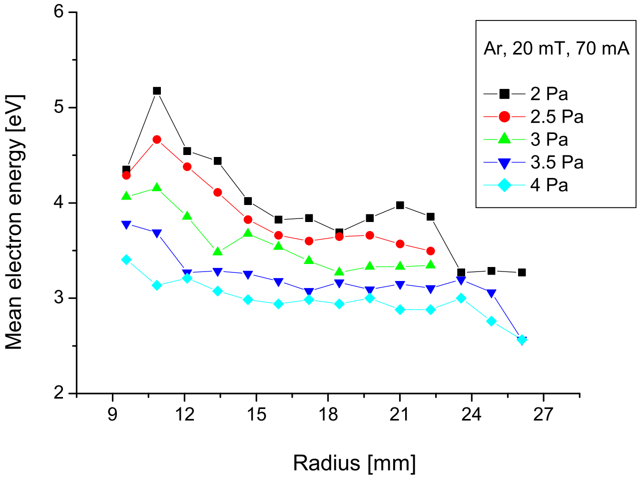

Figure 8.5: Mean energy of electrons in argon discharge at different pressures. Discharge conditions correspond to figure 8.4.

## 8.2 2D PIC-MCC model of discharge in magnetron

For simulations of the dc discharge in the cylindrical magnetron the two dimensional Object Oriented Particle-In-Cell code (OOPIC) developed at the University of California, Berkely, USA [Verboncoeur *et al.* (1995)] was chosen. It is 2d3v electromagnetic code – two dimensional in space, three dimensional in velocities.

Two dimensional model is a successor of 1D PIC-MCC model of the discharge. 1D simulations using XPDC1 code [Verboncoeur *et al.* (1993)] was done in our group earlier [Kudrna *et al.* (2002); Rusz (2003)] as a first approach to the problem. However, the ability of 1d model to describe the discharge properly was limited, because the discharge is not homogeneously distributed along the discharge region [e.g. Holík *et al.* (2004)].

Scheme of the computational region used for the 2D PIC-MCC model of the discharge is depicted in figure 8.6. Dimensions used in the model are identical with those in real device (i.e. anode diameter: 60 mm, cathode diameter: 10 mm, discharge area length: 120 mm). In order to reduce computational consumption

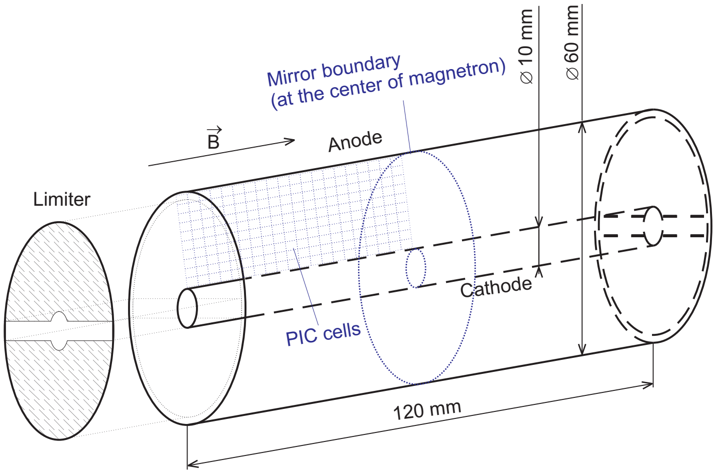

Figure 8.6: Scheme of the discharge region in the cylindrical magnetron. PIC grid including the mirror boundary placed in the middle of magnetron is marked in blue.

of the simulation the mirror boundary in the central plane of the magnetron was placed and only one half of the discharge area was simulated – from the center of the magnetron to the left limiter. It is possible due to the symmetry of the system.

The simulated region was covered by a grid equidistant in both – longitudinal and radial – directions. The total number of cells in grid differed according to the realized simulation and it will be given directly with results. Weighting of particles to the grid points is in the OOPIC code realized by Cloud-In-Cell method[1]. The electrostatic computational scheme was used, because the magnetic field induced by moving charged particles can be neglected in comparison with the applied external magnetic field in studied case ( the total discharge current in described magnetron is typically only 50–250 mA). Poisson equation at the grid points was solved by DADI technique in the model. The plasma potential profile obtained from Poisson equation was in some cases smoothed in order to reduce numerical noise in simulation. The OOPIC code was modestly optimized for our arrangement (e.g. optimization of $\overrightarrow{v} \times \overrightarrow{B}$ for $\overrightarrow{B} = (0, 0, B_z)$).

Collisions of charged particles with neutral gas were solved by the Monte Carlo method employing Null Collision technique. Following interactions were considered in the model: elastic collisions, excitation and ionization for electrons and elastic collisions and charge exchange interaction for single charged argon ions. Cross sections for elastic and excitation collisions in argon are taken from [Surendra *et al.* (1990)], ionization collision cross section is taken from [Rapp & Englander-Golden (1965)]. The collision model used in the OOPIC code is described in detail in [Vahedi & Surendra (1995)].

Coefficient of the secondary emission of electrons from stainless steel electrodes induced by impinging single charged ions was set for the major part of simulations to the value 0.2. The secondary electron yield of the PTFE fitting isolating the limiter that is held on the cathode potential from the grounded anode was set to 0.3.

The Debye length in the cylindrical magnetron is approximatively $D_\lambda \simeq 50\ \mu\mathrm{m}$ at typical discharge conditions of $T_e \approx 2$ eV and $n_e \approx 4 \times 10^{16}\ \mathrm{m}^{-3}$ according to figures 8.4 and 8.5. The Debye length should be in optimal case resolved by

---

[1] see Chapter 7.2

the grid. The plasma frequency is at these plasma conditions $\omega_{el} \simeq 11$ GHz. Gyrofrequency of electrons is in the magnetron typically lower than the plasma frequency – e.g. for the case of $B = 20$ mT it is equal to $\omega_c = 3.5$ GHz. The time step in simulation should be therefore shorter than approximatively $6 \times 10^{-10}$ s in order to resolve the response of the plasma.

The rest of used individual simulation conditions is given directly with particular simulation results.

# Chapter 9

# Results

## 9.1 Early simulation results

Moderate discharge conditions was chosen for developing the model. All simulations presented in this work were performed for the case of dc discharge in argon.

The 2D simulations were started with simulation with rough computational grid. The aim of this simulation was to obtain relatively quickly an initial profile of the plasma density for more precise simulations. This initial simulation was started with grid with only $20 \times 40$ cells – 20 in axial direction and 40 in radial. The discharge conditions were set to: $B = 20$ mT, $p = 5$ Pa, $U = -200$ V. The simulation was started with homogenously distributed charged particle density in the whole discharge region. The time step in simulation was $\triangle t = 0.5 \times 10^{-11}$ s, ions were twice subcycled and the plasma potential profile was two times binomial smoothed. Results of this preliminary simulation were presented and relatively extensively discussed in [Marek *et al.* (2004)] that is attached in Appendix D. I redirect the readers there.

Low number of cells in this simulation – that means in fact poor resolution of the potential profile – that was extreme especially in axial direction led in the end into growth of numerical instability that expressed in a nonphysical peak of density and potential growing near the limiter. This fact can be readily seen in figure 9.1 where the depicted data are taken from snapshot at $t = 8$ $\mu$s. The growing instability was connected also with the fast growth of the number of

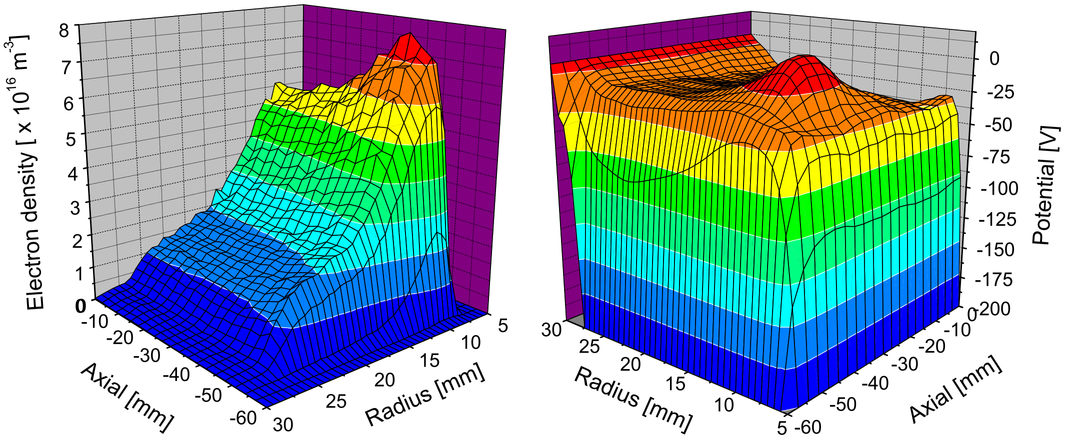

(a) (b)

Figure 9.1: Results of the simulation of the argon discharge in magnetron at $p = 5$ Pa, $B = 20$ mT, $U = 200$ V with $20 \times 40$ cells in grid taken from snapshot at $t = 8$ $\mu$s. The cathode is at radial position $r = 5$ mm, anode at $r = 30$ mm. Zero of axial coordinate denotes the center of the magnetron. The position of limiter is $z = -60$ mm; (a) electron density profile ; (b) plasma potential profile – for better view rotated by 90° in clockwise direction.

superparticles in simulation as it can be seen in figure 9.2. Although the grid used in this simulation was really very rough and the numerical instability appeared in the end, good starting profile for the next simulation was obtained.

For initialization of the next simulation there were used the results obtained at simulation time $t = 4.4$ $\mu$s, when the instability was not still too pronounced. However, small peak in density near the limiter was already present. New grid had $40 \times 100$ cells[1]. It is not still too many but the simulation was limited by computational power that was available that time. In order to fulfill condition given in Chapter 7.2.1 that the cell length should be smaller then the Debye length in order to properly resolve the sheaths we would need according to the experimental data given in Chapter 9 at least $1200 \times 500$ cells and it required

---

[1] First number denotes again the number of cells in axial direction. This notation will be used also further in this work.

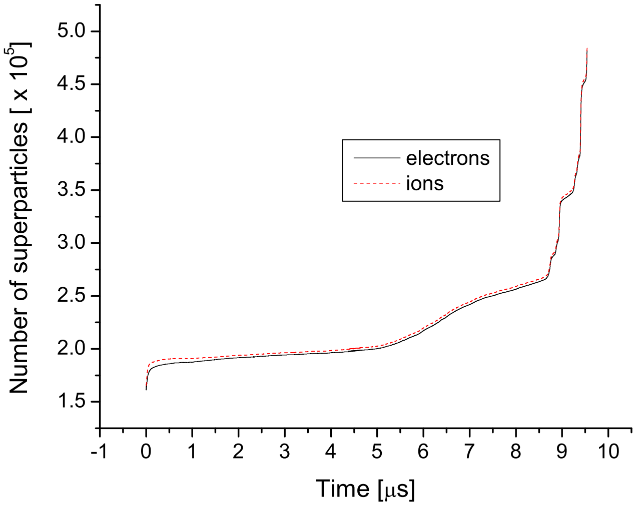

Figure 9.2: The temporal evolution of the number of superparticles in simulation with grid with 20 × 40 cells.

higher computational power than was available that time. Other parameters of the simulation with 40 × 100 cells remained the same like in previous simulation with grid with 20 × 40 cells.

This simulation was performed for time $t = 20$ $\mu$s. Resulting density and plasma potential profiles are depicted in figure 9.3. Relatively reliable results were obtained. Computed electron density profile has similar shape as was expected according to experiment. The nonphysical peak near the limiter vanished during the simulation time and also step in density observed in figure 9.1 near the radial position $r = 25$ mm disappeared and the density profile corresponds therefore better with the experimental data than the previous simulation. The only principal problem of this simulation was the steady grow of the number of superparticles in simulation – see figure 9.4. Reaching of the dynamical equilibrium of the number of simulating particles in simulation is expected in case of steady state glowing discharge. This discrepancy was broadly discussed in [Marek *et al.* (2004)] because the same behavior was observed in previous simulation. It was concluded that the increase of the number of superparticles in simulation

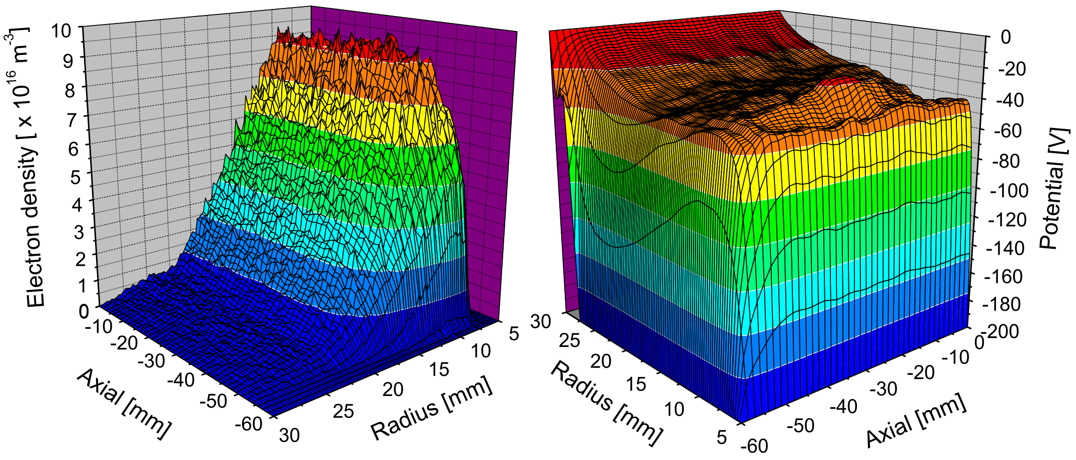

(a)

(b)

Figure 9.3: Results of the simulation of the argon discharge in magnetron at $p = 5$ Pa, $B = 20$ mT, $U = 200$ V with $40 \times 100$ cells in grid taken from snapshot at $t = 20$ $\mu$s. (a) electron density profile ; (b) plasma potential profile – for better view rotated by 90° in clockwise direction.

was probably caused by using of the voltage source instead of the current source in model although the experiment can be operated with both of them. In case of the non-magnetized discharge the situation is different and a resistance has to be used for limiting the current in case of voltage source operated discharge. That's why incorporating of the current source into the OOPIC code was managed. (The current source was already partially incorporated by J. Hammel that time, however, adaption of the code for the cylindrical magnetron geometry was needed.)

During the work on the code further simulations with the voltage source were started. At this time 4 simulations were performed concurrently – for discharge at magnetic field $B = 10$ mT, 20 mT, 30 mT and 40 mT. The grid had $400 \times 200$ cells in these simulations. It was possible to perform that because of new computing machine – computer with two Intel® Xeon$^{\mathrm{TM}}$ CPU at 3 GHz and with 4 GB of system memory. Initial density profile used for starting of these simulations

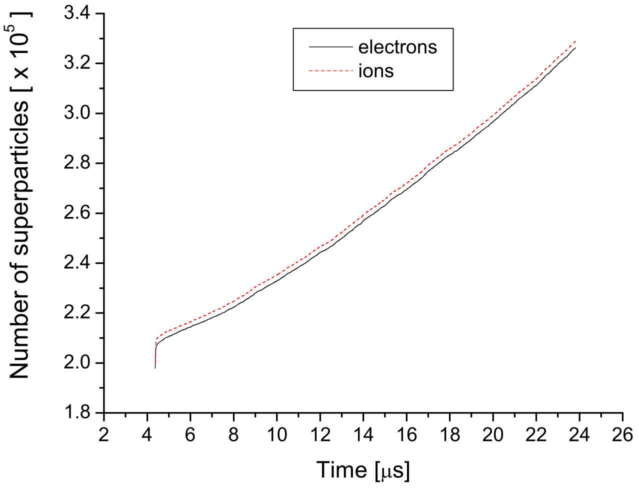

Figure 9.4: The temporal evolution of the number of superparticles in simulation with grid with 40 × 100 cells.

was taken from approximated results of the simulation with 40 × 100 cells. The discharge voltage applied in model was chosen appropriately to the experiment for each value of magnetic field in order to ensure similar discharge current and therefore similar density of charged particles in the discharge region in all cases. This scaling was needed because all simulations were started with the same initial density profile. The time step was set to $\triangle t = 10^{-11}$ s. The pressure of neutral argon gas was changed to $p = 4$ Pa because of available experimental data. The cell dimension was approximatively three times bigger than the Debye length in case of equidistant grid with 400 × 200 cells.

In figure 9.5 there are depicted temporal developments of the number of superparticles for all four simulations. Note an interesting effect of the magnetic field on the number of superparticles in simulation. While in cases of the discharge at magnetic field 10 mT and 20 mT the number of superparticles in simulation steadily grew, for cases at 30 mT and 40 mT the number of superparticles stabilized at the steady state value. These results together with the fact, that in experiment the discharge in the cylindrical magnetron can be performed also with the voltage source led into the decision to continue with simulations of discharge

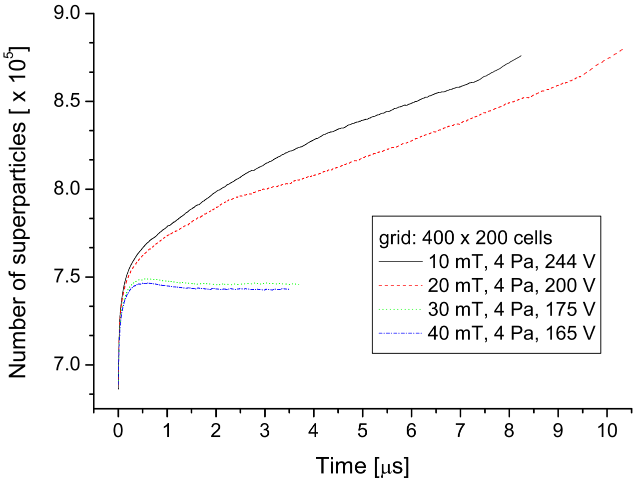

Figure 9.5: The temporal evolution of the number of superparticles in simulation with grid with 400 × 200 cells for argon discharges at different magnetic field. The applied discharge voltage was chosen appropriately to the experiment.

driven by the voltage source, although the current source was successfully adopted for our geometry and first tests of implementation were already performed.

Explanation of saturation of the number superparticles in model with 400×200 cells in case of discharges at 30 mT and 40 mT is not easy because the change of magnetic field acts together with decreasing of the discharge voltage. Lower applied voltage relaxes the constraint on timestep (the first condition in Chapter 7.2.1) since the superparticles are less accelerated in the positive column. Magnetic field prolongs the screening length for electrons in direction perpendicular to magnetic field lines and the third condition in Chapter 7.2.1 on the computational grid is easier to fulfill in this case.

Charged particles density and potential profiles obtained in simulation with 400 × 200 cells are depicted for the discharge conditions of our special interest: Ar, $p$ = 4 Pa, $B$ = 20 mT, $U$ = −200 V in figure 9.6. Although there were approximatively 10 particles per cell in this simulation the plasma potential was relatively noisy and the maximum of the electron density was more pronounced near the mirror boundary placed in the center of magnetron than was expected

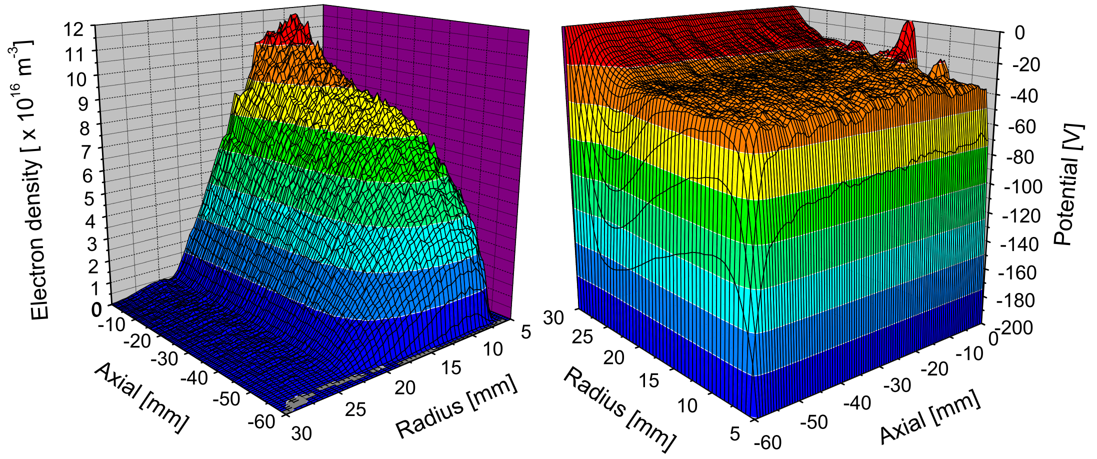

(a) (b)

Figure 9.6: Results of the simulation of the argon discharge in magnetron at $p = 4$ Pa, $B = 20$ mT, $U = 200$ V with $400 \times 200$ cells in grid taken from snapshot at $t = 10$ $\mu$s. (a) electron density profile ; (b) plasma potential profile.

according to experiment. However, results obtained at magnetic field 30 mT and 40 mT were valuable and redirected the aim towards the more time consuming simulation with more precise grid that is described in detail in the next section.

## 9.2 Recent results with the more precise grid

The simulation of the discharge in argon at $p = 4$ Pa, $B = 20$ mT, $U = 200$ V with the more precise grid was started with grid $1250 \times 500$ cells equidistant in both directions. Cell dimensions were therefore comparable with the Debye length that is according to Chapter 9 approximately $\lambda_D \approx 50$ $\mu$m at these discharge conditions. The time step was set to $\triangle t = 10^{-11}$ s – appropriately to resolve the plasma frequency that is approximatively $\omega_{el} \approx 11$ GHz and also fulfilling the condition that electrons shall not pass longer distance than one cell per time step for major part of population of electrons. The latter was generously fulfilled for electrons in the positive column with Maxwell-Boltzmann distribution with characteristic temperature $T_e < 5$ eV and it was also suitable for major part of electrons accelerated in the cathode fall region.

First results of the simulation with the grid with $1250 \times 500$ cells were presented and compared with experiment in [Marek *et al.* (2005a)] that is attached in Appendix D. More details about simulation conditions are given there. Starting density profile was taken from approximated results obtained in the simulation with the grid with $40 \times 100$ cells – see figure 9.3 (the same starting profile was used in the case of the last simulation with $400 \times 200$ cells). Presented results were taken from snapshot at simulation time $t = 6.47 \times 10^{-7}$ s. The number of superparticles in this simulation saturated and reliable results for comparison with experiment were obtained.

In this simulation there were only approximately two superparticles per cell in average. Since [Birdsall & Langdon (1991)] recommended that number of superparticles in cell should be much bigger than 1 to avoid numerical noise in simulation, obtained plasma density profiles were used for starting next simulation with more superparticles per cell.

Following simulation was started with the same grid with $1250 \times 500$ cells. The total number of superparticles was set to approximatively 7 millions for each species – electrons and ions – that gives approximatively 12 superparticles per cell in average. Each superparticle represented $5 \times 10^5$ real charged particles. Initial particle distribution in the discharge region was generated according to parameterized results of above mentioned simulation with grid with $1250 \times 500$

cells and lower number of superparticles considering Maxwell-Boltzmann velocity distribution with $T_e = 3$ eV and $T_i = 300$ K. Potential profile computed by DADI technique was four times binomial smoothed in order to further suppress the numerical noise. The time step for electrons was again $\triangle t = 10^{-11}$ s, ions were six times subcycled. Coefficient of secondary emission on electrodes, collision cross sections and other model conditions remained the same as were described in Chapter 8.2. Input file used for initialization of this simulation is attached in Appendix B.

Results of the above described simulation taken from snapshot at simulation time $t = 2.9$ $\mu$s are depicted in figure 9.7. The electron density profile depicted

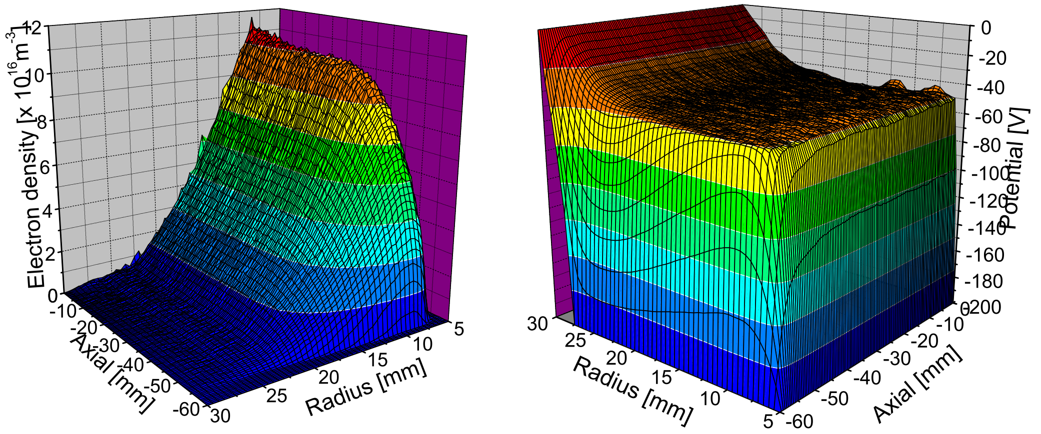

(a) (b)

Figure 9.7: Results of the simulation of the argon discharge in magnetron at $p = 4$ Pa, $B = 20$ mT, $U = 200$ V with grid with $1250 \times 500$ cells and approximatively 12 superparticles per cell. Data are taken from snapshot at $t = 2.9$ $\mu$s. (a) electron density profile ; (b) plasma potential profile

in figure 9.7(a) has in radial direction shape that is typical for magnetically supported glow discharges in the cylindrical magnetron. The electron density is axially almost homogenous in major part of the discharge region beginning at the mirror boundary in the center of magnetron at $z = 0$ mm and than falls down toward the limiter placed at the axial position $z = -60$ mm. The plasma potential depicted in figure 9.7(b) has relatively flat plateau of the positive column at voltage around $U_{pl} = -50$ V with narrow region of the cathode fall in the vicinity of the cathode and the limiter. The anode fall is relatively pronounced and run radially into one third of the discharge region. The plasma potential profile is smoother and less fluctuating than it was in the case of previous simulation with 2 superparticles per cell in average.

### 9.2.1 Temporal development

The temporal evaluation of number of superparticles in simulation is depicted in figure 9.8. The number of superparticles reached saturated value corresponding to the steady state of the glowing discharge. The principal problem connected with monotonous grow of charged particles population in simulations with rougher grid was therefore solved by choosing grid cell dimensions comparable to the Debye length. At simulation time $t = 3.03$ $\mu$s the model parameters were changed in order to optimize the simulation according to [Kawamura *et al.* (2000)]($\triangle t =$

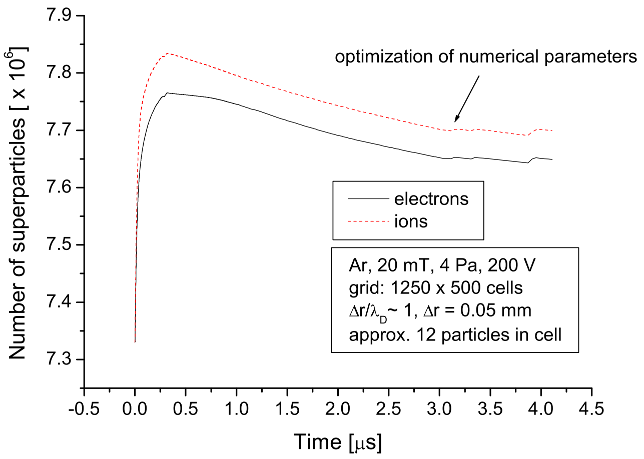

Figure 9.8: The temporal evolution of the number of superparticles in simulation with grid with 1250 × 500 cells.

$4 \times 10^{-11}$ s, subcycling of ions was set to 40). However, it led into the numerical instability. Therefore prior stable results are presented here and compared with experiment.

The temporal development of plasma parameters in simulation is presented in figures 9.9, 9.10 and 9.11. Figure 9.9 illustrates the temporal development of

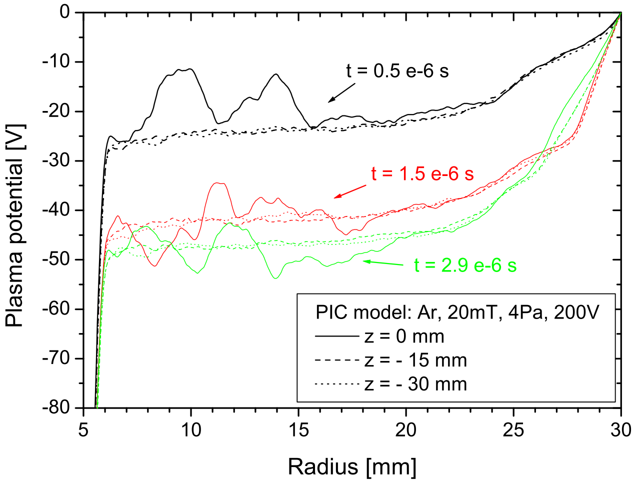

Figure 9.9: The temporal evolution of the plasma potential in the simulation with grid with $1250 \times 500$ cells at three different axial positions. $z = 0$ mm denotes the center of the magnetron.

the plasma potential profile showing that the simulation was probably reaching the steady state since the plasma potential plateau seems to go to stabilize at the value around $U_{pl} = -50$ V. The anode potential fall grew from approximatively 20 V at $t = 0.5$ $\mu$s to approximatively 45 V at $t = 2.9$ $\mu$s during the simulation. Plasma potential in the vicinity of the mirror boundary ($z = 0$ mm) was more noisy and fluctuating than at other axial positions because of Neumann boundary condition[1] that was applied at the dielectric reflecting boundary.

The temporal development of the charged particles density profiles is depicted in figures 9.10 and 9.11 for electrons and single charged argon ions respectively.

---

[1] only normal derivative of potential is fixed at the boundary: $dU/dz = 0$

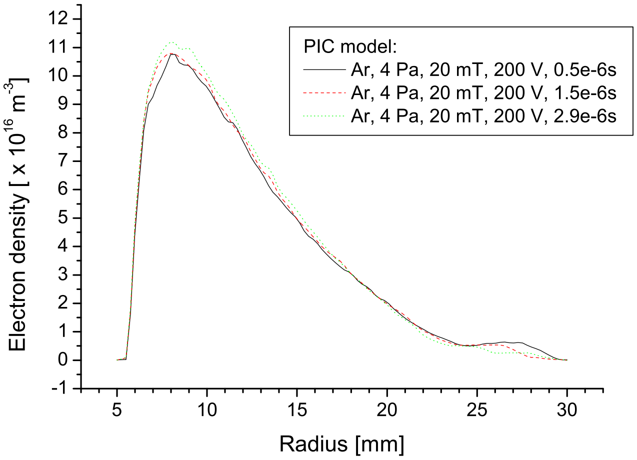

Figure 9.10: The temporal development of the radial profile of the electron density at $z = -1.2$ mm in the simulation with grid with $1250 \times 500$ cells. Profiles were not taken directly at the central plane because of bigger noise directly at the mirror boundary.

While ions were redistributing towards the cathode in figure 9.11, electrons get to their positions near the cathode faster and only smoothing of the profile and small growth of its maximum can be observed in figure 9.10 during the simulation.

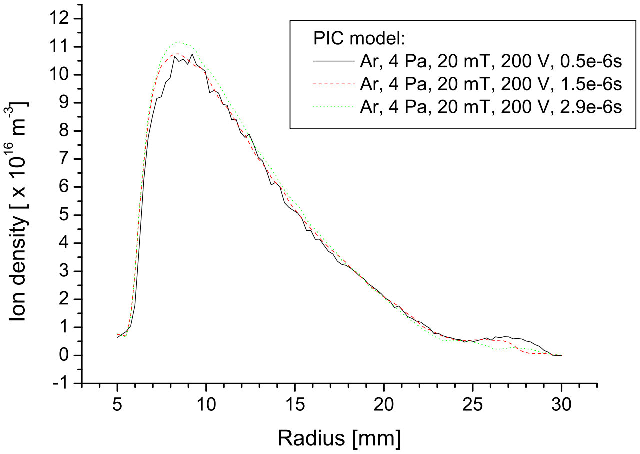

Figure 9.11: The temporal development of the radial profile of the ion density at $z = -1.2$ mm in the simulation with grid with $1250 \times 500$ cells.

# Chapter 10

# Comparison with experiment

## 10.1 Density profiles

The radial profiles of the electron and ion density obtained in the above described 2D PIC-MCC simulation with $1250 \times 500$ grid cells and approximatively 12 superparticles per cell (see Chapter 9.2) in the vicinity of the central plane of the magnetron ($z = 0$ mm) at the simulation time $t = 2.9$ $\mu$s are depicted in figure 10.1 and compared there with electron density profiles obtained by Langmuir probe for three different discharge currents in experiment. Experimental data were recorded by radially movable Langmuir probe positioned in the central plane of magnetron (see figure 8.1). The experiment was described and these data were presented in more detail in [Bilyk (2005)].

The discharge current in voltage source driven simulation was determined by averaging of the charged particles flow on the boundaries over approximatively 200 time steps at the simulation time $t \approx 3$ $\mu$s. The average value of the discharge current was found approximatively 75 mA in one half of the magnetron discharge area that was simulated in the model resulting to approximatively $I \doteq 151$ mA in the whole magnetron. It is higher than in the depicted available experimental results. However, assuming the linear dependence of the charged particles density on the discharge current in the first approximation the simulation results can be quantitatively compared. The dependence of the charged particles density on the discharge current was measured by J. Rusz in [Rusz (2003)] and it is depicted in figure 10.2 showing that the linear dependence can be used in first

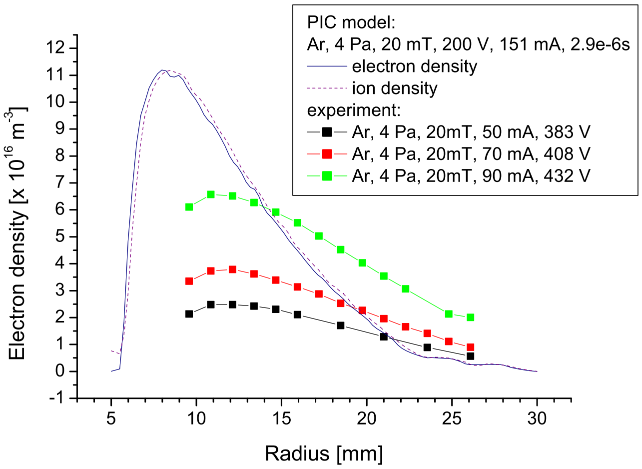

Figure 10.1: Comparison of the computed radial density profiles with experimental data measured in the central plane of the cylindrical magnetron at various discharge currents. Data were taken from [Bilyk (2005)].

approximation, although the dependence is in reality a little bit faster near the cathode. Assuming the linear dependence the maximum of density profile would be approximately $n_e \approx 1.2 \times 10^{17}$ m$^{-3}$ at $I = 150$ mA that corresponds pretty well with the simulation data.

The simulation data depicted in figure 10.1 have similar profile as those obtained in experiment and also corresponding magnitude as discussed in previous paragraph but the maximum is closer to the cathode in comparison to the experimental data. In contrast to that is the comparison with former data measured by E. Passoth where the density maximum was approximatively at the same position as in the simulation. This comparison is shown in figure 10.3. The electron density decay near the anode is faster in the simulation than in experiment depicted in figure 10.3 and the simulation results corresponds better to the case of discharge at higher magnetic field but at the same $B/p$ coefficient – $B = 25$ mT and $p = 5$ Pa – than to the case of $B = 20$ mT and $p = 4$ Pa. Anyway, simulation results agree with the experimental data obtained at $B = 20$ mT and $p = 4$ Pa and depicted in figure 10.3 still relatively well. Note the ion density in the vicinity

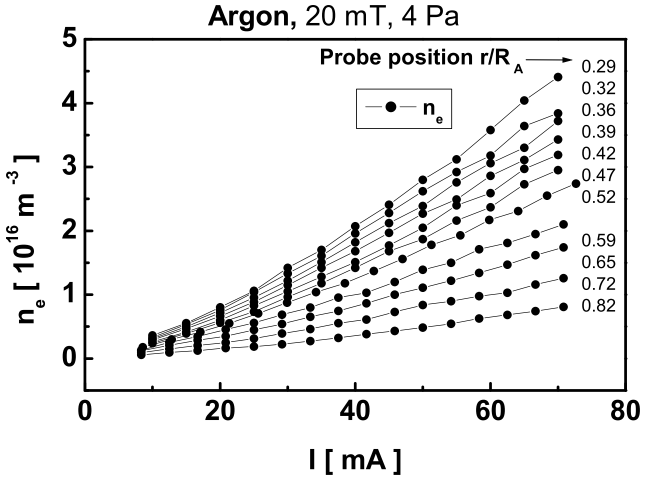

Figure 10.2: Electron density at various radial positions in dependency on the discharge current in the cylindrical magnetron. Data were taken from [Rusz (2003), fig. 15, page 37].

of the cathode, that is in the simulation correctly higher than the electron density since the positively charged argon ions are attracted by the negative potential of the cathode and electrons are repelled.

The discrepancy between the experimental results given in figures 10.1 and 10.3 was probably caused by worse spatial resolution of the probe used for obtaining the data given in figure 10.1 that is expressed in the density profile flattening.

### 10.1.1 Axial density profiles

Axial profiles of the electron density obtained at the simulation time $t = 2.9$ $\mu$s are depicted for different radial positions in figure 10.4. They can be qualitatively compared with experimental results obtained by M. Holík by axially movable Langmuir probe for the discharge current $I = 50$ mA and various magnetic field that are depicted in figure 10.5 and were presented in [Holík *et al.* (2004)]. The decrease of density at higher magnetic field in figure 10.5 was caused by contracting of the plasma closer to the cathode as the magnetic field increased. Note, that

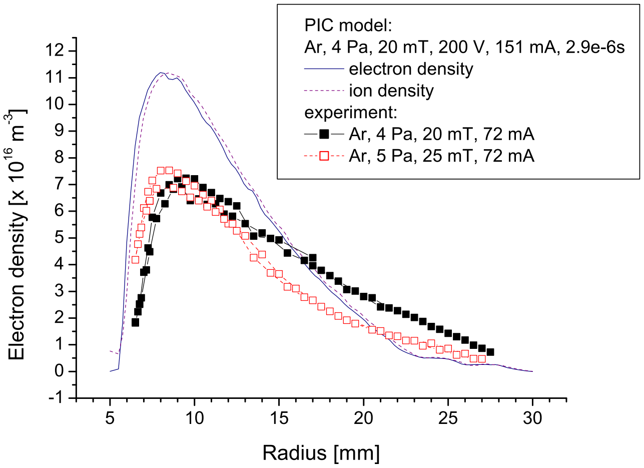

Figure 10.3: Comparison of the computed radial density profiles with experimental data measured by E. Passoth in the central plane of the cylindrical magnetron conserving the $B/p$ corresponding to the simulation conditions.

the plasma was also axially contracted with increasing magnetic field strength.

The shape of simulation axial profile corresponds better with the experimental results obtained at $B = 10$ mT, where the plasma was more axially homogenous, than with the case of $B = 20$ mT.

### 10.1.2 Results obtained in the early simulation

The comparison of the radial density profile computed in early simulation with grid with $40 \times 100$ cells (see figure 9.3) with the Langmuir probe data that is given in figure 10.6. The profile is relatively noisy and the position of the maximum of density is closer to cathode in simulation similar to that presented in figure 10.1. However, the magnitude and the shape of the profile are relatively similar to the experiment especially at considering the low computational cost of simulation with $40 \times 100$ cells in grid.

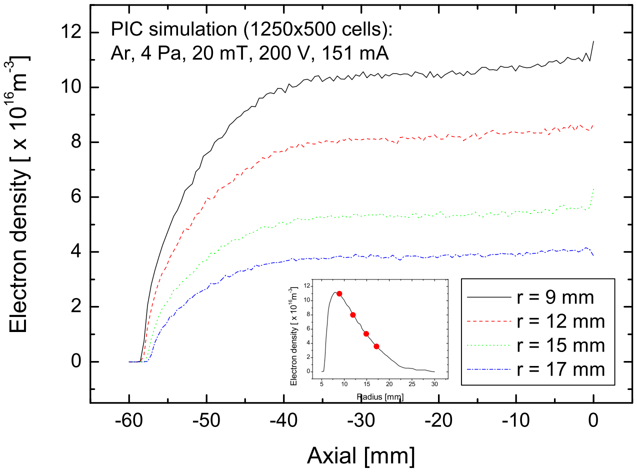

Figure 10.4: Computed axial density profiles at different radial positions in the cylindrical magnetron.

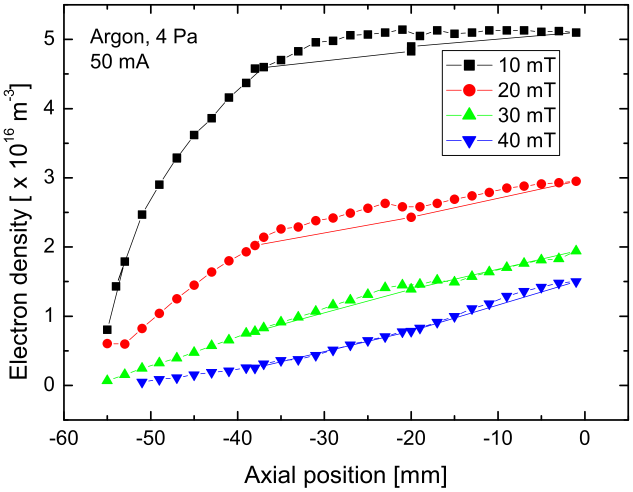

Figure 10.5: Density profiles measured by axially movable Langmuir probe in the cylindrical magnetron discharge at the discharge current $I = 50$ mA and various magnetic field. Data were taken from [Holík *et al.* (2004)].

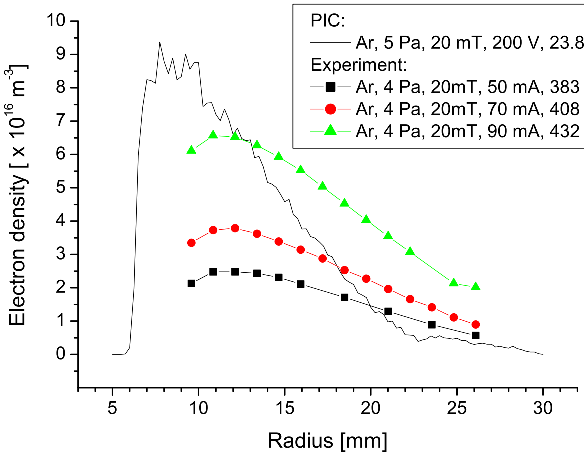

Figure 10.6: Comparison of the computed radial density profile obtained in the simulation with grid with 40 × 100 cells at $t = 23.8$ $\mu$s with the Langmuir probe data.

## 10.2 Plasma potential profiles

Another important quantity for comparison with experiment is the plasma potential. Plasma potential profiles were measured by means of Langmuir and emissive probes in the magnetron. Experimental results are given in figure 10.7. Emissive probe data were measured by the strongly emitting probe technique. The emissive probe data were overestimated approximately by 3 V in this case[1]. However, obtained plasma potential profile can be compared with Langmuir probe data and with the simulation results omitting the shift. Corrected emissive probe data correspond to the plasma profile obtained via Langmuir probe – in both cases the plasma potential in positive column was almost constant with the potential of the plateau few volts below zero. Anode fall was small and protruded only few millimeters into the plasma. Almost the whole applied voltage was spent in the cathode fall region. The step change in the plasma potential profile determined by emissive probe at discharge current $I = 100$ mA was probably caused

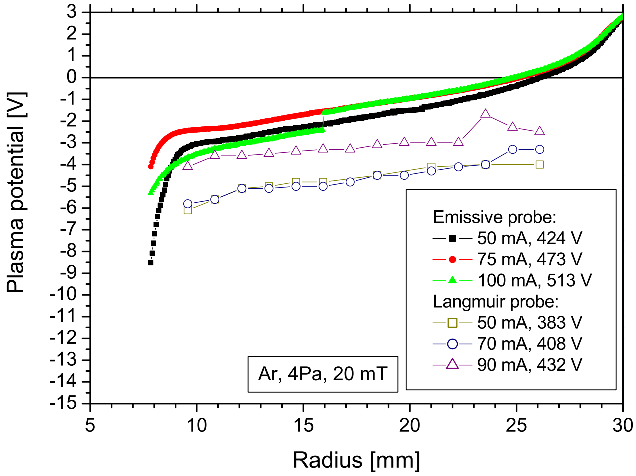

Figure 10.7: Radial profiles of the plasma potential measured in the central plane of the cylindrical magnetron by means of Langmuir and Emissive probes.

---

[1] This was discussed in Chapter 4.3 in Part I.

by switching of the discharge into the another mode of burning (see e.g. [Rusz (2003)], Chapter 4, pp 39-42).

In contrast to that the plasma potential profile obtained in presented simulation and depicted in detail in figure 10.8 has different structure: Almost one

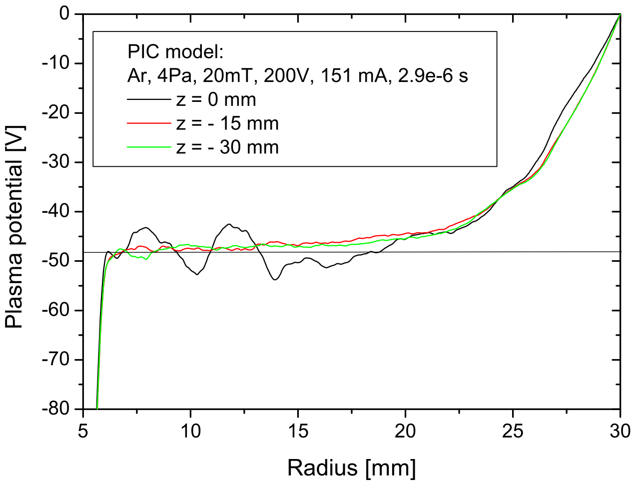

Figure 10.8: Radial plasma potential profiles computed at different axial positions in simulation with $1250 \times 500$ cells and with 12 superparticles per cell in average at the simulation time $t = 2.9\ \mu$s.

quarter of the applied voltage is spent in anode fall region that protrudes further into the discharge region in comparison with experiment. This is the main discrepancy in comparison with the experiment since the anode fall is followed by reasonable flat positive column region and with narrow cathode fall region where the rest of applied voltage is spent. The cathode fall was broader in experiment than in the simulation, but the emissive probe data were limited by spatial resolution of the probe (probe loop had length of 5 mm and it was believed that the strongest emission was really from the probe tip) and by validity of the strongly emissive probe technique used for plasma potential determination that is applicable only in quasi-neutral plasma [Wilson *et al.* (2002)], which was not the case of the cathode fall. Furthermore strongly emitting probe may influence the discharge if it was set too close to the cathode. For these reasons we were not able to correctly measure the plasma potential by the emissive probe in close vicinity of the cathode.

Another discrepancy that appeared in comparison with the experiment was the total applied discharge voltage. That was $U = 200$ V in case of the model and approximatively $U \approx 400$ V in the case of experiment conserving the same discharge conditions and at almost comparable plasma density in the discharge region.

# Chapter 11

# Discussion of results

Although relatively reliable and stable results were obtained in presented simulation with the more precise grid, the simulation results didn't agree with experiment in all aspects. The discrepancy between the simulation and experiment was most obvious in case of the plasma potential profile that is sensitive even to small discrepancies in charged particles distribution in the discharge region. The discrepancy could be caused by several reasons:

## 11.1 Short simulation time

Firstly it can be because of relatively short simulation time that was in presented simulation approximatively 3 $\mu$s. In order to disengage from the starting density profile ions should ideally cross the discharge region more times. However, it would take tens or hundreds of microseconds because at considering the thermal velocity of ions at room temperature as an governing velocity for ions redistributing, ions travelled only something more than 1 mm during presented simulation time.

In order to avoid this need and in order to minimize the computation time needed for reaching the steady state the simulation was started from density profiles obtained in previous simulation that were believed to be close to the correct results.

As it can be seen from temporal development of the radial plasma potential profile that is depicted in figure 9.9, where the potential plateau in the positive column region seemed to stabilize near value $U_{pl} = -50$ V, the simulation was going to reach the steady state despite rather short simulation time. On the other hand it is possible that it is not the final state since the density profiles depicted in figures 9.10 and 9.11 were still changing. Charged particles were moving from region near anode to the region of the maximal density. In other words: it is possible that nonphysically big anode fall established only in order to pull the particles away from the anode vicinity and it will vanish after particles will be redistributed. The resulting plasma potential profile could be then more consistent with the experiment.

Another issue connected with rather short simulation time can be shown on the temporal development of the number of superparticles in simulation that is depicted in figure 9.8. The number of superparticles grew fast at the very beginning of simulation ("avalanche") that was connected with increased ionization near the cathode as non-physically positioned electrons turned their potential energy into the kinetic one. This phase should be followed with phase where extra particles originating from the staring "avalanche" diffuse to walls. This phase is connected with moderate decrease of the number of superparticles in simulation and results after some time into the steady state solution. As it can be seen from figure 9.8 the phase following the "avalanche" was not probably over in presented simulation at time $t \approx 3$ $\mu$s.

Verification of both above suggested explanations of discrepancy of simulation results can be done only in further run of the simulation. However, it has to be done in more powerful computing system since performing the presented simulation for tens or hundreds microseconds of simulation time will take great computational power. For illustration, presented data (3 $\mu$s of the discharge; grid with $1250 \times 500$ cells; approximately 8 millions particles for each species; timestep $\triangle t = 10^{-11}$ s) were obtained in simulation that costed 6 months on Intel® Xeon$^{\mathrm{TM}}$ CPU at 3 GHz and spent 0.6 GB of the computational memory if performed without diagnostics. That's why employing the code parallelization connected with precise optimization of simulation conditions and running the simulation on some cluster or supercomputer that would significantly shorten the computation time will be needed.

It should be noted that the OOPIC code was already successfully parallelized by authors (PTSG group, University of California, Berkeley) in electromagnetic version. The electrostatic code is not to our knowledge parallelized yet. Implementation of parallelized 2D Poisson equation solver is needed for that at present time.

## 11.2 Secondary emission from electrodes

Another reason for discrepancy of simulation results can be found in the coefficient of secondary emission from electrodes. This coefficient was set to 0.2 for metallic part of magnetron in simulation similarly as it was done e.g. in [Hammel & Verboncoeur (2004)]. However, recently it was found in literature that the coefficient of secondary emission is in reality substantially lower. Regarding to the review article [Phelps & Petrović (1999)] the coefficient of secondary emission is almost constant at energies of impinging Argon ions lower than 300 eV for all tested materials in case of the clean surface. Its magnitude is for most mentioned materials lower than 0.1. If the metallic surface is not clean the coefficient of secondary emission is even substantially lower for low impinging argon ion energies – in some cases even by order of magnitude or more – and it is also no more constant in this energetic region. Since the material of the cathode was continually sputtered during the discharge in magnetron its surface can be considered as clean and the coefficient of secondary emission from metallic surfaces was therefore probably close to 0.1.

The higher coefficient of secondary emission was probably responsible for higher efficiency of the discharge burning in model since secondary electrons emitted from cathode are important for sustaining the discharge. Higher emission of secondary electrons flowing from cathode probably also influenced the structure of the plasma potential profile, although the main reason for the big anode fall was probably connected with the short simulation time discussed above.

## 11.3 Electron temperature used for initialization of simulation

Another reason for the higher efficiency of burning of the discharge in contrast to experiment as mentioned in Chapter 11.2 could be found in the electron temperature used initialization of simulation. It was initialized by Maxwell-Boltzmann distributed electrons with characteristic temperature $T_e = 3$ eV. If the temperature of electrons used for initialization of simulation was higher than in reality, there is an additional energy present in system that has to dissipate prior to obtain stable and correct results.

## 11.4 Charged particles interactions

Next reason for discrepancy of simulation results and experiment could be found in omitting of some important process in argon discharge.

In our model following interactions were considered: elastic collisions, excitation and ionization for electrons and elastic collisions and charge exchange interaction for single charged argon ions.

Let me discuss importance of some other interactions that could be relevant in the discharge:

Beginning at intermediate pressures the stepwise ionization due to metastable levels play important role in argon discharges. Metastable levels are levels that cannot decay to any lower levels via optically allowed transitions. First two argon metastable levels $1s_3$ and $1s_5$ have lifetimes of 1.3 and 3.8 s respectively and the cross-sections for interactions with these metastable levels are two or three orders of magnitude grater than those of the ground state. Including of metastable states into the model can be important because of combination of large cross section and relatively low treshold energies.

The importance of the effect of stepwise ionization in our low pressure case can be determined according to results presented in [Roberto *et al.* (2003)]. In [Roberto *et al.* (2003)] 1D PIC-MCC model of argon radio-frequency driven discharge was applied for study of the influence of metastables on discharge at various discharge conditions. The model included such interaction as metastable creation, ionization from the metastable state, metastable quenching to resonant level and metastable pooling. The metastable excited atoms were treated in model as particles. It was found that for the low pressure case (for 50 mTorr $\doteq$ 7 Pa) the metastables had little influence on the discharge. In our case, the pressure was even lower than in cited work. Therefore we can conclude that the influence of metastables on discharge was also negligibly small in our case of dc discharge at pressure of 4 Pa although the study of the influence of metastables was done for rf driven discharge. The influence of metastables was therefore excluded as a significant factor causing the discrepancy of our simulation results from the experiment.

The Coloumb collisions should not play important role in our case as well, since they take effect only at higher charged particles densities. This was shown in our previous 1D simulations where the computationally consuming Coloumbic electron-electron interaction was incorporated.

According to our previous estimations recombination of charged particles in volume should be also negligible as well as the secondary emission of electron from electrodes induced by energetic photons. Their neglecting in the model was therefore correct.

Some non-negligible role in the discharge can play interaction of charged particles with sputtered metal atoms. This process was not included in the model and can probably contribute to discrepancy between model and experiment. However, it will not be probably substantial.

## 11.5 Computational grid

Finally the last reason for the found discrepancy between simulation results of presented model and experiment could be because of the computational grid used in simulation. Although cells dimensions were comparable with the Debye length in both directions, the grid was maybe still not fine enough and the electric field was not properly resolved. In case of rf driven discharges it is possible to employ the direct implicit simulation scheme [Vahedi *et al.* (1993)] in order to obtain time averaged plasma properties. In this approach only averaged sheath size near electrodes and the rf drive frequency must be resolved (usually $s \gg \lambda_D$)

that massively reduce the computational power that is otherwise needed, however it is not our case and that's why the Debye length should be properly resolved by the grid.

# Chapter 12

# Conclusions of part II

2D PIC-MCC model of the dc glow discharge in the cylindrical magnetron was described and presented here. Simulations were started with rough computational grid at the very beginning in order to obtain density profiles usable for initialization of the next simulations with more precise grid that followed. Results of the most recent simulation with 1250 × 500 cells in grid, where the cell length was comparable with the Debye length, were presented in more detail here and compared with experiment. The results were in relatively good agreement with experimental data. Although reliable data were obtained in this simulation, they did not agree in all aspects with presented experiment. The discrepancy was most obvious in the plasma potential profile. The discrepancy can be most likely to ascribed to the relatively short simulation time that resulted from computational size of the presented simulation. From this point of view a comparison of discussed results with previous simulation with 40 × 100 cells is interesting, where also relatively comparable results were obtained employing much smaller computational power. However, the number of superparticles steadily grew in that simulation and it was not therefore correct.

Although simulation results did not agree precisely with experimental data, stable model of the discharge in the cylindrical magnetron was created and further computational power when applied to the debugged code of presented simulation will probably bring fruitful results.

# Chapter 13

# Summary

In the first part of this work thorough study of variations of electron saturation current of the emissive probe at varying probe heating was performed in two types of argon low temperature plasma: (i) weakly magnetized plasma of dc discharge in cylindrical magnetron and (ii) non-magnetized plasma generated in so called Double-Plasma(DP) machine. The variations were characterized and possible processes generating them were suggested and discussed. First results of the study were presented in [Marek *et al.* (2006b)]. In [Picková *et al.* (2006)] various techniques for interpreting the emissive probe data obtained in the cylindrical magnetron data were compared. The presented work was especially focused on the study of the overestimation of the plasma potential by strongly emitting probe in the low temperature plasma. The overestimation of the plasma potential was discussed on the basis of obtained results, compared with 1d analytical model in this work and the results were presented in [Marek *et al.* (2007)]. The DP-machine results were presented independently in [Gstrein *et al.* (2006)]. Obtained experimental and model results give useful measure for applicability of the strongly emitting probe technique in the low temperature plasma.

In the second part of thesis results of 2d PIC-MCC numerical model of the dc discharge in the cylindrical magnetron were presented and compared with experiment. The progress in simulations was presented in several publications [Marek *et al.* (2004, 2005a,b, 2006a)]. Numerically stable model was created. It was found that longer simulation time is needed to obtain steady state results. Further computational run of this simulation will probably bring fruitful results.

Experimental data obtained for comparison with simulation were presented e.g. in [Holík *et al.* (2004)].

The aims of work, which were set up in Chapter 1, were fulfilled and next progress of work was suggested. In addition author of this work participated in Monte Carlo simulations of the electron current collected by Langmuir probe [Trunec *et al.* (2004)] and in the study of plasma potential fluctuations in the cylindrical magnetron device [Bilyk *et al.* (2004a,b, 2006)].

# Appendix A

# Floating potential of the strongly emitting probe – analytical model

As mentioned in Chapter 2.2.3, analytical model describing strongly emitting probe was developed in [Takamura *et al.* (2004)]. Theoretical formula, that can describe an electron emission from plasma-facing solid surfaces under space charge limited condition was derived there. Ions were assumed to be cold, however, a finite temperature of emitted electrons from the solid surface was taken into account. Schematics of 1-D potential in front of the emitting wall used in the analytical model is depicted in figure A.1. As described in Chapter 2.2.3 the space potential well is formed in front of strongly emitting surface when electrons are emitted with non-zero kinetic energy. So-called "Virtual Cathode" is formed in front of the emitting surface at larger emissions, which reduces thermionic emitted current.

The area in front of the strongly emitting wall is divided into two separate parts in the model: region $\alpha$ – from the plasma to the virtual cathode and to region $\beta$ – between the virtual cathode and the solid surface.

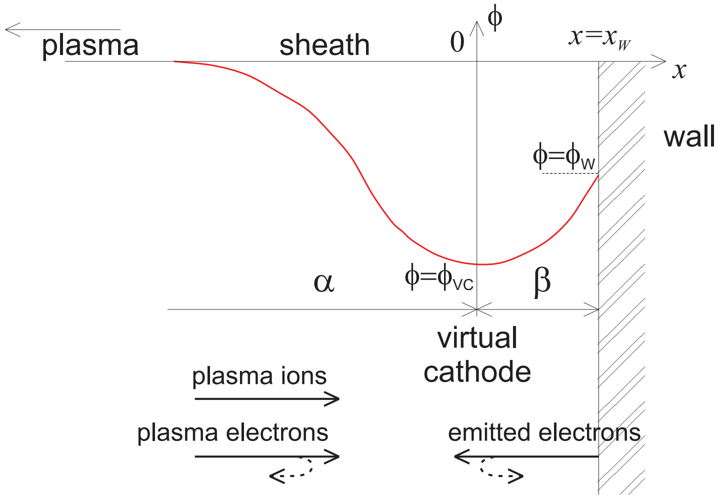

Figure A.1: Schematics of 1-D sheath model with sufficient electron emission from the wall presented in [Takamura *et al.* (2004)].

## A.1 Modeling in region $\alpha$

The space potential far from the solid surface is assumed to be zero. Potential in region $\alpha$ can be obtained by solving Poisson equation

$$\frac{d^2\varphi}{dx^2} = -\frac{e}{\varepsilon_0}(n_i(x) - n_e^p(x) - n_e^s(x)), \tag{A.1}$$

where $n_i(x)$ is ion density, $n_e^p(x)$ is the plasma electron density and $n_e^s(x)$ is emitted electron density in region $\alpha$. It is assumed that ions are accelerated by the electric field in the sheath towards the solid surface without any collisions. The ion density can be expressed by solving ion velocity $V$ from energy conservation law $\frac{1}{2}m_iV^2 + e\varphi$ =Const and its substituting to the continuity equation of ion flux $\frac{dn_iV}{dx} = 0$ and employing Bohm criterion of ion velocity at the sheath edge by:

$$n_i(x) = n_0 \left(1 - \frac{1}{M^2}\frac{2e\varphi}{kT_e}\right)^{-\frac{1}{2}}, \tag{A.2}$$

where $n_0$ is the ion density at the plasma–sheath edge and $M$ is the mach number defined by:

$$M = V_0 \left(\frac{kT_e}{m_i}\right)^{-\frac{1}{2}}, \tag{A.3}$$

where $V_0$ is the ion velocity at the plasma–sheath edge and $\sqrt{\frac{kT_e}{m_i}}$ is the ion sound velocity. The electron density is given by the Boltzmann relation:

$$n_e(x) = n_{e0}^{p} \exp\left(\frac{e\varphi(x)}{kT_e}\right), \tag{A.4}$$

where $n_{e0}^{p}$ is the plasma electron density at the plasma–sheath edge. The emitted electrons are assumed to have the Maxwell-Boltzmann velocity distribution[1]:

$$f(v_0) = N_0 \left(\frac{m_e}{2\pi kT_{eW}}\right)^{\frac{1}{2}} \exp\left(-\frac{m_e v_0^2}{2kT_{eW}}\right). \tag{A.5}$$

The emitted electron density $n_e^s(x)$ can be obtained by the continuity for the emitted electrons:

$$dj_e^s = ev(x, v_0)dn_e^s(x) = ev_0 f(v_0). \tag{A.6}$$

The emitted density $n_e^s(x)$ can be obtained by integrating Eq. A.6 over $v_0$:

$$n_e^s(x) = \int_{v_{VC}^s}^{\infty} \frac{v_0 f(v_0)}{v(x, v_0)} dv_0, \tag{A.7}$$

where $v_{VC}^s$ is the minimum velocity of emitted electrons, which is necessary to override the potential barrier at the virtual cathode. It means, those emitted electrons may move into region $\alpha$ from the region $\beta$. The energy conservation for emitted electrons entering into the region $\alpha$ gives:

$$\frac{1}{2}m_e v^2(x, v_0) - e\varphi(x) = \frac{1}{2}m_e v_0^2 - e\varphi_W, \tag{A.8}$$

where $\varphi_W$ is potential of the emitting wall. Solving for $v(x, v_0)$ from Eq. A.8 and substituting $v(x, v_0)$ into Eq. A.7 is obtained:

$$n_e^s(x) = n_{eVC}^s \mathrm{erfc}\left(\sqrt{\frac{e(\varphi - \varphi_{VC})}{kT_{eW}}}\right) \exp\left(\frac{e(\varphi - \varphi_{VC})}{kT_{eW}}\right), \tag{A.9}$$

---

[1] Note, that distribution of thermionic emitted electrons differs as was shown in Chapter 2.2.1.

where $n^s_{eVC}$ is the emitted electron density at the virtual cathode position VC, which is given by the following relation:

$$n^s_{eVC} = \frac{N_0}{2} \exp\left(\frac{e(\varphi_{VC} - \varphi_W)}{kT_{eW}}\right). \tag{A.10}$$

The complementary error function erfc$(y)$ is defined by:

$$\mathrm{erfc}(y) = \frac{2}{\pi} \int_y^\infty e^{-t^2} dt. \tag{A.11}$$

Quasi-neutrality at the plasma–sheath edge is expressed by:

$$n_0 = n^p_{e0} + n^s_e(-\infty). \tag{A.12}$$

By applying of derived equations for densities into Eq. A.1 and after solving it at the position of virtual cathode by using some substitutions, following polynomial expression was derived in [Takamura *et al.* (2004)]:

$$(EG + 1)(\beta^*_3 G^3 + \beta^*_2 G^2 + \beta^*_1 G + \beta^*_0) = 0, \tag{A.13}$$

where

$$\begin{aligned}
\beta^*_3 &= EF^2 - 2A^2F + 2\phi_{VC}A^3, \\
\beta^*_2 &= F^2 + 2EF(e^{\phi_{VC}} - 1) - 2(A^2(e^{\phi_{VC}} - 1) + 2AF) + 6\phi_{VC}A^2, \\
\beta^*_1 &= 2(F - 2A)(e^{\phi_{VC}} - 1) + E(e^{\phi_{VC}} - 1)^2 - 2F + 6\phi_{VC}A, \\
\beta^*_0 &= (e^{\phi_{VC}} - 1)^2 - 2(e^{\phi_{VC}} - 1) + 2\phi_{VC}, \qquad (A.14)
\end{aligned}$$

and $A, E, F$ are defined by

$$\begin{aligned}
A &= \sqrt{-\pi\phi_{VC}C}\,\mathrm{erfc}(-\pi\phi_{VC}C)\exp(-\pi\phi_{VC}C), \qquad (A.15)\\
E &= C(A - 1), \qquad (A.16)\\
F &= -\frac{A}{C} + 2\phi_{VC} + \sqrt{\frac{-\pi\phi_{VC}}{C}}, \qquad (A.17)
\end{aligned}$$

where $\phi_{VC} = \frac{e\varphi_{VC}}{kT_e}$ is normalized potential and $C = \frac{T_e}{T_{eW}}$.

Solution from the first factor of Eq. A.13: $EG+1 = 0$ has no physical meaning as explained in [Takamura *et al.* (2004)]. The second factor gives a cubic equation, which has three real solutions. Only one solution satisfies the condition $G > 0$ that is required as explained at the same place.

The space charge limited emitted current density on the position of the virtual cathode can then be described as a function of $\phi_{VC}$ as follows:

$$\frac{j_e^s}{j_{is}} = \frac{G\sqrt{-\pi\phi_{VC}}}{1+AG}\sqrt{\frac{2m_i}{\pi m_e}}, \tag{A.18}$$

where the ion saturation current density $j_{is}$ is defined by:

$$j_{is} = en_0\sqrt{\frac{k(T_e+T_i)}{m_i}}. \tag{A.19}$$

The ion current density flowing on the position of virtual cathode can be expressed by:

$$j_i^+ = \sqrt{\frac{1+AG}{1+EG}}j_{is} \tag{A.20}$$

and the plasma electron current density as:

$$j_e^p = \frac{e^{\phi_{VC}}}{2(1+AG)}\sqrt{\frac{2m_i}{\pi m_e}}j_{is}{}^{1} \tag{A.21}$$

The floating condition at the position of virtual cathode can be than expressed by:

$$j_e^p - j_i^+ - j_e^s = 0. \tag{A.22}$$

Solving the Eq. A.22 numerically the potential at the position of virtual cathode can be obtained (i.e. potential fall in region $\alpha$). Note, that according to Eqs. A.18, A.20 and A.21, the potential fall in region $\alpha$ depends only on ratio $T_e/T_{eW}$ since $j_{is}$ can be canceled out in Eq. A.22. The potential fall in region $\alpha$ obtained by applying and numerically solving of above described model is depicted in dependence on $T_e/T_{eW}$ in figure A.2.

---

[1] Note, corrected sign in comparison to [Takamura *et al.* (2004)] in order to fullfil Eq. A.22 given at the same place.

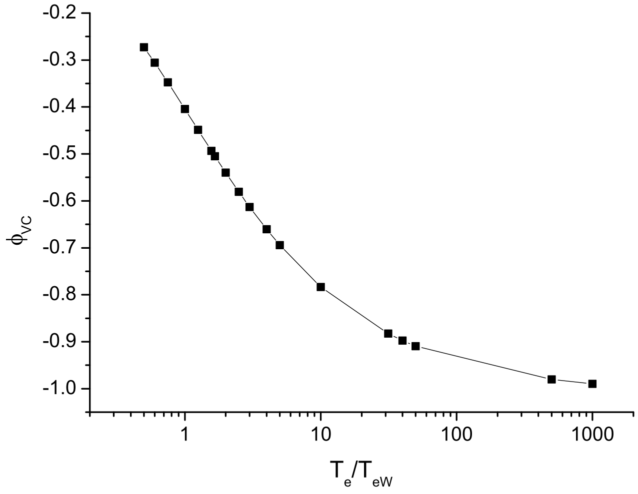

Figure A.2: Normalized potential at the position of virtual cathode formed in front of emitting surface in respect to the plasma potential computed according to the analytical model presented in [Takamura *et al.* (2004)] at the floating probe condition. $\phi_{VC} = \frac{e\varphi_{VC}}{kT_e}$.

## A.2 Modeling in region $\beta$

Once the potential fall $\varphi_{VC}$ in region $\alpha$ is obtained together with currents flowing over the virtual cathode at the floating probe condition, potential fall between the probe wall and the virtual cathode can be computed from relation between emitted current density from the wall $j_{em}$ and charge limited current density $j_e^s$ flowing to the plasma at the position of virtual cathode given as:

$$j_e^s = j_{em} \exp\left(\frac{e(\varphi_{VC} - \varphi_W)}{kT_{eW}}\right), \tag{A.23}$$

where $j_e^s$ is determined by Eq. A.18 and $j_{em}$ is given by Richardson-Dushmann formula (Eq. 2.7):

$$j_{em} = A_{RD} T_W^2 e^{-\frac{\chi_0}{kT_W}}. \tag{A.24}$$

Normalized potential at the wall $\phi_{VC}$ computed for density typical in cylindrical magnetron discharge and two different temperatures of plasma electrons in dependence on varying temperature of the wall $T_W$ is depicted in figure A.3. The data were computed at assumption that thermionic emitted electrons have

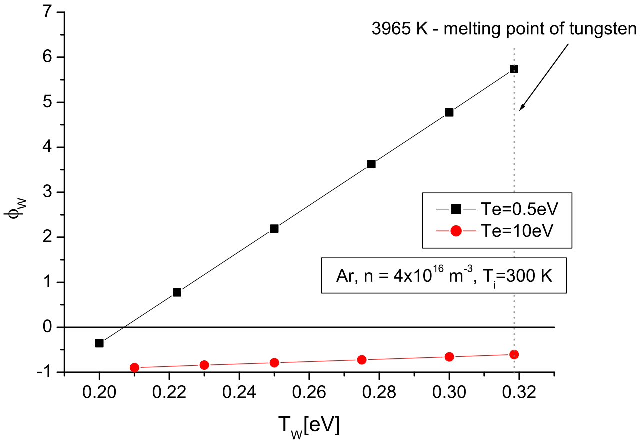

Figure A.3: Overestimating of the plasma potential by strongly emitting probe as computed by the analytical model presented in [Takamura *et al.* (2004)] for two different electron temperatures in plasma. Following parameters were set into the model: discharge in Ar, $n_e = 4.10^{16}$ m$^{-3}$, $T_i = 300$ K; tungsten probe: $\varphi_{work} = 4.5$ eV, $A_{RD} = 70 \times 10^4$ Am$^{-2}$K$^{-2}$.

Maxwell-Boltzmann distribution with characteristic temperature equal to the temperature of the wall ($T_{eW} = T_W$).

# Appendix B

# Input file for OOPIC

```
half_magnetron.inp

{

finer grid

}

Variables

{

    Torr_per_Pa = 1 / 133

    kb = 1.38e-23

    e0 = 1.602e-19

    K_per_eV = e0 / kb

    amu = 1.66e-27

    me = 9.11e-31


    z_max = 0.12

    r_min = .005
```

```
    r_max = .03


    Zcells = 1250
    Rcells = 500
}
Region
{
    name = CMD
    Species
    {
        name = argon_plus_ions
        m = 40*amu
        q = e0
        subcycle = 6
        collisionModel=2
    }
    Species
    {
        name = electrons
        m = me
        q = -e0
        collisionModel=1
    }
    Grid
    {
```

```
    J = Zcells

    x1s = -z_max/2

    x1f = 0.0

    n1 = 1.0

    K = Rcells

    x2s = r_min

    x2f = r_max

    n2 = 1.0

}

Control

{

    dt = 1e-11

    ElectrostaticFlag = 1

    B01 = 0.02

    BOnlyInZFlag=1

    nSmoothing=4

    NonRelativisticFlag=1

}

MCC

{

    gas = Ar

    pressure = 4*Torr_per_Pa

    eSpecies = electrons

    iSpecies = argon_plus_ions

    ecxFactor = 1
```

```
}
Dielectric
{
    name = CentralPlane
    j1 = Zcells
    k1 = 0
    j2 = Zcells
    k2 = Rcells
    normal = -1
    reflection = 1
}
Conductor
{
    name = Anode
    j1 = 0
    k1 = Rcells
    j2 = Zcells
    k2 = Rcells
    normal = -1
    Secondary
    {
        secondary = 0.2
        secSpecies = electrons
        iSpecies = argon_plus_ions
    }
```

```
}
Equipotential
{
    name = Cathode_and_limiters
    C = -200
    A = 0
    a0 = 1
    a1 = 1
    tdelay = 1
    phase = 0

    Segment
    {
        name = Just_cathode
        j1 = 0
        k1 = 0
        j2 = Zcells
        k2 = 0
        normal = 1
    }
            Segment
    {
        name = Left_limiter
        j1 = 0
        k1 = 0
```

```
            j2 = 0

            k2 = Rcells*0.9

            normal = 1

        }

        Secondary

        {

            secondary = 0.2

            secSpecies = electrons

            iSpecies = argon_plus_ions

        }

        nxbins=30

        nenergybins = 30

        energy_min = 0

        energy_max = 500

    }

    Dielectric

    {

        name = Teflon_limiter

        er = 1.0

        Segment

        {

            name = Left_teflon

            j1 = 0

            k1 = Rcells*0.9

            j2 = 0
```

```
        k2 = Rcells
        normal = 1
    }
    Secondary
    {
        secondary = 0.3
        secSpecies = electrons
        iSpecies = argon_plus_ions
    }
}
Load
{
    x1MinMKS = -z_max/2
    x1MaxMKS = 0.0
    x2MinMKS = r_min
    x2MaxMKS = r_max
    speciesName = electrons
    analyticF = ramp((-1.39264E18+5.69607E20*x2-8.53703E22*x2^2
    +6.47744E24*x2^3-2.67462E26*x2^4+5.72779E27*x2^5-4.97915E28
    *x2^6)*(1.00704-1.0428*x1-408.38346*x1^2-14527.79234*x1^3
    -26451.7345*x1^4+3.16456E6*x1^5))
    np2c = 0.5e6
    units=EV
    temperature = 5
}
```

```
    Load
    {
        x1MinMKS = -z_max/2
        x1MaxMKS = 0.0
        x2MinMKS = r_min
        x2MaxMKS = r_max
        speciesName = argon_plus_ions
        np2c = 0.5e6
        analyticF = ramp((-1.39264E18+5.69607E20*x2-8.53703E22*x2^2
        +6.47744E24*x2^3-2.67462E26*x2^4+5.72779E27*x2^5-4.97915E28
        *x2^6)*(1.00704-1.0428*x1-408.38346*x1^2-14527.79234*x1^3
        -26451.7345*x1^4+3.16456E6*x1^5))
        units=EV
        temperature =  300*kb/e0

    }
}
```

# Appendix C

# List of publications

## C.1 Publications in scientific journals

[1] Trunec D., Holík M., Kudrna P., Bilyk O., Marek A., Hippler R., Tichý M., Monte Carlo simulations of the electron currents collected by electrostatic probes, Contributions to Plasma Physics, **44**, 577-581, 2004.

[2] Holík M., Bilyk O., Marek A., Kudrna P., Behnke J.F., Tichý M., 2-D Experimental study of the plasma parameter variations of the magnetically sustained DC discharge in cylindrical symmetry in Argon, Contributions to Plasma Physics, **44**, 613-618, 2004.

[3] Bilyk O., Kudrna P., Holík M., Marek A., Tichý M., Behnke J.F., A study of discharge fluctuations in magnetically-supported dc discharge in cylindrical and inverted cylindrical configuration, Czechoslovak Journal of Physics, Suppl. C, **54**, C735-C741, 2004.

[4] Bilyk O., Holík M., Marek A., Kudrna P., Tichý M., Behnke J.F., Fluctuations of the magnetically-supported dc discharge in coaxial configuration, Vacuum, **76**, 437-445, 2004.

[5] Marek A., Kudrna P., Holík M., Bilyk O., Picková I., Tichý M., Apetrei R. P., 2D PIC simulation of dc magnetized plasma in cylindrical configuration, Acta Physica Slovaca, **55**, 461-466, 2005.

[6] Bilyk O., Holík M., Kudrna P., Marek A., Tichý M., Observation of Wave-like Structures in Magnetized dc Discharge in Cylindrical Symmetry in Argon, Contributions to Plasma Physics, **46**, 361-366, 2006.

[7] Marek A., Picková I., Kudrna P., Tichý M., Apetrei R. P., Olenici S. B., Gstrein R., Schrittwieser R., Ionita I., Experimental Investigation of the Change of the Electron Saturation Current of a dc-heated Emissive Probe, Czechoslovak Journal of Physics, Suppl B, **56**, B932-B937, 2006.

[8] Picková I., Marek A., Tichý M., Kudrna P., Apetrei R. P., Measurements with the Emissive Probe in the Cylindrical Magnetron, Czechoslovak Journal of Physics, Suppl B, **56**, B1002-B1008, 2006.

## C.2 Publications in conference proceedings

[1] Bilyk O., Kudrna P., Holík M., Marek A. and Tichý M., A study of DC discharge instability in cylindrical magnetron, WDS'02 Proceedings of Contributed Papers: Part II - Physics of Plasmas and Ionized Media (ed. J. Šafránková), Prague, Matfyzpress, 388-393, 2002.

[2] Bilyk O., Holík M., Marek A., Kudrna P., Tichý M., A study of the floating potential fluctuations in the cylindrical magnetron DC discharge plasma, WDS'03 Proceedings of Contributed Papers: Part II - Physics of Plasmas and Ionized Media (ed. J. Šafránková), Prague, Matfyzpress, 460-465, 2003.

[3] Holík M., Kudrna P., Bilyk O., Marek A., Tichý M., Trunec D., Behnke J. F., Probe diagnostic of DC discharge in cylindrical magnetron - Experiment and Monte Carlo simulation, WDS'03 Proceedings of Contributed Papers: Part II - Physics of Plasmas and Ionized Media (ed. J. Šafránková), Prague, Matfyzpress, 456-459, 2003.

[4] Holík M., Bilyk O., Marek A., Kudrna P., Behnke J.F., Porokhova I.A., Golubovskii Yu.B., Tichý M., 2-D experimental study of the plasma parameter variations of the magnetically sustained dc discharge in cylindrical symmetry in argon Proc. XXVI ICPIG, Vol. 1 (ed. by J. Meichsner, D. Loffhagen, H.E. Wagner), Greifswald, Germany, 43-44, 2003.

[5] Kudrna P., Holík M., Bilyk O., Marek A., Behnke J.F., Martines E., Tichý M., Langmuir probe study of the floating potential fluctuations in the dc cylindrical magnetron discharge, Proc. XXVI ICPIG, Vol. 4 (ed. by J. Meichsner, D. Loffhagen, H.E. Wagner), Greifswald, Germany, 157-158, 2003.

[6] Kudrna P., Holík M., Bilyk O., Marek A., Behnke J.F., Martines E., Tichý M., A study of fluctuations in the dc cylindrical magnetron discharge using Langmuir probes, Proc. 16th Intern. Symposium on Plasma Chemistry, Abstracts and full-papers CD, CD - ISPC-583.pdf, 1-6, 2003.

[7] Marek A., Kudrna P., Holík M., Bilyk O., Tichý M., The PIC Simulation of the Magnetized DC Discharge Plasma in the Cylindrical Configuration, WDS'04 Proceedings of Contributed Papers: Part II - Physics of Plasmas and Ionized Media (ed. J. Šafránková), Prague, Matfyzpress, 316-321, 2004.

[8] Holík M., Bilyk O., Marek A., Kudrna P., Behnke J. F., Tichý M., Study of Magnetically Supported DC Discharge in Cylindrical Configuration, WDS'04 Proceedings of Contributed Papers: Part II - Physics of Plasmas and Ionized Media (ed. J. Šafránková), Prague, Matfyzpress, 322-326, 2004.

[9] Bilyk O., Kudrna P., Holík M., Marek A., Tichý M., Behnke J. F., Fluctuation of dc discharge in EB field in cylindrical configuration, WDS'04 Proceedings of Contributed Papers: Part II - Physics of Plasmas and Ionized Media (ed. J. Šafránková), Prague, Matfyzpress, 327-332, 2004.

[10] Holík M., Bilyk O., Marek A., Kudrna P., Behnke J.F., Tichý M., Axial distribution of Discharge Current in Magnetically Supported DC Discharge in Cylindrical Configuration in Helium, Neon and Argon, Proc. XVII ESCAMPIG (ed. V. Ciupina, G. Musa, R. Vladoiu), Constanta, Rumania, 177-178, 2004.

[11] Bilyk O., Kudrna P., Holík M., Marek A., Tichý M., A study of magnetically-supported dc discharge in cylindrical and inverted cylindrical configuration, Proceedings of the 12th International Congress on Plasma Physics, (ed. by T. Hutter), http://hal.ccsd.cnrs.fr/ccsd-00002041, Nice, France, 1-7, 2004.

[12] Holík M., Picková I., Bilyk O., Marek A., Kudrna P., Behnke J. F., Tichý M., Modelling and emissive probe measurements in magnetically supported dc discharge in cylindrical configuration, Plasma Polymers and Related Materials, (ed. M. Mutlu, G. Dinescu, R. Frch, J.M. Martin-Martinez, J. Vyskocil), Hacettepe University Press 2005, ISBN 975-491-194-0, 136-141, 2005.

[13] Marek A., Kudrna P., Holík M., Bilyk O., Tichý M., 2D PIC Simulation of dc Magnetized Plasma in Cylindrical Configuration, Book of Contributed Papers SAPP XV, January 15-20, Podbánské, Slovakia, 209-210, 2005.

[14] Marek A., Kudrna P., Picková I., Holík M., Bilyk O., Tichý M., 2D PIC Simulations of the DC Discharge in Cylindrical Magnetron, WDS'05 Proceedings of Contributed Papers: Part II - Physics of Plasmas and Ionized Media (ed. J. Šafránková), Prague, Matfyzpress, 362-367, 2005.

[15] Marek A., Holík M., Bilyk O., Picková I., Apetrei R. P., Schrittwieser R., Ionita-Schrittwieser C., Kudrna P., Tichý M., Magnetized Plasma in Cylindrical Coordinates - Experiment and Model, 17th Intern. Symposium on Plasma Chemistry, Abstracts and full-papers CD, abstract p.197, CD - ISPC-635.pdf, 1-4, 2005.

[16] Marek A., Apetrei R. P., Olenici S. B., Gstrein R., Picková I., Kudrna P., Tichý M., Schrittwieser R., Emissive Probe Measurements in the DC Low Temperature Magnetized Plasma in Cylindrical Configuration, ICPP'06 Proceedings contributed papers CD, paper A168, CD - A168p.pdf, 1-4, 2006.

[17] Gstrein R., Marek A., Ionita C., Kudrna P., Olenici S. B., Balan P. C., Schrittwieser R., Tichý M., Space Charge Effects Of Emissive Probes Investigated In A DP-Machine, ICPP'06 Proceedings contributed papers CD, paper A181, CD - A181p.pdf, 1-4, 2006.

[18] Marek A., Kudrna P., Komm M., Picková I., Tichý M., Progress in PIC Simulation of the dc Argon Discharge in Cylindrical Magnetron, WDS'06 Proceedings of contributed papers, (ed. J. Šafránková), Prague, Matfyzpress, 133-138, 2006.

[19] Marek A., Apetrei R. P., Picková I., Kudrna P., Tichý M., Schrittwieser R., Ionita C., Can a Strongly Emitting Probe be Used in a Low Temperature Plasma?, Book Abstracts SAPP XVI, January 20-25, Podbánské, Slovakia, 225-226, 2007.

# Appendix D

# Attached articles

Marek A., Kudrna P., Holík M., Bilyk O., Tichý M., The PIC Simulation of the Magnetized DC Discharge Plasma in the Cylindrical Configuration, WDS'04 Proceedings of Contributed Papers: Part II - Physics of Plasmas and Ionized Media (ed. J. Šafránková), Prague, Matfyzpress, 316-321, 2004.

# The PIC Simulation of the Magnetized DC Discharge Plasma in the Cylindrical Configuration

A. Marek, P. Kudrna, M. Holík, O. Bilyk and M.Tichý

Charles University, Faculty of Mathematics and Physics, Prague, Czech Republic.

**Abstract.** In this article we report on the 2D Particle-In-Cell simulations of the magnetized DC discharge plasma in the cylindrical configuration, particularly on the model of a discharge in our experimental device - cylindrical magnetron. For our PIC simulations we used the XOOPIC code, which was developed at the University of Berkeley. The first results of the 2D simulation for the conventional cylindrical magnetron arrangement (e.g. exterior electrode is the anode and post in the axis serves as the cathode) are presented here and also compared with the experiment.

## Introduction

Numerical simulations are nowadays widely used in plasma physics research. They enable investigation of plasma in various configurations and under different conditions help to understand the plasma behavior. Computational physics is becoming more and more reasonable partner of experimental methods. (But all computations need every time comparison with reality – with experiment.)

Plasma modelling techniques can be divided into two basic families with respect to the plasma description: codes using kinetic description and codes using fluid description of plasma. The technique of our interest – Particle-In-Cell (PIC) technique [e.g. *Birdsall et al.*, 1995] – belongs among codes using kinetic description of plasma. In PIC technique there are solved equations of motion for all charged particles in plasma. Computation of mutual electrical forces is in the PIC approach transformed to the solving of Poisson equation in the simulated region. A great advantage of this technique is that it is self-consistent. On the other hand self-consistent approach is compensated by great computational effort (especially in 2D and 3D simulations).

Let us describe the electrostatic Particle-In-Cell computational scheme: 1.) Division of simulated region to cells – 2.) Assignment of the charge of particles to the mesh points – 3.) Computation of the electrical field (via solution of the Poisson equation on the mesh points) – 4.) Particle move in fields (solution equations of motion in computed electric and in applied external magnetic field) – 5.) Jump to the point 2.

Collisions with neutral particles (elastic collisions, excitation, ionization) are in PIC codes usually realized via Monte Carlo – Null Collision method [*Skullerud*, 1968].

Although electromagnetic PIC scheme, which involves also magnetic field induced by moving charged particles, is also possible, it is not needed for the case of our study. We focus in our work on simulations of the dc discharge in cylindrical magnetron, where magnetic field induced by moving charged particles can be neglected in comparison with the applied external magnetic field because of the small current density in the cylindrical magnetron.

## Cylindrical magnetron – object of computations

An experimental device – cylindrical magnetron – is currently used in our laboratory for a study of the influence of the magnetic field on the discharge characteristics and on the plasma diagnostic (particularly on the diagnostic via Langmuir probe). Magnetron is suitable for such a study because of the simple arrangement of the magnetic field, which is parallel to the axis of the magnetron and can vary its magnitude. The numerical model of magnetron discharge can help to determine ”true values” of plasma parameters in discharge. They can be compared with those determined from experimental Langmuir probe characteristic by employing different probe theories.

The scheme of the cylindrical magnetron is depicted in figure 1 and is described in detail in [*Passoth et al.*, 1997]. Cylindrical magnetron consists of grounded cylindrical steel vacuum vessel which serves as the anode and the post on the axis of vessel which serves as the cathode. Discharge region is delimited by two limiters which are connected to the cathode potential. The cathode is water cooled. Discharge in the magnetron is confined by the magnetic field parallel to the magnetron axis. Magnetic field is created by the couple of coils and can vary up to the magnitude of 40 mT. The discharge region in magnetron has 12 cm in length and 6 cm in diameter. Our magnetron operates in rare gases at pressures typically 1 − 10 Pa and up to 200 mA of discharge current.

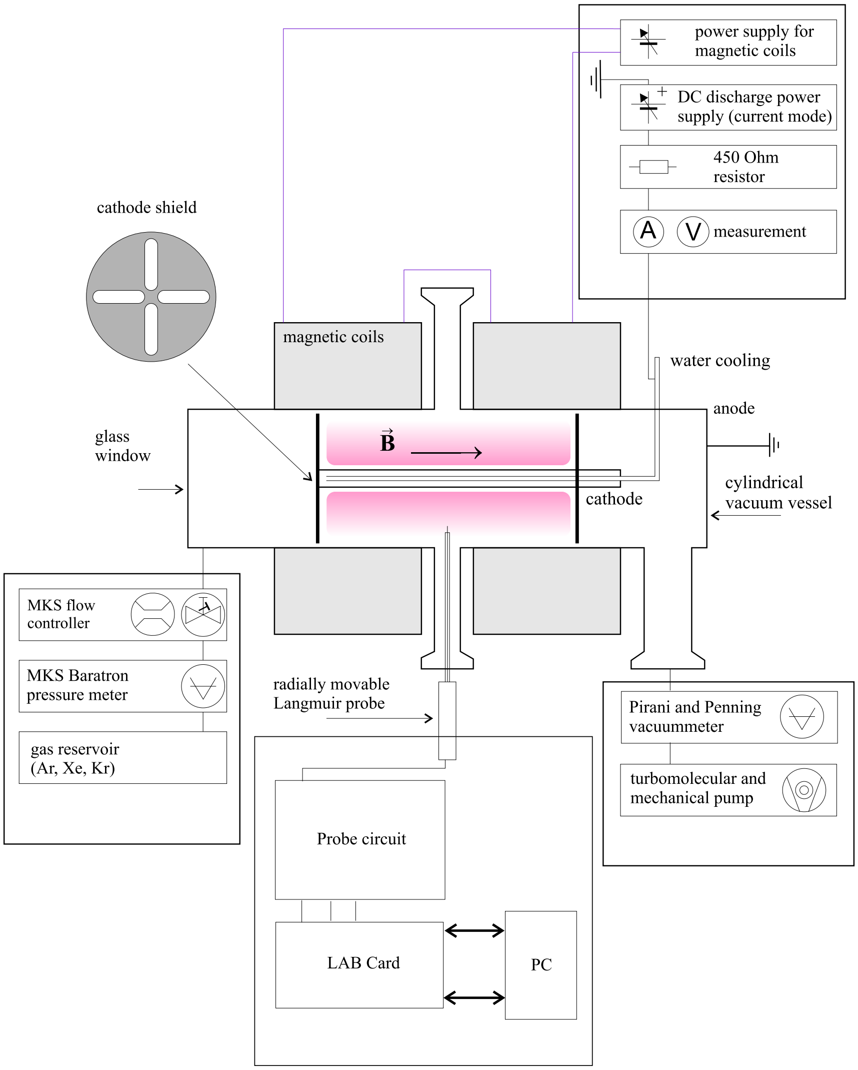

**Figure 1.** Scheme of cylindrical magnetron, Faculty of Mathematics and Physics , Charles University, Prague.

## PIC model of cylindrical magnetron

For simulations we used the two dimensional XWindow Object Oriented PIC code (XOOPIC) developed at University of California, Berkeley, USA [*Verboncoeur et al.*, 1995].

2D simulation requires great computational power. In order to reduce this, only one half of the magnetron is simulated. It is achieved via dielectric boundary with 100% reflection in the central plane of magnetron. It is possible because of symmetry of the problem.

Scheme of the computational region for simulation is depicted in figure 2. Discharge area is from the left side delimited by the metallic limiter conductively connected with the cathode and isolated by the thin dielectric from the anode. Right margin is built up by the mirror boundary in the center plane of the magnetron. Dimensions of the discharge area are identical in PIC model with those in the real device (anode diameter: 60 mm, cathode diameter: 10 mm, magnetron length: 120 mm (i.e. 60 mm of length is simulated)). Zero in axial direction is placed in the center of the magnetron. Electrostatic field solver is used in the simulation because magnetic field induced by motion of charged particles can be neglected in comparison with applied extern magnetic field. There were taken into account elastic collisions, excitation and ionization for electrons and elastic collisions and charge transfer for ions in simulation.

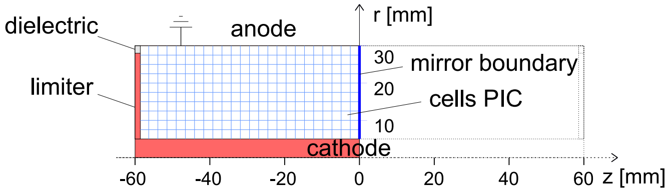

**Figure 2.** Scheme of the region of PIC simulations. Only half of the magnetron is modelled. This is possible due to symmetry of the problem.

## Results of PIC simulation

An example of XOOPIC simulation results of dc discharge in magnetron are presented in figure 3. Simulation was made at following discharge conditions: discharge in Argon at $p = 5$ Pa, $B = 20$ mT and cathode voltage $U_C = -200$ V. Simulation was initialized with uniform distribution of particles in the whole magnetron space in order to obtain initial density profile for further magnetron discharge simulations. Data presented in figure 3 are from snapshot taken at simulation time $t = 5$ µs.

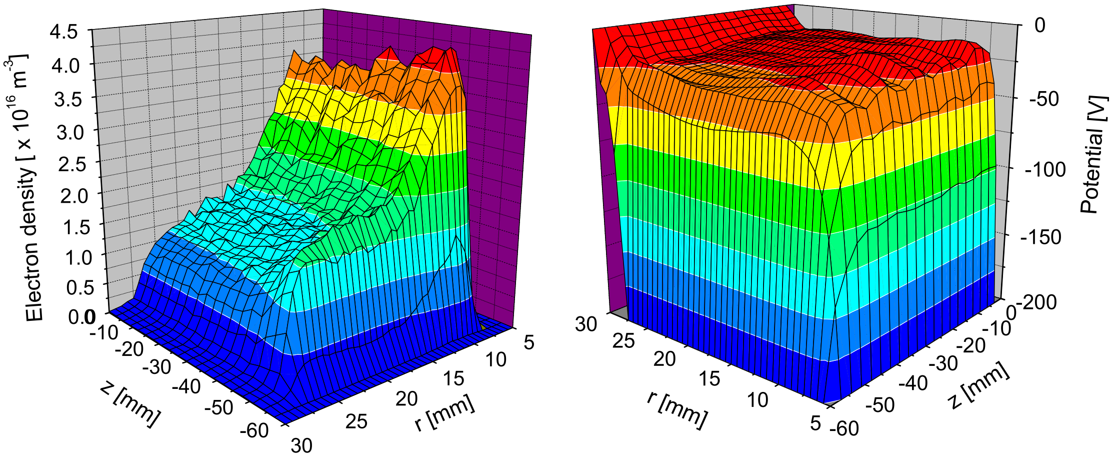

(a) Electron density profile

(b) Potential profile

**Figure 3.** Electron density and potential profile computed in simulation of dc discharge in Argon at $p = 5$ Pa, $B = 20$ mT and cathode voltage $U_C = -200$ V.

The anode in figure 3(a) is situated on the left front margin of the chart at radial coordinate $r =$ 30 mm, the cathode is at $r = 5$ mm. Zero of axial coordinate denotes center of the magnetron. Therefore the limiter is situated on the right front margin of the chart at $z = -60$ mm. In order to get a better view figure 3(b) with potential profile is rotated clockwise by 90°.

In figure 3(b), you can see the profile of the potential which comes up to our expectations – high cathode fall near the cathode and the limiter, almost constant potential profile in central part of magnetron (positive column) and moderate anode fall in the vicinity of the grounded anode in the back left margin of the chart. Such potential profile is typical for glow discharges. Electron density profile depicted in figure 3(a) is also qualitatively good. Only formation of a peak on the ridge of density profile in the limiter vicinity is the sign of computational instability.

## Comparison with experiment

Though 2D experimental map of density profile is not available in magnetron described above we can compare our computational results with radial density profiles in the central plane of our magnetron obtained via Langmuir probe. We can also qualitatively compare our results with experimental data measured in another cylindrical magnetron (till 2004 situated at E-M-A University in Greifswald, Germany, now at Charles University in Prague, Czech republic), which differs from that depicted in figure

1 by longer discharge region (30 cm instead of 12 cm) and by another cathode diameter (18 mm instead of 10 mm) but enables measurements of radial profiles at different radial positions. Let us denote this magnetron as the 'longer' magnetron.

In figure 4 the computed radial electron density profile in central plane of the magnetron ($z = 0$ mm) is compared with experimental data measured by Langumir probe. Radius $r_A$ in charts denotes the position of anode.

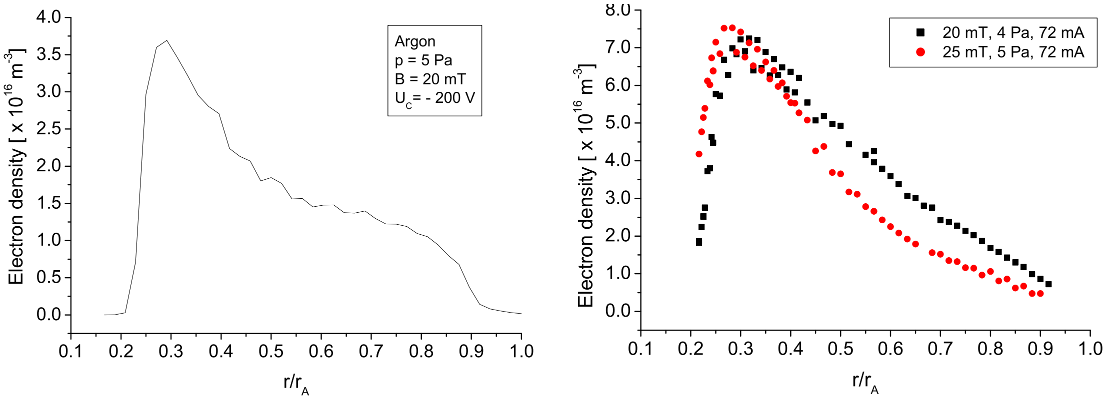

(a) PIC model

(b) Experiment

**Figure 4.** Electron density profile in central plane of the magnetron. Comparison of computational results with experiment.

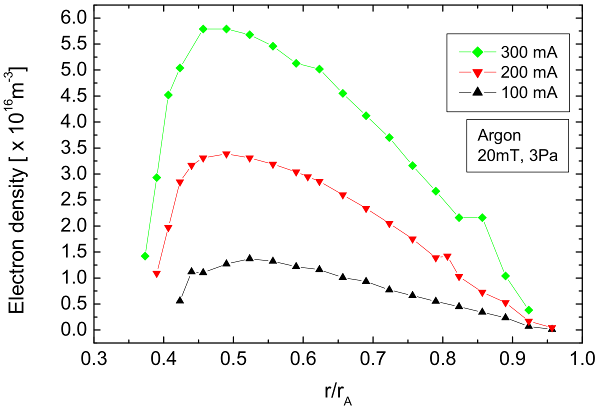

**Figure 5.** Dependence of the measured radial profile of electron density on the discharge current.

In figure 4 we can see qualitatively good agreement between simulation results and experimental values. The shape of experimental density profiles is comparable with that from simulation and maximum electron density is observed at the same radial position in both cases. The main difference is in magnitude of electron density. In our simulation the two times lower values were obtained. The discrepancy can be connected with the dependence of density on the discharge current. This relation is illustrated in figure 5 where density profiles measured in 'longer' magnetron are depicted for several discharge currents. The discharge current was not recorded in our simulation so we are not able to compare it with experimental value.

The axial density profile can be compared with experimental values only roughly. Radial profiles of electron density measured at three different axial positions in 'longer' magnetron are presented for several magnitudes of magnetic field in figure 6. To the conditions used in our simulation ( $\frac{B}{p} = 4$ mT/Pa) corresponds the best the first chart where $\frac{B}{p} = 3.3$ mT/Pa.

## Problem in the simulation – rising number of computational particles

Although results of XOOPIC simulation presented here are in relatively good agreement with the experiment there is a problem with numerical instability of the simulation – with a growing number of computational particles during simulation. An example of the time evolution of the number of computational particles in our simulation is depicted in figure 7(a). You can see rapid growth of their number since 6 µs with strange progress after 8 µs.

Similar behavior is presented in figure 7(b) where the time histories of the number of computational particles in the XOOPIC simulation of the voltage driven unmagnetized dc discharge made by J.Hammel at the University of California in Berkeley are depicted. The discharge configuration was in this case

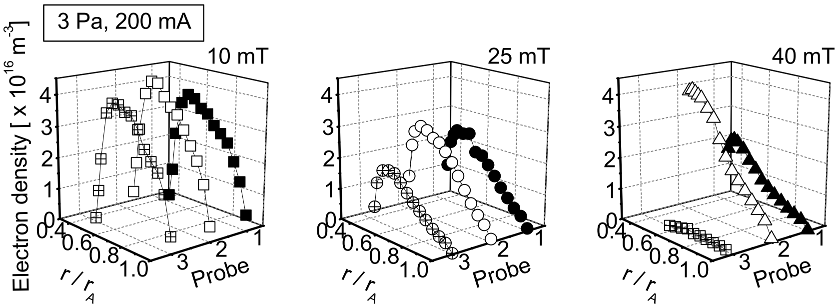

**Figure 6.** Radial electron density profiles measured in the 'longer' magnetron on three different axial positions : $1 - z = 0$ mm(central plane), $2 - z = 60$ mm, $3 - z = 120$ mm. Limiter position is $z = 150$ mm [*Holík et al.*, 2003].

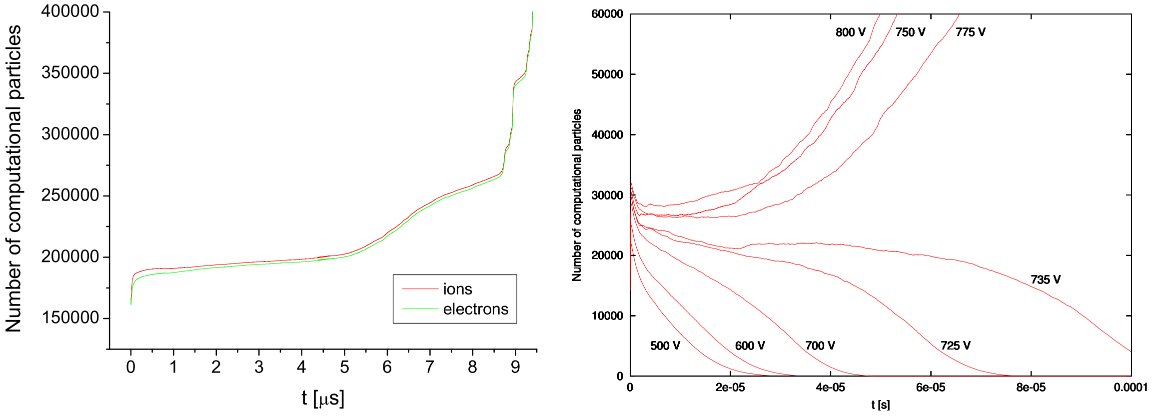

(a) The time evolution of the number of computational particles in our simulation of the dc discharge in cylindrical magnetron.

(b) Voltage driven XOOPIC runs in unmagnetized dc discharge (J.Hammel – University of California, Berkeley, USA).

**Figure 7.** The time evolution of the number of computational particles during simulation for our instance and its comparison with voltage driven XOOPIC runs in unmagnetized dc discharge done by J.Hammel at University of California, Berkeley, USA [*Hammel et al.*, 2004].

different (two planar electrodes in dielectric cylindrical tube, discharge without magnetic field) but his results demonstrates well behavior of the glow discharge driven by the voltage source. You can see that it is practically impossible to set the proper discharge voltage to obtain the stable discharge solution in the model. Only a small difference in applied voltage causes the fatal discrepancy of the discharge behavior in the future. In experimental practice this problem (which is caused by positive voltage feedback of the discharge) is solved by incorporating a resistor into the discharge circuit or by usage of the current source instead of the voltage source.

Typical current voltage characteristic of the low pressure unmagnetized dc discharge is presented in figure 8(a). Glow discharges in low pressure gases often operate in the positive voltage feedback region (region C–D) but the current in the discharge system is delimited by resistor.

However, in our cylindrical magnetron the situation is different. From our experiments we know that the magnetron operates in the region with the negative feedback (in the vicinity of the point E in figure 8(a)). Discharge characteristic measured in our magnetron is depicted in figure8(b) for illustration. The negative feedback implies that our magnetron can operate in the constant-current mode as well as in the constant-voltage mode (without the current limiting resistor).

In the XOOPC simulation model the question still remains: How can the simulation reach a stable state? Is the implementation of the current source into the XOOPIC necessary (the current source implementation is not usable yet) or is it possible to reach the steady state with negative voltage-current feedback, which is observed in experiment, in our simulation model in a different way?

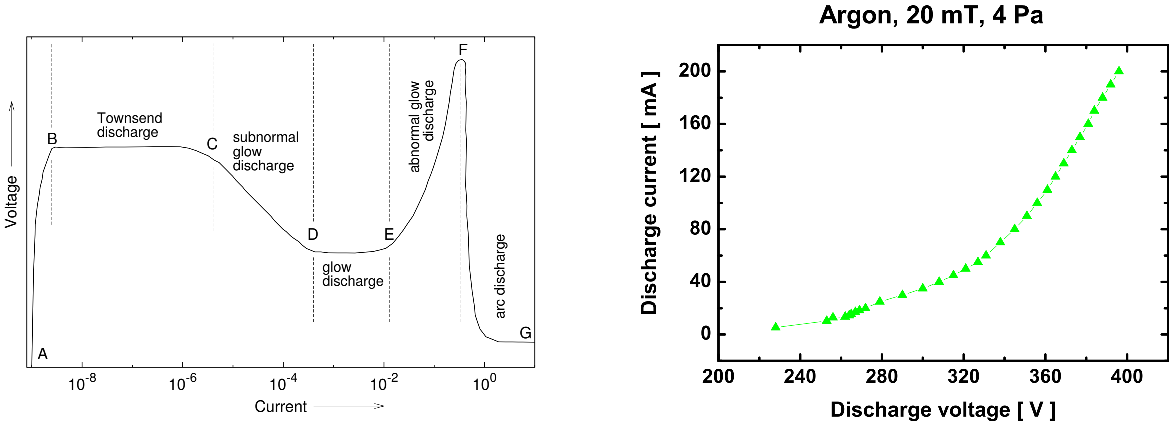

(a) Typical low pressure dc discharge characteristic.

(b) DC discharge characteristic measured in cylindrical magnetron

**Figure 8.** DC discharge characteristic in low pressure gas and its comparison with operational region of dc discharge in cylindrical magnetron.

## Conclusion

We presented here results of our 2D PIC simulations of the dc magnetized discharge in cylindrical configuration, particularly in the cylindrical magnetron device. Simulation was realized by using XOOPIC code developed at the University in Berkeley, USA. Density profile obtained in simulation was qualitatively compared with experimental data measured via Langmuir probe in the cylindrical magnetron partially in laboratory at the Charles university in Prague, Czech republic and partially at the E-M-A University in Grefswald, Germany. Results of the simulation are relatively in good agreement with experimental data.

The computational model, however, needs further improvement because of instability in the number of the simulation particles instability. A current source may be implemented into the code to help to solve this problem. In future work, we hope to bring with our simulation model a more detailed study of the discharge in cylindrical magnetron and more precise comparison with experiment.

**Acknowledgments.** The work in Greifswald was financially supported by the Deutsche Forschungs-Gemeinschaft (DFG) in frame of the project SFB 198 Greifswald "Kinetik partiell ionisierter Plasmen". The work in Prague was partially financially supported by the Czech Science Foundation, grants 202/03/H162, 202/03/0827 and 202/04/0360, by project COST action 527.70 and by the Faculty of Mathematics and Physics, Research plan MSM 1132000002. The authors are indebted to Institute of Physics, University of Greifswald, for the loan of the experimental equipment.

## References

Birdsall, C.K., A.B. Langdon, Plasma physics via computer simulation, *Mc Graw-Hill* 1995,*Adam-Hilger* 1991.

Skullerud H. R., The stochastic computer simulation of ion motion in a gas subjected to a constant electric field, *J. Phys. D: Appl. Phys.*, 1, 1567-1568, 1968.

Hammel, J., J. Verboncoeur, DC Discharge studies using PIC-MCC, http://ptsg.eecs.berkeley.edu/j̃hammel/report.pdf, 2004.

Holík M., O. Bilyk, A. Marek, P. Kudrna, J.F. Behnke, I.A. Porokhova, Yu.B. Golubovskii, M. Tichý, 2-D experimental study of the plasma parameter variations of the magnetically sustained dc discharge in cylindrical symmetry in argon, *Proc. XXVI ICPIG, Vol. 1 (ed. by J. Meichsner, D. Loffhagen, H.E. Wagner), Greifswald, Germany*, 43-44, 2003.

Passoth, E., P. Kudrna, C. Csambal, J.F. Behnke, M. Tichý and V. Helbig, An experimental study of plasma density determination by a cylindrical Langmuir probe at different pressures and magnetic fields in a cylindrical magnetron discharge in heavy rare gases, *J. Phys. D: Appl. Phys*, 30, 1763-1777, 1997.

Verboncoeur,J.P., A.B. Langdon and N.T. Gladd, An Object-Oriented Electromagnetic PIC Code,*Comp. Phys. Comm.*, 87, 199-211, May11, 1995.

MAREK A., KUDRNA P., HOLÍK M., BILYK O., PICKOVÁ I., TICHÝ M., APETREI R. P., 2D PIC simulation of dc magnetized plasma in cylindrical configuration, Acta Physica Slovaca, **55**, 461-466, 2005.

**acta physica slovaca vol. 55 No. 5, 461 – 466 October 2005**

# 2D PARTICLE-IN-CELL SIMULATION OF DC MAGNETIZED PLASMA IN CYLINDRICAL CONFIGURATION[1]

**A. Marek[2]*, P. Kudrna*, M. Holík*, O. Bilyk*, I. Picková*, M. Tichý*, R.P. Apetrei†**
**Charles University in Prague, Faculty of Mathematics and Physics,*
*V Holešovičkách 2, 180 00 Prague 8, Czech Republic*
†*Innsbruck University, Institut for Ion Physic, A-6020 Innsbruck, Austria*

Received 18 April 2005, in final form 27 May 2005, accepted 31 May 2005

We report on 2D Particle-In-Cell (PIC) simulations of dc magnetized plasma in cylindrical coordinates. Simulations aremade by XOOPIC code developed on the University of California, Berkeley. Results of the simulation are compared with experimental data obtained by Langmuir probe and emissive probe diagnostics in cylindrical magnetron device.

PACS: 52.65.Rr, 52.70.Ds, 52.25.Xz, 52.50.Dg

## 1 Introduction

PIC method of plasma simulation is widely used in plasma physics research because of its reasonable results and ability to solve wide range of problems in its kinetic approach. Regarding to description of PIC method we refer to [1]. We present here 2D PIC simulations of magnetized dc discharge in cylindrical magnetron device. Magnetrons are used in industry e.g. for thin film layer coating and etching. Many magnetron configurations are used. In our research we concern on discharge in the cylindrical magnetron device because its symmetry and simple magnetic field arrangement enables relatively simple theoretical description and makes easier understanding of processes in weakly magnetized plasma avoiding effects of nonhomogenous magnetic field. We study the influence of the magnetic field on discharge parameters and PIC model of discharge can contribute to our description.

## 2 Experimental system

Scheme of the cylindrical magnetron device used for experimental research in our laboratory is depicted in Fig. 1 and is described in detail in [2] so that only its overview will be given at this place: Cylindrical magnetron consists of grounded stainless steel tube (anode) and water cooled cathode at its axis. Discharge area (12 cm long) is constrained by two metallic limiters connected

---

[1] Presented at Joint 15th Symposium on Applications of Plasma Processes (SAPP) and 3rd EU-Japan Symposium on Plasma Processing, Podbanské (Slovakia), 15 – 20 January 2005.

[2] E-mail address: Ales.Marek@matfyz.cz

0323-0465/05 © Institute of Physics, SAS, Bratislava, Slovakia

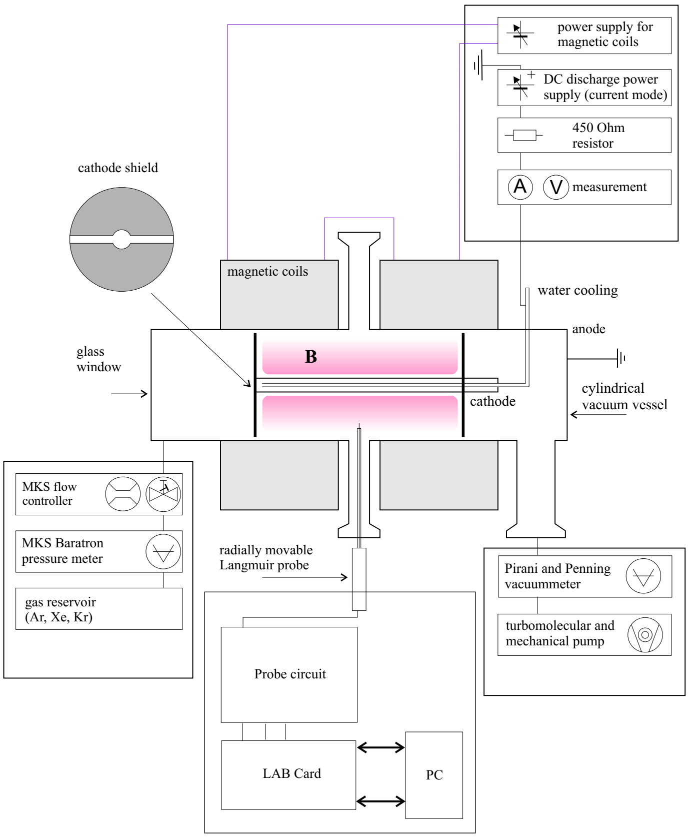

Fig. 1. Cylindrical magnetron scheme. Faculty of Mathematics and Physics, Charles University in Prague.

to the cathode potential. Plasma in magnetron is confined by homogenous magnetic field parallel to axis. It is created by couple of magnetic coils and can vary up to $40\ \mathrm{mT}$. Magnetron usually operates in noble gases at pressures $1\ -10\ \mathrm{Pa}$. Plasma parameters can be determined by means of electrical probes placed in vacuum feedthrough in the central plane of magnetron. Some experimental data presented in this contribution are obtained in similar cylindrical magnetron (see e.g. [3]) that differs from that one described here in length of discharge area ($30\ \mathrm{cm}$ instead of $12\ \mathrm{cm}$) and also in electrodes radii (anode radius is $28\ \mathrm{mm}$ and cathode radius is $9\ \mathrm{mm}$). Let us to denote these two magnetrons like ”longer” and ”shorter” magnetron for easier handling in this text. Shorter magnetron’s dimensions are given in Fig. 2 .

## 3 2D PIC model of the magnetron

For simulations we applied XOOPIC code [4] developed on the University of California, Berkeley. Scheme of region for our 2D PIC model of discharge in cylindrical magnetron is depicted

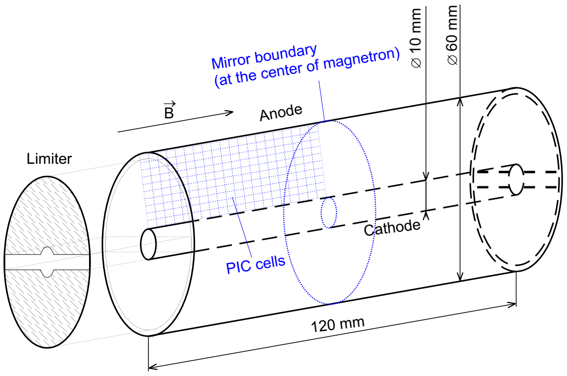

Fig. 2. : Scheme of region for 2D PIC simulation of discharge in the "shorter" magnetron.

in Fig. 2. 2D code is suitable for this problem because of symmetry of magnetron arrangement. Symmetry could enable in principle even 1D description, but we know from experiment, that discharge is not homogenously distributed along the whole discharge region. In order to reduce computational effort we placed reflecting boundary to the middle of magnetron and we simulated only half of discharge area (from the center to the left limiter). However, simulation remained still relatively time consuming. This is because conditions had to be fulfilled that ensure stable and physically correct solution. According to [5] it means: 1.) cell length smaller or comparable with Debye length (that is in the order of tens of $\mu\mathrm{m}$ in magnetron), 2.) reasonable number of simulating superparticles in cell (optimally 10 to 50 per cell – this was not fulfilled in our simulation because of too high computational requirements) and 3.) time step restrictions: time step must resolve processes on plasma frequency and particles need not fly over more than one cell in one time step.

## 4 Results of model and comparison with experiment

An example of computational results is presented in figure 3. It is obtained in simulation where cells dimensions were comparable with Debye length. Comparison of computational electron density results with Langmuir probe data is given in Fig. 4 for two different experimental conditions; $r_A$ denotes anode radius. Considering that maximum of the electron density is proportional to the applied power we can see satisfactory agreement of model results with experimental data. Maximum of computed electron density is situated approximately at the same position like in experiment. Profile of the electron density in the region of positive column corresponds better to Langmuir probe data obtained at higher magnetic field ($25\ \mathrm{mT}$, $5\ \mathrm{Pa}$ – note the ratio of the magnetic induction over pressure remains the same: $B/p = 5\ \mathrm{mT/Pa}$).

An important criterion of physical reliability of our computational results is plasma potential profile (Fig. 3b). The discrepancy in the plasma potential profile in our former 1D model of magnetron [6] was the motivation to apply 2D model. In 1D model dropped more than one half of applied discharge voltage in the anode regions and in the positive column (positive column was not in fact developed at all). This is in contrast with data obtained in discharge by Langmuir

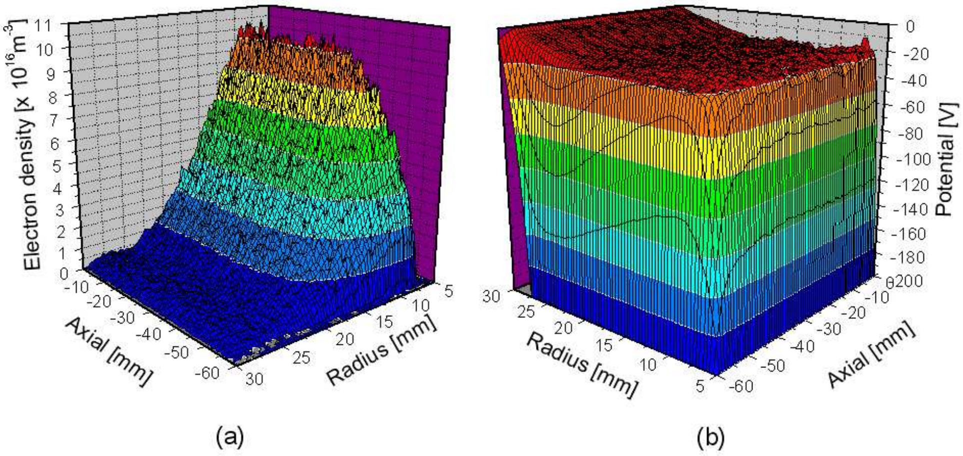

(a) (b)

Fig. 3. XOOPIC simulation results of Argon discharge in magnetron at $p = 4\,\mathrm{Pa}$, $B = 20\,\mathrm{mT}$, $U_{Cathode} = -200\ \mathrm{V}$. Data are from snapshot taken at discharge time $t = 6,4 \times 10^{-7}$ s. Density profile used for initial condition was obtained from former simulation with rougher computational grid. Zero of axial coordinate denotes center of magnetron; $r_{Anode} = 30$ mm; $r_{Cathode} = 5$ mm. Cell dimension is comparable with Debye length (i.e. $500 \times 1250$ cells). (a) electron density profile, (b) potential profile (for better view 90° clockwise rotated).

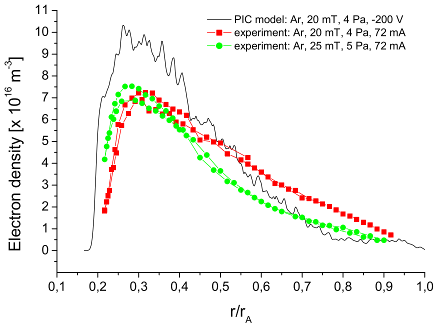

Fig. 4. Comparison of computed radial density profile with data measured by Langmuir probe. $r_A$ is anode diameter.

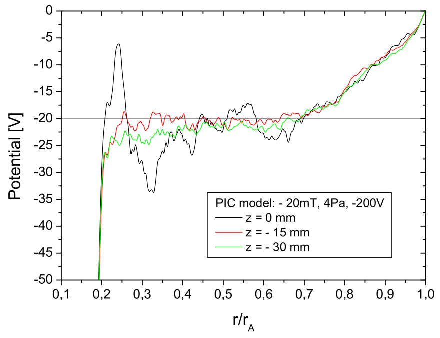

Fig. 5. Detail of computational potential profile at three different axial positions. $r_A$ is anode diameter, $z = 0$ denotes the center of the magnetron.

probe diagnostics. These experimental data showed only small potential fall in anode regions as well as in positive column. Almost the whole applied voltage was spent in cathode regions.

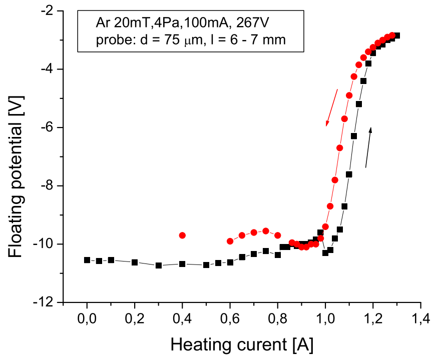

Fig. 6. Heating characteristics of emissive probe. Operating point determined at 1.3 A.

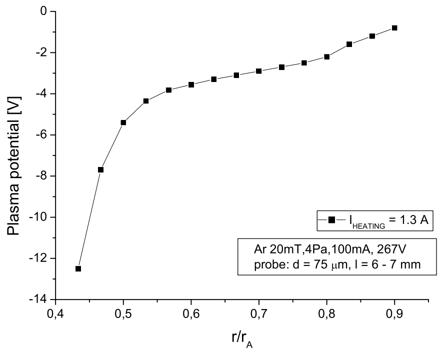

Fig. 7. Radial profile of plasma potential obtained by strongly emitting probe in ”longer” magnetron.

Despite that, electron density profile obtained in 1D model corresponded relatively well with the experiment.

In our former 2D simulations with rougher computational grid presented e.g. in [7] we obtained potential profile that corresponded better with Langmuir probe results than in case of 1D model. Region of positive column is relatively broad and is well developed. But the potential fall in anode regions was almost 40 V (from 200 V of applied voltage) and furthermore number of simulating particles monotonously grew during computation - computation was not stable. The presented simulation was already stable and was made with gird cell size comparable in both directions with Debye length. Resulting plasma potential profile (Fig. 3b) is in detail depicted at three different axial positions in 5. We can see flat and well developed positive column like in simulation [7], but potential profile is better resolved and potential fall in anode regions is smaller.

To compare of potential profile with experiment we used plasma potentials obtained from the zero cross of the second derivative of the Langmuir probe characteristic. In order to validate experimental plasma potential profile by another method we measured plasma potential profile in magnetron by emissive probe too (in fact the potential shifted by $kT_e/e$ is measured [8]). These measurements have been realized in the ”longer” magnetron. Emissive probe data are depicted in Fig. 6 and Fig. 7. From data in Fig. 6 we determined sufficient value of heating current at which the floating potential of the emissive probe was already good approximation of plasma potential (1.3 A at given experimental conditions). Emissive probe data (see Fig. 7) confirmed results obtained by Langmuir probe: potential fall in the region of the positive column was only a few volts as well as the potential fall in the anode regions.

Big potential fall in anode regions in the simulation can be caused by some of these factors: a) grid is not still fine enough, b) discrepancy is observed because of the noise in potential caused by small number of superparticles per one cell, c) model doesn't involve all processes participating in burning discharge. Solution of this discrepancy will be object of our future work.

## 5 Conclusion

We used 2D PIC code for modeling of weakly magnetized dc discharge in the cylindrical magnetron. In our recent simulation with grid comparable with Debye length we obtained stable solution that is in relatively good consistency with experimental results. Despite that qualitative agreement of simulation results with experiment was found, further improvement of model is needed because of relatively big potential fall was observed in anode regions in simulation in comparison to data obtained by emissive as well as Langmuir probe measurements.

**Acknowledgement:** The work was financially supported by Czech Science Foundation, grants 202/03/H162, 202/03/0827 and 202/04/0360, by project COST action 527 and by EURATOM. This work is a part of the research plan MSM 0021620834 that is financed by the Ministry of Education of the Czech Republic. Thanks are also due to University of Greifswald, Germany, which provided us with the cylindrical magnetron system.

## References

[1] C.K. Birdsall, A.B. Langdon: *Plasma physics via computer simulation*, Mc Graw-Hill 1995, Adam-Hilger 1991.

[2] E. Passoth, P. Kudrna, C. Csambal, J.F. Behnke, M. Tichý, V. Helbig: *J. Phys. D: Appl. Phys.* **30** (1997) 1763

[3] M. Holík, O. Bilyk, A. Marek, P. Kudrna, J.F. Behnke, M. Tichý: *Contrib. Plasma Phys.* **44** (2004) 613

[4] J.P. Verboncoeur, A.B. Langdon, N.T. Gladd: *Comp. Phys. Comm.* **87** (1995) 199

[5] V. Vahedi, G. DiPeso, C.K. Birdsall, M.A. Lieberman, T.G. Roghlien: *Plasma Sources Sci. Technol.* **2** (1993) 261

[6] J.F. Behnke, C. Csambal, J. Rusz, P. Kudrna, M. Tichý: *Czech. J. Phys.* **50** (2000) 427

[7] M. Holík, I. Pickova, O. Bilyk, A. Marek, P. Kudrna, J.F. Behnke, M. Tichý: *Plasma Polymers and Related Materials* (in print)

[8] M. Y. Ye, S. Takamura: *Phys. Plasmas* **7** (2000) 3457

Gstrein R., Marek A., Ionita C., Kudrna P., Olenici S. B., Balan P. C., Schrittwieser R., Tichý M., Space Charge Effects Of Emissive Probes Investigated In A DP-Machine, ICPP'06 Proceedings contributed papers CD, paper A181, CD - A181p.pdf, 1-4, 2006.

# Space Charge Effects Of Emissive Probes, Investigated In A DP-Machine

R. Gstrein[1], A. Marek[2], C. Ionita[1], P. Kudrna[2], S.B. Olenici[3],
P.C. Balan[1], R. Schrittwieser[1], M. Tichý[2]

[1]*Institute for Ion Physics and Applied Physics, Leopold-Franzens University of Innsbruck, Technikerstr. 25, A-6020 Innsbruck, Austria*
[2]*Charles University in Prague, Faculty of Mathematics and Physics, V Holešovičkách 2, 18000 Prague, Czech Republic*
[3]*Al. I. Cuza University, Faculty of Physics, 11 Carol I Blvd., RO-700506, Iasi, Romania*

**Abstract.** We report on a systematic investigation of electron-emissive probes in a DP-machine plasma. The rationale are perturbing effects observed with emissive probes in various plasmas and with emissive probes of various designs. These effects might impair the accuracy of emissive probes as diagnostic tools for the direct determination of the plasma potential. The two effects are a deviation of the floating potential of an emissive probe from the plasma potential even for a strongly heated probe and a variation of the electron saturation current with the probe heating. We have therefore tested conventional emissive wire probes with different wire diameters and materials and different loop lengths in the Innsbruck DP-machine.

**Keywords:** Plasma diagnostics, emissive probes, plasma potential, DP-machine, space charges
**PACS:** 52.75.-d, 52.70.-m, 52.70.Ds, 52.80.Tn

## INTRODUCTION

Emissive probes are well-known diagnostic tools for the determination of the plasma potential. The principle is that the probe emits an electron current into the plasma which can be detected as long as the probe voltage is more negative than the plasma potential. In contrast to the conventional cold Langmuir probe this method is insensitive to electrons drifts and beams and does not depend on the electron temperature.

In this contribution we present systematic investigations on the variation of the current-voltage characteristic with the heating current in a DP-machine (Double Plasma Machine). An accompanying paper is devoted to analogous investigations in a magnetron discharge.[1] The rationale of our investigations is related to two observed discrepancies of the emissive probe:

- According to simple theory the floating potential of a sufficiently emitting probe should be identical to the plasma potential. However, often it is observed that even with strong emission the floating potential remains somewhat below the value of the plasma potential as determined from a cold probe current-voltage characteristic (assuming a Maxwellian plasma). This effect seems to be related to a space charge forming around the probe wire even with sufficient electron emission.[2,3]
- Whereas the magnitude of the current on the negative side of the emissive probe characteristic naturally increases due to the electron emission current which superimposes on the ion saturation current, the electron saturation current on the positive side should in principle not be affected by the electron emission. Nevertheless, many investigations frequently do show an increase of the electron saturation current with the heating. Our investigations (also Ref. 1) show that this effect seems to be related to the shape of the probe.

We point out, however, that another recent investigation did not show such effects but that in this case the current-voltage characteristic was claimed to behave strictly according to the text book, i.e., without the above-mentioned perturbing effects.[4]

# EXPERIMENTAL SET-UP

## The Emissive Probe Design

A conventional electron emissive probe, according to our design,[2,5,6] consists of a ceramic or boron nitride tube of a few mm outer diameter and suitable length according to the necessity of the experiment. The tube has at least two bores of around 0,5 mm diameter. Through these bores, a wire of a refractory metal (tungsten, thoriated tungsten or tantalum) with a diameter in the range of 0,05 to 0,2 mm is inserted in such a way that on one side of the tube (at the "hot end") a wire loop of a total length of a few mm is formed. In each of the bores, the W-wire extends a few cm towards the other end (the "cold end") of the ceramic tube. Before insertion, the two ends of the wire are spliced equally with about 8 – 10 copper threads with diameters of 0,05 mm on a few cm length so that in the centre a piece of the desired loop length remains uncovered. In this way, inside the bores the two ends of the probe wire are densely covered with a thin layer of Cu so that the conductivity of these parts is larger.

If the wrapping of the W-wires with Cu-threads is performed in the right way the electrical and mechanical contact between the probe wire and the copper is excellent. By careful choice of the number of Cu-threads for wrapping the wire, the thickness of the combined wire ends can be adjusted so that it tightly fits into the bores of the probe tube. This increases the electric and mechanical contact. On the cold end of each tube, only the twisted Cu-wires are protruding and can there be connected easily to any further electrical leads and eventually to a battery or power supply. This treatment has the effect that only the exposed loop of the emissive probe is heated when a current is passed through the probe wire. Compared to other constructions our design is much less bulky and thus such a probe can be constructed very small. See Fig. 1 for a schematic of our probe construction. Our group was the first to use such probes even in fusion experiments,[2,6,7,8,9] where we also found the two effects described in the Introduction.[2]

We have tested emissive probes with three different total lengths of the probe wire loop (5 mm, 10 mm and 20 mm), various wire diameters and the three above mentioned materials (W, W with 0,6% Th, and Ta) in the unmagnetized Ar plasma of the Innsbruck DP-machine.

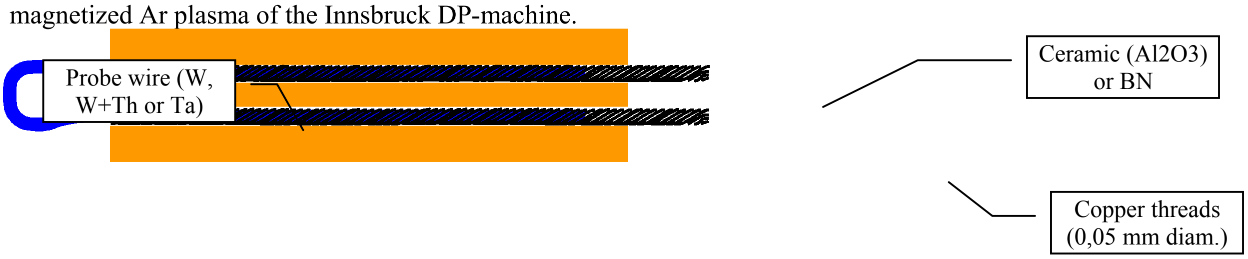

**FIGURE 1.** Schematic of the probe construction. Inside the ceramic the probe wire is spliced with thin copper wires. The connection between the two materials is very tight and provides an excellent mechanical and electrical contact. The covering of the probe wire with copper threads is denser than shown here for clarity.

Great care has to be taken to make meaningful measurements with emissive probes. They are more complicated to handle than cold probes and are much more sensitive to external influences. A conventional emissive wire probe as described here obviously can quickly melt when it is overheated. Therefore also the available emission current, which in turn depends on the plasma density and temperature, is limited. Already before melting, the wire diameter diminishes which leads to an increase of the electric resistance and thereby of the heating power and the emission, if no special measures are taken. The reduction of the diameter of the wire might also have other effects which impair the accuracy of the probe, but not so much concerning the determination of the plasma potential.

## The Plasma Apparatus

DP-machines are well-established tools for basic plasma investigations.[10] The Innsbruck DP-machine consists of a vacuum cylinder of 44 cm diameter and 90 cm length. The chamber is separated into a source chamber and a target chamber by a fine-mesh grid. The grid is isolated from the walls and usually biased to about –100 V. In each part of the DP-machine a heated double filament of 0.2 mm diameter tungsten wire serves as hot cathode for a low-temperature discharge in argon. The inner side of the entire chamber is covered by rows of strong permanent magnets with opposite polarity to increase the efficiency of the discharge.

With a background pressure between $10^{-4}$ and $10^{-3}$ mbar and a discharge current between 50 and 300 mA, the achievable plasma density lies in the range of $10^9$ and $10^{10}$ $cm^{-3}$. In the present experiments, plasma was produced only in the target chamber.

# EXPERIMENTAL RESULTS AND DISCUSSION

Fig. 2 a,b shows typical sets of current voltage characteristics of an emissive probe taken in the Innsbruck DP-machine Ar-plasma for a background pressure of $10^{-3}$ mbar and a discharge current of 200 mA which corresponds to a density of about $3\times10^9$ $cm^{-3}$.

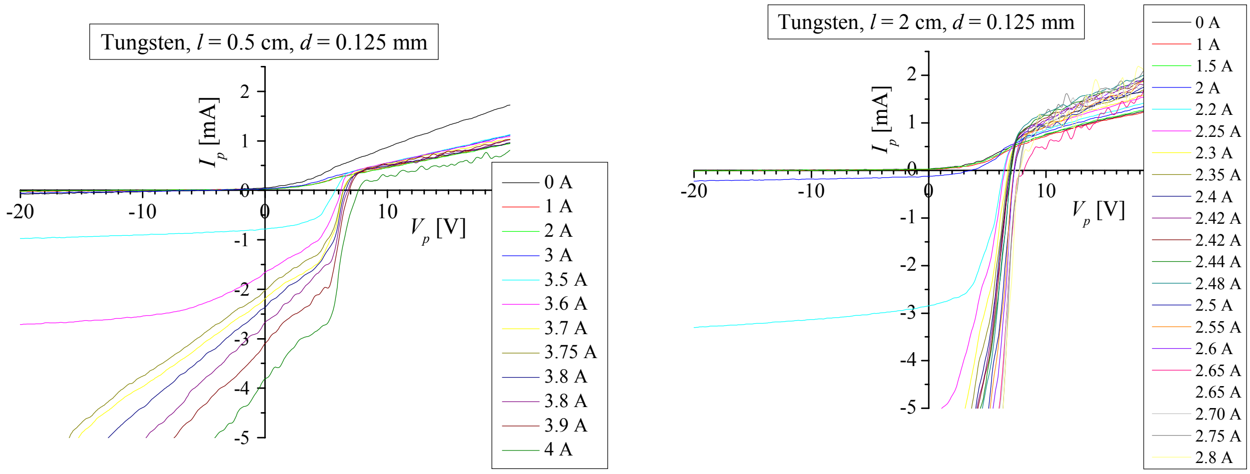

**(a)** **(b)**

**FIGURE 2.**. Current-voltage characteristics of two emissive probes of 0.125 mm diameter tungsten with different wire lengths, (a) 5 mm total loop length, (b) 20 mm total loop length, for increasing wire heating current.

This figure shows various effects that are typical for cold and emissive probes. For no heating such a probe acts as cold probe, however, with the geometry rather of a cylindrical probe.

The characteristic for 0 A heating current in Fig. 2 a with a loop length of only 5 mm could be due to coating since its electron saturation part is considerably higher than of the following characteristics. However, this probe was then used for the first time. From the following curves we see that expectedly the magnitude of the emission current on the left-hand side increases while the floating potential shifts to the right-hand side. In this case, extremely high heating currents were applied which for the highest value (4 A) led to a fast reduction of the wire diameter and thereby of the geometrical collection surface of the probe until the probe melted. For very high heating currents we also see a clear increase of the fluctuations superimposed on the entire characteristic. But in the range from 1 A to 3.9 A there is only a small variation of the electron saturation current.

Fig. 2 b with a loop length 4 times as long obviously also produces a much larger emission current. On the other side the electron saturation current shows a much stronger effect with the heating current; we see a strong increase, which behavior is closer to the expected one described in the Introduction.

In general our results also show that it is advantageous to fire a probe for a while until bright red hot before using them for measurements. This not only cleans the surface but apparently affects also deeper layers beneath it so that the work function has a better constancy after this treatment.

Also Fig. 3 shows the principle behavior of emissive probes when the floating potential is measured. We clearly see that for a certain heating current the floating potential suddenly increases, approaching the value of the plasma potential that here was determined according to the textbook from the inflection point of the cold probe characteristic. For both loop lengths the behavior is qualitatively the same. However, very surprising is the result that in both cases the floating potential can also exceed the cold probe value! This phenomenon was definitely not seen in denser and hotter plasmas, as for instance on that of the CASTOR tokamak.[2] But also in the case of the recently investigated laser-heated probe in the plasma of VINETA, also for strong heating the floating potential remains clearly below the value of the cold probe.[11] On the other hand, the transgression of the floating potential of an emissive probe over the value of the cold probe was seen sometimes also in other thin cold plasmas such as in a Q-machine.[12]

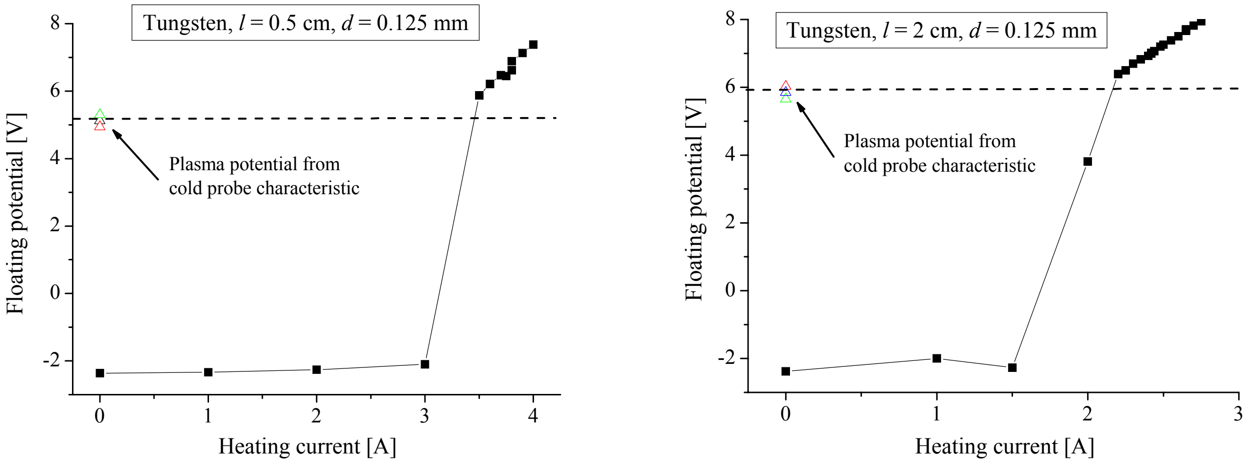

**(a)** **(b)**

**FIGURE 3.** Floating potential of the emissive probes of Fig. 2 versus heating current, (a) for the loop length of 5 mm, (b) for the loop length of 20 mm.

Obviously further intensive investigations are needed to fully explain the above described phenomena, in particular the question whether or not, and if yes, to what extent a space charge forms around an emissive probe even in the floating case.

## ACKNOWLEDGMENTS

The work was supported by the Austrian Science Foundation (Fonds zur Förderung der wissenschaftlichen Forschung) under grant No. L302-N02, Austrian-Czech Scientific-Technical Collaboration project A-14/2004, the Czech Science Foundation, grants 202/03/H162, 202/06/0776 and 202/04/0360, by the Ministry of Education, Youth and Sports, Research plan MSM 0021620834, by the and by EURATOM.

## REFERENCES

1. A. Marek, R.P. Apetrei, S.B. Olenici, R. Gstrein, I. Picková, P. Kudrna, M. Tichý, R. Schrittwieser, *13th Int. Cong. Plasma Phys.*, Kiev, May 22-26, 2006, submitted.
2. R. Schrittwieser, J. Adámek, P. Balan, M. Hron, C. Ioniţă, K. Jakubka, L. Kryška, E. Martines, J. Stöckel, M. Tichý, G. Van Oost, *Plasma Phys. Contr. Fusion* **44**, 567-578 (2002).
3. M.Y. Ye, S. Takamura, *Phys. Plasmas* **7**, 3457-3463 (2000).
4. N. Mahdizadeh, F. Greiner, M. Ramisch, U. Stroth, W. Guttenfelder, C. Lechte, K. Rahbarnia, *Plasma Phys. Contr. Fusion* **47**, 569-579 (2005).
5. A. Siebenförcher, R. Schrittwieser, *Rev. Sci. Instrum.* **67**, 849 - 850 (1996).
6. R. Schrittwieser, C. Ioniţă, P.C. Balan, Jose A. Cabral, H.F.C. Figueiredo, V. Pohoaţă, C. Varandas, *Contrib. Plasma Phys.* **41**, 494 - 503 (2001).
7. J. Adámek et al., *Czechoslovak J. Phys.* **52**, 1115-1120 (2002).
8. P. Balan et al., *Rev. Sci. Instrum.* **74**, 1583-1587 (2003).
9. C. Ioniţă et al., *Rev. Sci. Instrum.* **75**, 4331-4333 (2004).
10. R.J. Taylor, K.R. MacKenzie, H. Ikezi, *Rev. Sci. Instrum.* **43,** 1675-1678 (1972).

11 R. Schrittwieser, C. Ioniţă, P.C. Balan, C.A.F. Varandas, C. Silva, J. Stöckel, M. Tichý, E. Martines, G. Van Oost, T. Klinger, R. Madani, R.M.O. Galvão, the ISTTOK team, the CASTOR team, *Proc. 2nd German-Polish Conf. Diagnostics of Plasmas* (Krakow, Poland, 2004), Inv12.

12 D. Strele, private communication.

# References

Alaghband, G. (1997). Parallel Computing and Architectures. http://carbon.cudenver.edu/~galaghba/csc6551.html, lecture notes of Math 4674/CSC 6551 held on University of Colorado. 66

Auciello, O. & Flamm, D.L. (1989). *Discharge Parameters and Chemistry*, vol. 1 of *Plasma Diagnostics*. Academic Press, San diego, London. 7, 8, 15, 15

Balan, P., Schrittwieser, R., Ioniță, C., Cabral, J.A., Figueiredo, H.F.C., Fernandes, H., Varandas, C., Adámek, J., Hron, M., Stöckel, J., Martines, E., Tichý, M. & Oost, G.V. (2003). Emissive Probe Measurements of Plasma Potential Fluctuations in the Edge Plasma Regions of Tokamaks. *Rev. Sci. Instrum.*, **74**, 1583–1587. 8, 12, 14

Bilyk, O. (2005). *Probe Diagnostics of Low-temperature Plasma*. Ph.D. thesis, Charles University in Prague, Faculty of Mathematics and Physics, Department of Electronics and Vacuum Physics, Czech Republic. 77, 97, 98

Bilyk, O., Holík, M., Marek, A., Kudrna, P., Tichý, M. & Behnke, J.F. (2004a). Fluctuations of the magnetically-supported dc discharge in coaxial configuration. *Vacuum*, **76**, 437–445. 116

Bilyk, O., Kudrna, P., Holík, M., Marek, A., Tichý, M. & Behnke, J.F. (2004b). A study of discharge fluctuations in magnetically-supported dc discharge in cylindrical and inverted cylindrical configuration. *Czech Jour. Phys.*, **54**, C735–C741. 116

Bilyk, O., Holík, M., Kudrna, P., Marek, A. & Tichý, M. (2006). Observation of wave-like structures in magnetized dc discharge in cylindrical symmetry in argon. *Contrib. Plasma Phys.*, **46**, 361–366. 116

Birdsall, C.K. & Langdon, A.B. (1991). *Plasma Physics via Computer Simulation*. Adam Hilger, Bristol, Philadelphia and New York. 62, 63, 64, 90

Bradley, J.W., Karkari, S.K. & Vetushka, A. (2004). A Study of the Transient Plasma Potential in a Pulsed Bi-Polar dc Magnetron Discharge. *Plasma Sources Sci. Technol.*, **13**, 189–4137. 8

Cho, M.H., Chan, C., Hershkowitz, N. & Intrator, T. (1984). Measurement of Vacuum Space Potential by an Emissive Probe. *Rev. Sci. Instrum.*, **55**, 631–632. 16

Dimitriu, D.G., Găman, C., Mihai-Plugaru, M., Amarandei, G., Ionită, C., Lozneanu, E., Sanduloviciu, M. & Schrittwieser, R. (2004). Simple Experimental Methods to Control Chaos in a Double Plasma Machine. *Acta Phys. Slovaca*, **54**, 89–96. 21

Gewartowski, J.W. & Watson, H.A. (1965). *Principles of Electron Tubes*. D. Van Nostrand Company, Inc., Princeton, New Jersey. 9, 10

Gstrein, R., Marek, A., Ionita, C., Kudrna, P., Olenici, S.B., Balan, P.C., Schrittwieser, R. & Tichý, M. (2006). Space Charge Effects of Emissive Probes, Investigated in a DP-Machine. *Proceedings contributed papers CD of ICPP'06 in Kiev, Paper A181*, 1–4. 14, 44, 115

Gyergyek, T. & Čerček, M. (2005). Fluid Model of a Sheath Formed in Front of an Electron Emitting Electrode Immersed in a Plasma with Two Electron Temperatures. *Contrib. Plasma Phys.*, **45**, 89–110. 12, 14

Hammel, J. & Verboncoeur, J. (2004). DC Discharge Studies Using PIC-MCC. Tech. rep., Plasma Theory and Simulation Group, Department of Electrical Engineering, University of California, Berkeley, available at http://langmuir.nuc.berkeley.edu/∼jhammel/report.pdf. 64, 109

Hewett, D., Larson, W. & Doss, S. (1992). Solution of Simultaneous Partial Differential Equations Using Dynamic ADI: Solution of the Streamline Darwin Field Equations. *Journal of Computational Physics*, **101**, 11–24. 63

Hippler, R., Pfau, S., Schmidt, M. & Schoenbach, K.H. (2001). *Low Temperature Plasma Physics: Fundamental Aspects and Applications*, chap. Langmuir Probe Diagnostics of Low-Temperature Plasmas. Wiley-VCH, Berlin. 7

Hobbs, G.D. & Wesson, J.A. (1967). Heat Flow Through a Langmuir Sheath in Presence of Electron Emission. *Plasma Phys.*, **9**, 85–87. 13, 41

Holík, M., Kudrna, P., Bilyk, O., Rusz, J., Tichý, M., Behnke, J.F., Porokhova, I.A. & Golubovskii, Y.B. (2002). 2-D Experimental Study of Plasma Parameters in the Cylindrical Magnetron dc Discharge. *Czech. Jour. Phys., Suppl. D*, **52**, D673–D680. 19, 21

Holík, M., Bilyk, O., Marek, A., Kudrna, P., Behnke, J.F. & Tichý, M. (2004). 2-D Experimental Study of the Plasma Parameter Variations of the Magnetically Sustained DC Discharge in Cylindrical Symmetry in Argon. *Contrib. Plasma Phys., Suppl. D*, **44**, 613–618. 79, 99, 101, 116

Ishiguro, S. & Sato, N. (1993). Plasma Structures in Front of a Floated Emissive Electrode. *Phys. Fluids B*, **5**, 4237–4243. 14

Kawamura, E., Birdsall, C.K. & Vahedi, V. (2000). Physical and Numerical Methods of Speeding up Particle Codes and Paralleling as Applied to RF Discharges. *Plasma Sources Sci. Technol.*, **9**, 413–428. 64, 66, 92

Kohl, W.H. (1995). *Handbook of Materials and Techniques for Vacuum Devices*. American Vacuum Society classics, AIP Press, New York. 24

Kracík, J. & Tobiáš, J. (1966). *Fyzika plazmatu*. Academia, Prague. 60

Kudrna, P., Holík, M., Tichý, M., Csambal, C., Behnke, J.F., Porokhova, I.A. & Golubovskii, Y.B. (2002). PIC-MCC Modeling of the DC Discharge in Cylindrical Magnetron. *Czech. Jour. Phys., Suppl. D*, **52**, D666–D672. 79

LIEBERMAN, M.A. & LICHTENBERG, A.J. (1994). *Principles of Plasma Discharges and Materials Processing*. John Wiley and Sons, Inc., New York. 69

MADANI, R., IONITA, C., SCHRITTWIESER, R., AMARANDEI, G., BALAN, P. & KLINGER, T. (2004). A Laser-Heated Emissive Probe for Fusion Applications. *Proceedings of 31st EPS 2004 in London, ECA Vol.28G, P-5.127*, 1–4. 16, 17

MAHDIZADEH, N., GREINER, F., RAMISCH, M., STROTH, U., GUTTENFELDER, W., LECHTE, C. & RAHBARNIA, K. (2005). Comparison of Langmuir and Emissive Probes as Diagnostics for Turbulence Studies in the Low-Temperature Plasma of the Torsatron TJ-K. *Plasma Phys. Control. Fusion*, **47**, 569579. 16

MAREK, A., KUDRNA, P., HOLÍK, M., BILYK, O. & TICHÝ, M. (2004). The PIC Simulation of the Magnetized DC Discharge Plasma in the Cylindrical Configuration. *Proc. of Contrib. Papers of the WDS'04, Part II*, 316–321. 83, 85, 115

MAREK, A., KUDRNA, P., HOLÍK, M., BILYK, O., PICKOVÁ, I., TICHÝ, M. & APETREI, R.P. (2005a). 2D PIC Simulation of DC Magnetized Plasma in Cylindrical Magnetron. *Acta Phys. Slovaca*, **55**, 461–466. 90, 115

MAREK, A., KUDRNA, P., PICKOVÁ, I., HOLÍK, M., BILYK, O. & TICHÝ, M. (2005b). 2D PIC Simulation of the DC Discharge in Cylindrical Magnetron. *Proc. of Contrib. Papers of the WDS'05, Part II*, 362–367. 115

MAREK, A., KUDRNA, P., KOMM, M., PICKOVÁ, I. & TICHÝ, M. (2006a). Progress in PIC Simulation of the dc Argon Discharge in Cylindrical Magnetron. *Proc. of Contrib. Papers of the WDS'06, Part II*, 133–138. 115

MAREK, A., PICKOVÁ, I., KUDRNA, P., TICHÝ, M., APETREI, R.P., OLENICI, S.B., GSTREIN, R., SCHRITTWIESER, R. & IONITA, I. (2006b). Experimental Investigation of the Change of the Electron Saturation Current of a dc-heated Emissive Probe. *Czech. Jour. Phys., Suppl B*, **56**, B932–B937. 115

Marek, A., Apetrei, R.P., Picková, I., Kudrna, P., Tichý, M., Schrittwieser, R. & Ionita, I. (2007). Can a strongly emitting probe be used in a low temperature plasma? *Book of abstracts SAPP XVI conference (ed. J. Matúška, Š. Matejčík and J.D. Skalný), ISBN: 978-80-89186-13-6*, 225–226. 115

Mravlag, E. & Krumm, P. (1990). Space Potential Measurements With a Continuously Emitting Probe. *Rev. Sci. Instrum.*, **61**, 2164–2170. 16

Okuno, Y. & Fujita, H. (1991). Potential Formation Near Powered Electrode in Radio-Frequency-Driven Discharge. *J. Appl. Phys.*, **70**, 642–644. 8, 16

Passoth, E., Kudrna, P., Csambal, C., Behnke, J.F., Tichý, M. & Helbig, V. (1997). An Experimental Study of the Plasma Density Determination by a Cylindrical Langmuir Probe at Different Pressures and Magnetic Fields in a Cylindrical Magnetron Discharge in Heavy Rare Gases. *J. Phys. D: Appl. Phys.*, **30**, 1763–1777. 75

Phelps, A.V. & Petrović, Z.L. (1999). Cold-Cathode Discharges and Breakdown in Argon: Surface and Gas Phase Production of Secondary Electrons. *Plasma Sources Sci. Technol.*, **8**, R21–R44. 109

Picková, I., Marek, A., Tichý, M., Kudrna, P. & Apetrei, R.P. (2006). Measurements With the Emissive Probe in the Cylindrical Magnetron. *Czech. Jour. Phys., Suppl B*, **56**, B1002–B1008. 115

Popov, T. (2006). private communications. 24

Raizer, Y.P. (1991). *Gas Discharge Physics*, vol. 1. Electric Discharges Through Gases. Springer-Verlag, Berlin, Heidelberg and New York. 68, 73

Rapp, D. & Englander-Golden, P. (1965). Total Cross Sections for Ionization and Attachement in Gases by Electron Impact. I. Positive Ionization. *J. Chem. Phys.*, **43**, 1464–1479. 80

Roberto, M., Smith, H.B. & Verboncoeur, J.P. (2003). Influence of Metastable Atoms in Radio-Frequency Argon Discharges. *IEEE Transactions on Plasma Science*, **31**, 1292–1298. 110, 110

RUSZ, J. (2003). *Studium nízkoteplotního plazmatu v magnetickém poli*. Ph.D. thesis, Charles University in Prague, Faculty of Mathematics and Physics, Department of Electronics and Vacuum Physics, Czech Republic. 79, 97, 99, 104

SCHRITTWIESER, R., IONITA, C., BALAN, P.C., CABRAL, J.A., FIGUEIREDO, F.H., POHOATA, V. & VARANDAS, C. (2001). Application of Emissive Probes for Plasma Potential Measurements in Fusion Devices. *Contrib. Plasma Phys.*, **41**, 494–503. 8, 8

SIEBENFÖRCHER, A. & SCHRITTWIESER, R. (1996). A New Simple Emissive Probe. *Rev. Sci. Instrum.*, **67**, 849–850. 23

SMITH, J.R., HERSHKOWITZ, N. & COAKLEY, P. (1979). Inflection-point Method of Interpreting Emissive Probe Characteristics. *Rev. Sci. Instrum.*, **50**, 210–218. 15

STENZEL, R.L. (1997). http://www.physics.ucla.edu/plasma-exp/180E-W97/EmissiveProbe.html, part of lectures of physics (Physics 180E) of University of California. 11

SURENDRA, M., GRAVES, D.B. & JELLUM, G.M. (1990). Self-Consistent Model of a Direct-Current Glow Discharge: Treatment of Fast Electrons. *Phys. Review A*, **41**, 1112–1125. 80

TAKAMURA, S., OHNO, N., YE, M.Y. & KUWABARA, T. (2004). Space-Charge Limited Current from Plasma-Facing Material Surface. *Contrib. Plasma Phys.*, **44**, 126–137. 14, 14, 52, 52, 117, 118, 120, 120, 121, 122, 123

TRUNEC, D., HOLÍK, M., KUDRNA, P., BILYK, O., MAREK, A., HIPPLER, R. & TICHÝ, M. (2004). Monte carlo simulations of the electron currents collected by electrostatic probes. *Contrib. Plasma Phys.*, **44**, 577–581. 116

VAHEDI, V. & SURENDRA, M. (1995). A Monte Carlo Collision Model for the Particle-in-cell Method: Applications to Argon and Oxygen Discharges. *Comp. Phys. Comm.*, **87**, 179–198. 63, 80

Vahedi, V., DiPeso, G., Birdsall, C.K., Lieberman, M.A. & Rognlien, T.D. (1993). Capacitive RF Discharges Modelled by Paricle-In-Cell Monte Carlo Simulation. I: Analysis of Numerical Techniques. *Plasma Sources Sci. Technol.*, **2**, 261–272. 111

van der Straaten, T.A., Cramer, N.F., Falconer, I.S. & James, B.W. (1998). The Cylindrical DC Magnetron Discharge: I. Particle-In-Cell Simulation. *J. Phys. D: Appl. Phys.*, **31**, 177190. 66

Verboncoeur, J.P. (2005). Paricle Simulation of Plasmas: Review and Advances. *Plasma Phys. Control. Fusion*, **47**, A231–A260. 61, 62, 64

Verboncoeur, J.P., Alves, M.V., Vahedi, V. & Birdsall, C.K. (1993). Simultaneous Potential and Circuit Solution for 1d Bounded Plasma Particle Simulation Codes. *J. Comp. Physics*, **104**, 321–328. 79

Verboncoeur, J.P., Langdon, A.B. & Gladd, N.T. (1995). An Object-Oriented Electromagnetic PIC Code. *Comp. Phys. Comm.*, **87**, 199–211. 2, 79

Wang, J., Liewer, P. & Decyk, V. (1995). 3d Electromagnetic Plasma Particle Simulations on a Parallel Computer. *Computer Physics Communications*, **87**, 35–53. 67

Wilson, E.H., Jeong, J. & Hershkowitz, N. (2002). An Emissive Probe With a Rhenium Filament for Measuring Plasma Potential in a Radio Frequency Oxygen Plasma. *Rev. Sci. Instrum.*, **73**, 2033–4137. 8, 16, 104

Yan, S., Kamal, H., Amundson, J. & Hershkowitz, N. (1996). Use of Emissive Probes in High Pressure Plasma. *Rev. Sci. Instrum.*, **67**, 4130–4137. 8, 49